An Investigation into the Coordination Chemistry of Boratriazine-based Terpy-type Ligands

Jamie Savard

Thesis submitted to the
Faculty of Graduate and Postdoctoral Studies
In partial fulfillment of the requirements for the degree of

Master of Science
in
Chemistry

Ottawa-Carleton Chemistry Institute
University of Ottawa

Candidate	**Supervisor**
Jamie Savard	Jaclyn Brusso

Abstract

The rational design of ligand architectures that enables the development of well-defined metallic constructs has long been recognized as an avenue toward controlling and/or tuning the properties of the corresponding material. To date, one of the most widely studied ligand systems is 2,2’;6’,2”-terpyridine, whose tridentate chelating environment allows for coordination to a variety of metal ions with a wide range of geometries. The development of a terpy-like framework which incorporates a boratriazine moiety into the central ring has been recently reported by the Brusso group, namely 2,2-difluoro-4,6-bis(2-pyridyl)-1,3-dihydro-1,3,5,2-triazaborinine (Py_2F_2BTA) and 2,2-difluoro-4,6-bis(2-4,6-pyrimidinyl)-1,3-dihydro-1,3,5,2-triazaborinine (Pm_2F_2BTA). These compounds constitute unfused analogues to the extensively studied boron dipyrromethene (bodipy) family of luminophores, which are known for their high thermal resistance, chemical robustness, low photodegradation, and interesting photophysical signatures. While numerous bodipy derivatives have been studied, metal coordination with these compounds remains an intricate property to explore. Thus, the work presented herein represents the first investigations into the coordination chemistry of these novel ligand frameworks.

Chapter one serves as an introduction to coordination chemistry, exploring important concepts as they relate to the field; the origin of our boratriazine based ligands is also explored within this chapter. Chapter two aims to describe trends in coordination and reactivity of these ligands with iron and cobalt metal sources of different oxidation states. The third and fourth chapter focuses on the targeted use of azide and thiocyanate ligands, respectively, to promote interesting magnetic interactions in related complexes. In the fifth chapter, luminescent metal complexes synthesized through the use of d^{10} metals are described. Conclusions and future outlooks are then presented in the final section, chapter six.

Statement of Contribution

Acknowledgements are owed to Dr. Muralee Murugesu and Gabriel Brunet for the interpretation and measurement of the magnetic data presented herein. Additional thanks are given to Dr. Bulat Gabidullin, Dr. Anandi Srinivasan and Raúl Castañeda for having collected and solved the crystal structure data within this manuscript. Lastly, recognition is given to Dr. Riccardo Marin for having measured the solid-state emission of select complexes.

Table of Contents

CHAPTER 1

CHAPTER 2

CHAPTER 3

CHAPTER 4

CHAPTER 5

CHAPTER 6

List of Figures

List of Tables

List of Schemes

List of Abbreviations

VBT	Valence bond theory
CFT	Crystal field theory
HS	High spin
LS	Low spin
LFT	Ligand field theory
Terpy	2,2’;6’,2”-terpyridine
Bodipy	Difluoro-4-bora-3a,4a-diaza-*s*-indacene
Py$_2$F$_2$BTA	2,2-difluoro-4,6-bis(2-pyridyl)-1,3-dihydro-1,3,5,2-triazaborinine
Pm$_2$F$_2$BTA	2,2-difluoro-4,6-bis(2-pyrimidinyl)-1,3-dihydro-1,3,5,2-triazaborinine
BTA	Boratriazine
Py$_2$ImAm	*N*-2-pyridylimidoyl-2-pyridylamidine
Pm$_2$ImAm	*N*-2-pyrimidylimidoyl-2-pyrimidylamidine
SCXRD	Single crystal X-ray diffraction
DMF	Dimethylformamide
DMA	Dimethylacetamide
DFT	Density functional theory
LUMO	Lowest unoccupied molecular orbital
HOMO	Highest occupied molecular orbital
SOMO	Singly occupied molecular orbital
EE	End-to-end
EO	End-on
AF	Antiferromagnetic
FM	Ferromagnetic
SMM	Single molecule magnet
LC	Ligand centered
LLCT	Ligand to ligand charge transfer
LMCT	Ligand to metal charge transfer
CIE	Commission Internationale de l' Éclairage

List of Compounds Reported

2.1a	$[Fe^{III}Cl_3(Py_2F_2BTA)]\cdot MeCN$
2.1b	$[Fe^{III}Cl_3(Py_2F_2BTA)]\cdot 2DMF$
2.1c	$[Fe^{III}Cl_3(Py_2F_2BTA)]\cdot 2DMA$
2.2	$[Fe^{III}Cl_2(Py_2F_2BTA)(MeOH)]Cl$
2.3	$[Fe^{III}Cl_2(Py_2F_2BTA)(EtOH)]Cl$
2.4	$[Fe^{III}Cl_3(Py_2MeO_2BTA)]$
2.5	$[Fe^{III}Br_3(Py_2MeO_2BTA)]$
2.6	$[Fe^{III}Cl_3(Pm_2F_2BTA)]$
2.7	$[Fe^{III}Br_3(Pm_2F_2BTA)]$
2.8	$[\{Fe^{III}(NO_3)(Py_2F_2BTA)(H_2O)\}_2(\mu–O)](NO_3)_2\cdot 4DMA$
2.9	$[\{Fe^{III}(NO_3)(Py_2F_2BTA)(MeOH)\}_2(\mu–O)](NO_3)_2$
2.10	$[\{Fe^{III}(NO_3)(Pm_2F_2BTA)(H_2O)\}_2(\mu–O)](NO_3)_2$
2.11	$[\{Fe^{III}(NO_3)(terpy)(H_2O)\}_2(\mu–O)](NO_3)_2$
2.12	$[\{Fe^{III}(NO_3)(terpy)(MeOH)\}_2(\mu–O)](NO_3)_2$
2.13	$[\{Fe^{III}(NCS)_4(Py_2F_2BTA)\}_2(\mu–O)]$
2.14	$[Fe^{II}Cl_2(Py_2F_2BTA)]$
2.15	$[Co^{II}Cl_2(Py_2F_2BTA)]$
2.16	$[Fe^{II}Br_2(Py_2F_2BTA)(MeOH)]$
2.17	$[Fe^{II}Br_2(Pm_2F_2BTA)]\cdot MeOH$
2.18	$[Co^{II}(Py_2F_2BTA)_2][Co^{II}(NCS)_4]\cdot 4DMF$
2.19	$[Co^{III}(Py_2F_2BTA)_2(CH_3CO_2)]\cdot 2MeCN$
3.1	$[Fe_2{}^{II}(\mu_{1,1}-N_3)_2(N_3)_2(Py_2F_2BTA)_2]$
3.2	$[Co_2{}^{II}(\mu_{1,1}-N_3)_2(N_3)_2(Py_2F_2BTA)_2]$
4.1	$[Fe^{II}(NCS)_2(Py_2F_2BTA)]\cdot MeCN$
4.2	$[Co^{II}(NCS)_2(Py_2F_2BTA)]\cdot MeCN$
5.1	$[Zn^{II}Cl_2(Py_2F_2BTA)]$
5.2	$[Zn^{II}Cl_2(Pm_2F_2BTA)]$ MeOH
5.3	$[Cd^{II}Cl_2(Py_2F_2BTA)(MeOH)]$
5.4	$[Cd^{II}Cl_2(Pm_2F_2BTA)]\cdot MeOH$
5.5	$[Zn^{II}(NCS)_2(Py_2F_2BTA)]\cdot MeCN$
5.6	$[Cd^{II}(Py_2F_2BTA)_2]\cdot 2(ClO_4)$

CHAPTER 1

1.1 Coordination Chemistry: An Interplay Between Metals and Ligands

The study of coordination chemistry deals, by definition, with metal-ligand interactions. It is well known that the properties and reactivities of a coordinated ligand differ substantially from its unbound 'free' form. Concomitantly, combination of said ligand with metal ion(s) of differing oxidation states and identity will further diversify the observed behaviours in the resulting compound, enabling a wide range of exploitable phenomena. In this regard, a key objective in coordination chemistry is to predict and control the types of molecular attributes which arise from complexation for the development of useful constructs.

The ability to accurately describe bonding in coordination compounds is crucial in understanding the nature of their properties. Valence bond theory (VBT) was first developed by Linus Pauling in the early 1900s to describe covalent bonding and was then extended to incorporate compounds of transition metals.[1] VBT treats metal ions as Lewis acids, characterized by the availability of low lying empty orbitals suitable for accommodating electrons from another species, namely, ligands. In this model, ligands are viewed as Lewis bases, and are characterized by their ability to readily donate an electron pair. This pairing results in the formation of a coordinate bond. Upon coordination of a ligand set about a metal centre, atomic orbitals responsible for the formation of these coordinate bonds will mix, forming hybrid orbitals possessing directional properties. In VBT theory, this provides rationale for the various geometries that are observed in coordination complexes. Where VBT fails, however, is in demystifying the formation of outer and inner orbital complexes and resolving the source of distortion from ideal geometry commonly found in coordination complexes. In order to understand the physical characteristics of coordination complexes, more sophisticated bonding theories are required.[2]

Crystal field theory (CFT) is a theory that was developed in the 1930s by Bethe and Van Vleck which treats bonding in coordination compounds as comprised solely of electrostatic forces. That is, bonding is conceived to occur through positively charged metals with ligands that are either negatively charged, or possessing regions of high electron density.[3] Where this model shines is in describing the effects of coordination upon the bonding orbitals of the central metal ion. In transition metals, this invokes the five-degenerate *d*-orbitals d_{xy}, d_{yz}, d_{xz}, $d_{x^2}–d_{y^2}$, and d_{z^2} (Figure 1.1).

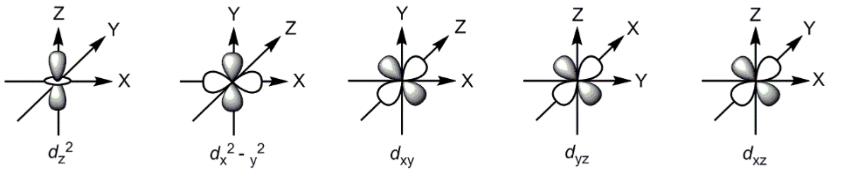

Figure 1.1 – Shape of five *d*-orbitals.

These orbitals can be grouped according to their molecular symmetry, which is dictated by the coordination geometry of the metal complex. For example, in octahedral complexes the d_{xy}, d_{yz}, and d_{xz} orbitals, which lie in between axes, have t_{2g} symmetry while the $\mathrm{d}_{x^2}–\mathrm{d}_{y^2}$ and d_{z^2} orbitals, lying along the axes, have e_g symmetry (Figure 1.2).

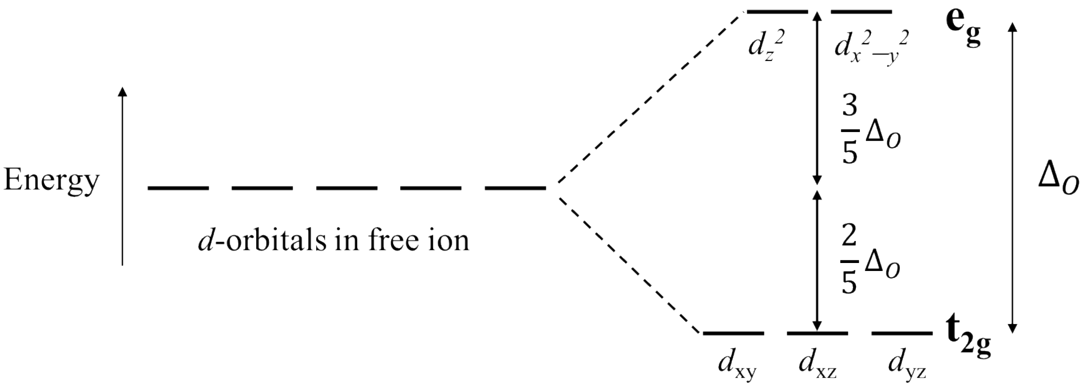

Figure 1.2 – Crystal field splitting of *d*-orbitals in an octahedral ligand field, Δ_{Oct}.

The bonding orbitals within a metal therefore have defined spatial occupancies which are dependent upon the nature of the metal ion as well as its oxidation state. When a set of ligands coordinates to a metal ion, it can do so with different geometric arrangements and coordination numbers. The symmetry labels for the *d*-orbitals depend upon the point group of the molecule (e.g., shape), as such, different splitting patterns are expected between coordination geometries (Figure 1.3). Additionally, the coordinated ligands often differ in terms of their stereoelectronic properties. As a result of complexation, the *d*-orbitals of the metal therefore experience inequivalent electronic interactions which manifest as a loss of degeneracy in their energies. The splitting of *d*-orbitals, called crystal field splitting, results in some of the orbitals occupying a lower and others a higher energy (visually represented as the orbitals below and above the barycentre in Figure 1.3). Each electron occupying an orbital of lowered energy contributes stabilization energy to the system. Conversely, electrons occupying orbitals of higher energy counter the stabilization of the system; the summative enthalpy upon complexation being termed the crystal field stabilization energy.[2]

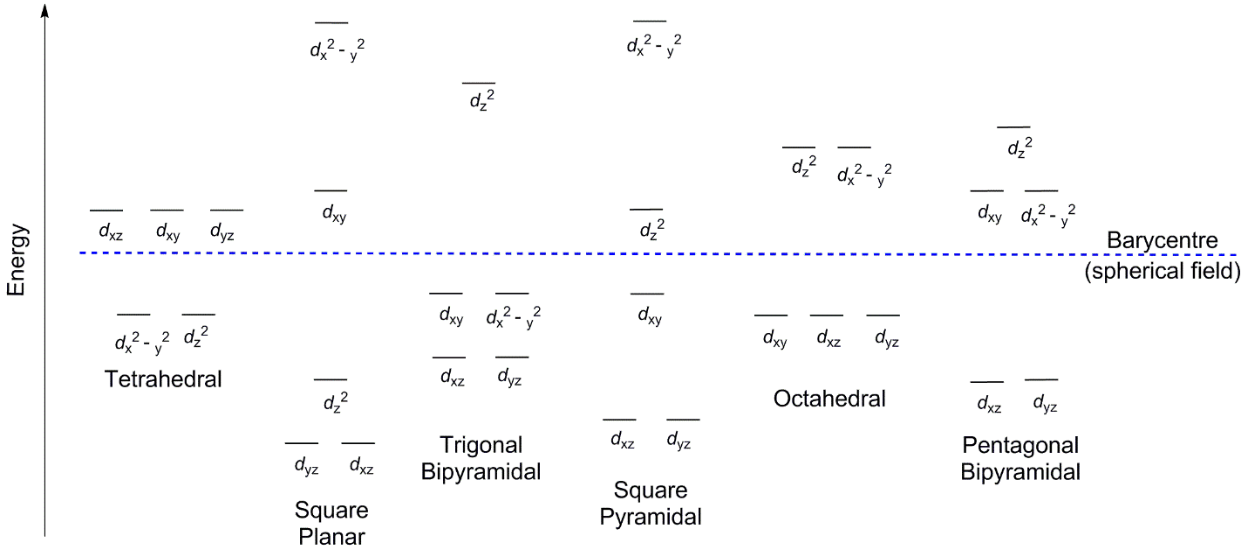

Figure 1.3 – Splitting patterns of *d*-orbital in different coordination environments.

The magnitude of crystal field splitting is largely governed by the nature of the associated ligands. Through the analysis of the spectra for numerous metal complexes, common ligands have been ordered in a sequence known as the spectrochemical series. A non-exhaustive version of this series is shown below and ordered for their increasing ability to split metal *d*-orbitals (Figure 1.4).[2] Ligands which cause a small degree of splitting (e.g., I^- and Br^-) are referred to as weak field ligands, while those which lead to larger splitting (e.g., CN^- and CO) are called strong field ligands.

$$\mathrm{I^- > Br^- > NCS^- > Cl^- > NO_3{}^- > N_3{}^- > F^- > HO^- >}$$

$$\mathrm{H_2O\ > SCN^- > py\ > NH_3\ > bpy > NO_2{}^- > CN^- > CO}$$

Figure 1.4 – Spectrochemical series.

As a result of crystal field splitting, complexes with the same metal ion and oxidation state may exist in either high, or low spin states (Figure 1.5).

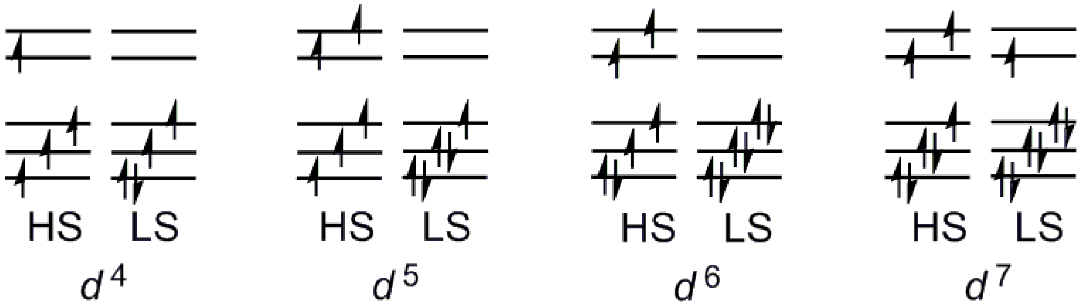

Figure 1.5 – High and low spin arrangement of electrons in an octahedral complex containing 4 to 7*d* electrons (HS: high spin and LS: low spin).

CFT successfully accounts for some magnetic properties, colors, hydration enthalpies, and structures of transition metal complexes, but it does not attempt to describe bonding.[2] Moreover, crystal field theory works well in systems involving highly electronegative ligands, but less so with systems that incorporate less polar ligands. In order to address this, ligand field theory (LFT) was developed by Orgel and Griffith in the 1950s as an improvement on CFT.[4] This model adds complexity to CFT by recognizing that both σ and π bonds can occur in metal–ligand interactions. This has helped rationalize non-intuitive observations from the spectrochemical series, such as why the hydroxide anion HO^- is a weaker field ligand than its neutral counterpart H_2O. LFT describes the whole toolkit required for understanding the bonding and properties of transition metal elements and their compounds.

It is important to note that, because not all metals are the same, bonding to a set of ligands will be more easily achieved by some over others. Small and highly charged species hold a higher surface charge density. This tendency towards ionic character can also be referred to as the ‘hardness’ of the entity. Conversely, large and diffusely charged species are better suited to interactions involving orbital overlap and can be termed as ‘soft’. For ligands, the trend from soft to hard coincides with the increasing electronegativity of the donor ion or group. On the other hand, metal ions that are less electronegative have more ‘hard’ character than more electronegative metals (Table 1.1). This allows for the application of a ‘like prefers like’ concept when considering metal–ligand interactions.

Table 1.1 – Classification of metals and ligands with different ‘hard’ and ‘soft’ character.

Hard	Intermediate	Soft
Ligands		
F^-, O^{2-}, HO^-, ROH, Cl^-, $N0_3^-$	Br^-, NO_2^-, N_3^-, SCN^-	CN^-, NCS^-, CO, I^-
Metals		
Fe^{3+}, Co^{3+}, Mn^{2+}, Mg^{2+}	Fe^{2+}, Co^{2+}, Ni^{2+}, Cu^{2+}, Zn^{2+}	Cu^+, Ag^+, Pd^{2+}, Pt^{2+}, Cd^{2+}

1.2 Harnessing Complexation: Engineering Useful Functionalities into Impactful Compounds

Coordination compounds have bolstered many new scientific advances across many different fields, such as, in molecular sensing, as potential therapeutic agents, in catalysis, gas adsorption, magnetic materials, and organic electronics (e.g., molecular devices for light driven energy conversion and storage) to name a few.[5–7] As such, the rational design and synthesis of metal complexes has been a long-standing goal in coordination chemistry.

Metals are known to exhibit preferential binding towards certain ligand architectures (e.g., monodentate *vs* multidentate, ionic *vs* neutral, or hard *vs* soft), partiality towards the adoption of certain coordination geometries, and favoritism towards holding certain oxidation states. These particularities allow for the use of clever approaches in the design of coordination compounds. Chelation, the binding of a ligand to a metal *via* two or more bonds, is an important strategic means towards influencing a desired mode of complexation. Numerous categories of chelates have been reported, however, pincer ligands are a class of special interest. The term 'pincer', coined in 1989 by van Koten, initially referred to tridentate ligands possessing of a central anionic carbon and two flanking binding units, enforcing a meridional (*mer*-) coordination mode about the metal centre.[8] Since then, the term pincer has grown more general, alluding to any three coordinate ligand which can occupy adjacent binding sites within a metal complex. Although largely due to conformational restrictions, pincer ligands have a strong preference for coordinating in *mer*-fashion. Facial coordination modes are also adopted if there is enough flexibility within the ligand system. Several key factors have led pincer systems to the cutting edge in ligand design: they permit otherwise labile ligands to be firmly bound, they can endow upon their complexes exceptional thermal stability, and the coordination spheres of these ligands are structured in well defined manners.[6]

To date, one of the most widely studied ligand systems is 2,2';6',2"-terpyridine (terpy), a prototypal tridentate ligand. The rich coordination chemistry of this compound (which varies from interaction with *s*-block metal cations, through to metal ions in the *p*-block, and on to the lanthanide and actinide series) has attracted much attention over recent decades (Figure 1.6). Through structural modifications, the properties of terpy-type ligand have shown remarkable tunability, which has led to many exciting innovations.[5–7]

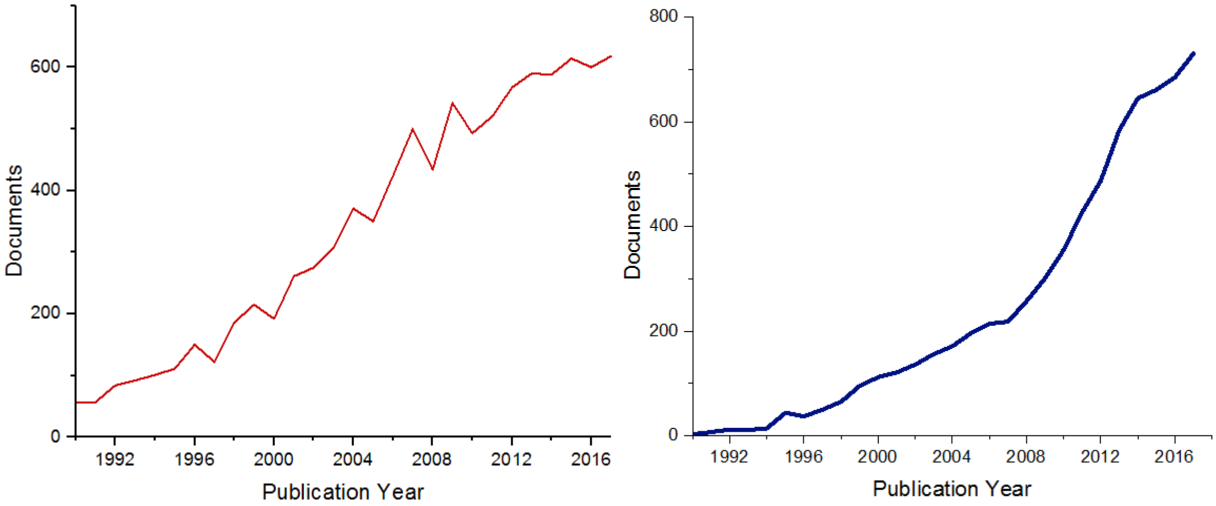

Figure 1.6 – Evolution of publications pertaining to “Terpyridine”, in red, and to “Bodipy”, in blue, since 1990 (Retrieved from Scifinder, June 2018).

1.3 Looking to Boron-dipyrromethene Based Fluorescent Dyes for Inspiration

The advent of 4,4-difluoro-4-bora-3a,4a-diaza-*s*-indacene (bodipy) dyes was first reported in 1968 by Treibs and Kreuzer,[9] gaining popularity in the nineties when the pioneering work of Boyer and coworkers garnered them a reputation as tunable dye lasers.[10–12] Bodipy-type materials have constituted a fascinating topic of research in modern photochemistry due to the tunability of the spectroscopic parameters of these chromophores (Figure 1.6). Notably, these compounds are characterized by strong absorption and sharp fluorescence spectral bands, which can span the entire range of visible light and into the NIR region, with molar absorptions approaching 10^5 $M^{-1}cm^{-1}$ and high quantum yields.[13–15] Compounds with the boron-dipyrromethene core have shown remarkable chemical robustness, thermal resistance, low photodegradation, and stability within the physiological pH range.[16] As such, this family of materials has been prolific in both scientific and technological fields. Device fabrication has been illustrated in a number of publications that test these dyes as fluorescence sensors, switches and probes,[17,18] in light harvesting arrays for antenna systems,[19,20] in photovoltaic devices,[21,22] in biomedicine (as fluorescence markers/bioimaging/singlet-oxygen photosensitizers),[15,23] and in chirality (fluorophores that respond to circular polarized light).[24] The rational design of these quasi-aromatic π systems enables for the construction of bodipy compounds with tailored properties. For example, the probability of intersystem crossing through heavy atom effect can promote singlet-oxygen generation,[23] photophysical processes (such as intramolecular charge transfer or photoinduced electronic transfer) that are sensitive to the presence of certain analytes can be induced,[25] molecular constructs with separated absorption and emission profiles *via* excited energy transfer can be customized,[22] oligomeric structures can support electrogenerated chemiluminescence,[26] and linking to nanoparticles/polymers can be incorporated for sensing purposes.[13]

1.4 Development of Terpy-like Boratriazine Ligands for Coordination Chemistry

In the pursuit of creating interesting and novel materials, we recently developed a terpy-type framework in which the N-BF_2-N motif from bodipy was incorporated into the central pyridyl ring of terpyridine affording 2,2-difluoro-4,6-bis(2-pyridyl)-1,3-dihydro-1,3,5,2-triazaborinine (Py_2F_2BTA) and 2,2-difluoro-4,6-bis(2-pyrimidinyl)-1,3-dihydro-1,3,5,2-triazaborinine (Pm_2F_2BTA) boratriazine (BTA) ligands (Scheme 1.1).[27]

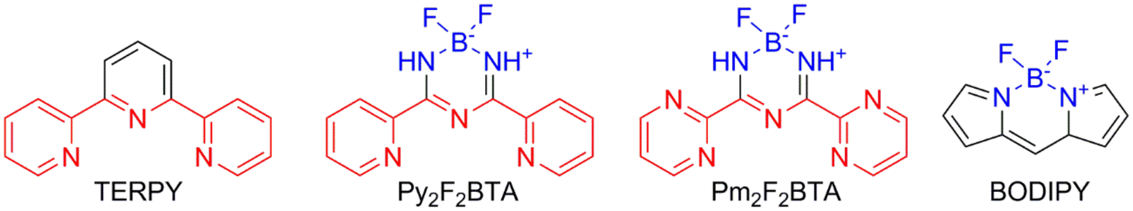

Scheme 1.1 – Chemical structures of tridentate ligands terpy, Py_2F_2BTA, Pm_2F_2BTA, along with bodipy. Red and blue portions in the BTA ligands highlight the terpy and BODIPY-like features, respectively

In doing so, we have effectively induced luminescence into the ligand system. Indeed, both the pyridyl and pyrimidyl derivative are emissive in the blue region upon UV irradiation. The photophysical properties of these compounds in a solution of DCM are summarized below (Table 1.2). In contrast, comparable bodipy and aza-bodipy analogues are typically found to absorb at higher wavelengths, with larger extinction coefficients and smaller stoke shifts. This is attributable to their rigid cores and larger degree of conjugation.[14] Through coordination to a metal ion, however, rigidity in BTA ligands has the potential to be induced such that the pyridyl and pyrimidyl side arms lose rotational freedom upon tridentate chelation.

Table 1.2 – Spectral properties of BTA ligands.[27]

	Py_2F_2BTA	Pm_2F_2BTA
$\lambda_{max}^{absorance}$, (nm)	310	307
ε^{d}, ($M^{-1}cm^{-1}$)	22795	14015
$\lambda_{max}^{emmision}$, (nm)	397	388
Quantum yield	0.12	0.07

Quantum Yields calculated at 22°C relative to 9, 10-diphenylanthracene in ethanol (QY = 0.90) using a Cary Eclipse Fluorescence Spectrophotometer (Agilent Technologies).

The synthetic procedures for the preparation of Py_2F_2BTA and Pm_2F_2BTA are quite similar (Scheme 1.2). Both compounds are prepared from their corresponding unsubstituted 1,3,5-triazapentadienes (i.e., *N*-imidoylamidine). *N*-imidoylamidine precursors remain a synthetic challenge to prepare, and as such have received little attention in the literature.[28–31] We have, however, demonstrated the high yielding synthesis of *N*-2-pyridylimidoyl-2-pyridylamidine (Py_2ImAm) from the reaction of 2-cyanopyridine with ammonia under pressure. The *N*-2-pyrimidylimidoyl-2-pyrimidylamidine (Pm_2ImAm) analogue can also be isolated from the reaction between 2-cyanopyrimidine and ammonia, albeit in more moderate yields and under milder reaction conditions. Treatment of Py_2ImAm and Pm_2ImAm with boron trifluoride diethyletherate in the presence of triethylamine then affords the desired boratriazine compounds.

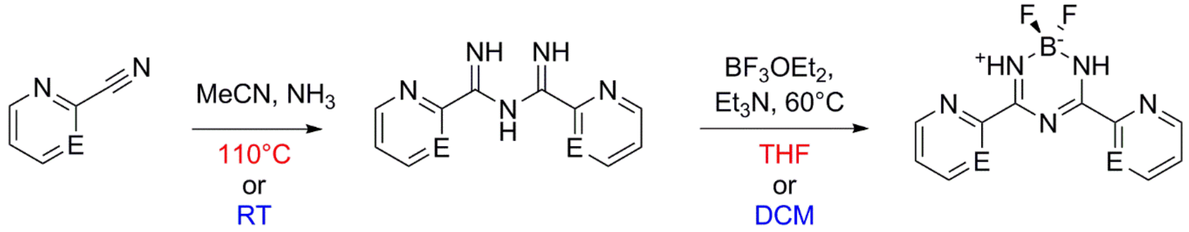

Scheme 1.2 – Synthesis of BTA ligands. Conditions for Py_2F_2BTA (E = CH) are shown in red; conditions for Pm_2F_2BTA (E = N) shown in blue.

These novel compounds represent unfused analogues of the extensively studied boron dipyrromethene. While extensive reports of bodipy derivatives have been studied, there are only few reports of unfused boratriazine compounds. Coordination of *N*-imidoylamidines to boron has been particularly underrepresented in the literature.[32–37] Moreover, taking advantage of their chelating ability enables us to further exploit the attributes of our BTA based compounds through metal coordination, which is not as easily achieved with bodipy based systems.

1.5. Outline of the Thesis

The goal of this work was to design and prepare novel coordination compounds of our boratriazine ligands using first row transition metals. Through the structural and physical analysis of an array of coordination complexes with this system, we have garnered an understanding of how these compounds behave in the presence of different metal ions. Through understanding the crystallization trends and chemical interactions between the ligands and different metal ions, the targeted synthesis of desirable metal complexes can be enabled.

Chapter two of this thesis provides the synthesis and structural characterization of a family of iron mononuclear and multinuclear compounds as well as a series of cobalt complexes. This section aims to describe trends in the reactivity of these metal salts with boratriazine-based ligands, as well as analyze their structural and physical properties. The third and fourth chapter focuses on the targeted use of azide and thiocyanate ligands, respectively, to promote interesting magnetic interactions in related complexes. In the fifth chapter, luminescent metal complexes synthesized through the use of d^{10} metals are described. Conclusions and future outlooks are then presented in the final section, chapter six.

1.6. References

1 L. Pauling, *Proc. Nat. Acad. Sci. USA*, 1975, **72**, 4200
2 V. Bhatt, *Essentials of Coordination Chemistry*, 2016, Academic Press, London Wall, London
3 G. Burns, *Introduction to Group Theory with Application*, 1977, Acamedic Press, Yorktown Heights, New York
4 D. P. Graddon, *An Introduction to Co-ordination Chemistry 2nd Edition*, 1968, Pergamon, London
5 E. A. Medlycott and G. S. Hanan, *Chem. Soc. Rev.*, 2005, **34**, 133
6 E. C. Constable, *Chem. Soc. Rev.*, 2007, **36**, 246
7 R. Shunmugam, G. J. Gabriel, K. A. Aamer and G. N. Tew, *Macromol. Rapid. Commun.*, 2010, **31**, 784
8 G. van Koten, *Pure & Appl. Chem.*, 1989, **61**, 10, 1681
9 A. Triebs and F. H. Kreuzer, *Liebigs Ann. Chem.*, 1968, **718**, 208
10 S. C. Guggenheimer, J. H. Boyer, K. Thangaraj, M. Shah, M-L. Soong and T. G. Pavlopoulos, *Applied Optics*, 1993, **32**, 21, 3942
11 J. H. Boyer, A. M. Haag, G. Sathyamoorthi, M-L. Soong, K. Thangaraj and T. G. Pavlopoulos, *Heteroat. Chem.*, 1993, **4**, 1, 39
12 M. Shah, K. Thangaraj, M-L. Soong, L. T. Wolford, J. H. Boyer, I. R. Politzer and T. G. Pavlopoulos, *Heteroat. Chem.*, 1990, **1**, 5, 389
13 J. Bañuelos, *Chem. Rec.*, 2016, **16**, 335
14 A. Loudet and K. Burgess, *Chem. Rev.*, 2007, **107**, 4891
15 T. Kowada, H. Maeda and K. Kikuchi, *Chem. Soc. Rev*., 2015, **44**, 4953
16 E. Banakova, A. Bobrov, A. Kazak, Y. Marfin, D. Merkushev, E. Molchanov, E. Rumyantsev, M. Shipalova, S. Usoltsev and O. Vodyanova, *J. Phys.: Conf Ser.*, 2018, **951**, 012017
17 N. Boens, V. Leen and W. Dehaen, *Chem. Soc. Rev.*, 2012, **41**, 1130
18 X. Qian, Y. Xiao, Y. Xu, X. Guo, J. Qian and W. Zhu, *Chem. Commun.*, 2010, **46**, 6418
19 J. Fan, M. Hu, P. Zhan and X. Peng, *Chem. Soc. Rev*., 2013, **42**, 29
20 J. Iehl, J. F. Nierengarten, A. Harriman, T. Bura and R. Ziessel, *J. Am. Chem. Soc.*, 2012, **134**, 988
21 J. S. Lu, H. Fu, Y. Zhang, Z. J. Jakubek, Y. Tao and S. Wang, *Angew. Chemie Int. Ed.*, 2011, **50**, 11658
22 A. Bessette and G. S. Hanan, *Chem. Soc. Rev.*, 2014, **43**, 3342
23 A. Kamkaew, S. H. Lim, H. B. Lee, L. V. Kiew, L. Y. Chung and K. Burgess, *Chem. Soc. Rev*., 2013, **42**, 77
24 E. M. Sánchez-Carnerero, A. R. Agarrabeitia, F. Moreno, B. L. Maroto, G. Muller, M. J. Ortiz and S. De La Moya, *Chem. Eur. J.*, 2015, **21**, 13488
25 R. Hu, E. Lager, A. Aguilar-Aguilar, J. Liu, J. W. Y. Lam, H. H. Y. Sung, I. D. Williams, Y. Zhong, K. S. Wong, E. Peña-Cabrera and B. Z. Tang, *J. Phys. Chem. C*, 2009, **113**, 15845.
26 J. Ouyang, T. C. Zietlow, M. D. Hopkins, F. R. F. Fan, H. B. Gray and A. J. Bard, *J. Phys.*

Chem., 1986, **90**, 3841

27 M. Yousaf, N. J. Yutronkie, R. Castañeda, J. A. Klein and J. Brusso, *New J. Chem.*, 2017, **41**, 12218

28 D. A. Peak, *J. Chem. Soc.*, 1952, **0**, 215

29 R. T. Boeré, T. L. Roemmele and X. Yu, *Inorg. Chem.*, 2011, **50**, 5123

30 H. C. Brown and P. D. Schuman, *J. Org. Chem.*, 1963, **28**, 1122

31 A. W. Cordes, C. D. Bryan, S. R. Scott, W. M. Davis, R. H. de Laat, J. D. Goddard, R. G. Hicks, D. K. Kennepohl, R. T. Oakley, N. P. C. Westwood, S. H. Glarum and R. C. Haddon, *J. Am. Chem. Soc.*, 1993, **115**, 7232

32 J. E. Milks, J. H. Polevy and G. W. Kennerly, *J. Am. Chem. Soc.*, 1962, **84**, 2529

33 V. A. Dorokhov, G. A. Stashina, V. M. Zhulin and B. M. Mikhailov, *Dokl. Akad. Nauk SSSR*, 1981, **258**, 351

34 B. M. Mikhailov, V. A. Dorokhov and V. I. Seredenko, *Bull. Acad. Sci. USSR, Div. Chem. Sci.*, 1978, **27**, 1205

35 C. Glotzbach, N. Goedeke, R. Froehlich, C.-G. Daniliuc, S. Saito, S. Yamaguchi and E.-U. Wuerthwein, *Dalton Trans.*, 2015, **44**, 9659

36 I. Haeger, R. Froehlich and E.-U. Wuerthwein, *Eur. J. Inorg. Chem.*, 2009, **2009**, 2415

37 S. A. Tikhonov, I. B. L'vov and V. I. Vovna, *Russ. J. Phys. Chem. B*, 2014, **8**, 626

CHAPTER 2

2.0 Exploring the Coordination Chemistry of Terpy-Type Boratriazine Ligands

Thanks to the tridentate terpy-like coordination pocket in 2,2-difluoro-4,6-bis(2-pyridyl)-1,3-dihydro-1,3,5,2-triazaborinine (Py_2F_2BTA) and 2,2-difluoro-4,6-bis(2-pyrimidinyl)-1,3-dihydro-1,3,5,2-triazaborinine (Pm_2F_2BTA), we can take advantage of the ligating properties of these boratriazines with a variety of metal ions. As it is possible to maintain the chelating ability of these compounds while tuning the physical properties of the constructs, this strategy may allow access to interesting photocatalytic activities due to the photoactive features of the system. For example, iron-based complexes, which are often characterized by favourable light absorption properties in the visible region of the electromagnetic spectrum, have been shown to exhibit photocatalytic properties using relatively inexpensive sources of visible light (e.g., light emitting diodes).[1,2] Complexes of cobalt are also known to have interesting photophysical properties, with applications in dye-sensitized solar cells,[3] in the construction of fluorescent nanomaterials,[4] as well as in photodynamic therapy for cancer treatment.[5] Additionally, owing to the state of their electronic configurations, complexes of iron and cobalt have been exploited for their ability to host interesting magnetic properties, such as spin crossover systems and single molecule magnets.[6–8] These compounds have also found many applications in catalyzing such processes as cross coupling reactions, C–N, C–P, and C–S bond formations, redox chemistry etc.[9,10]

Due to the high natural abundance of both iron and cobalt, and their relatively nontoxic nature,[11,12] these metal salts represent excellent and economic alternatives to precious metals. As such, we have guided our investigation into the reactivity and coordination behaviours of our BTA ligands with 3d transition metals, iron and cobalt in particular. This chapter is subdivided such that structurally related complexes are group together. In the first section, the synthesis of a series of mononuclear iron (III) halide constructs will be discussed, alongside the impact ligand exchange has on their frontier molecular orbitals. Next, the structural analysis of oxo-bridged dinuclear iron (III) compounds will be analyzed. The third section addresses BTA-based compounds of mononuclear iron and cobalt (II) structures, and lastly, cobalt complexes bound by multiple BTA ligands are discussed.

2.1.1 Synthesis and Structural Analysis of Mononuclear Boratriazine-Based Iron (III) Halide Complexes

Investigation into the reactivity and coordination behaviours of our BTA ligands with 1st row transition metals was first oriented towards the synthesis of a series of mononuclear iron (III) complexes. The use of metal halide salts in coordination can be advantageous due to the ease of synthesis of their complexes, as well as for their ability to undergo further chemistry through substitution of the halogens, an important aspect with respect to small molecule activation.

To that end, we have prepared and structurally characterized a series of related iron (III) halides, namely $[Fe^{III}Cl_3(Py_2F_2BTA)]\cdot MeCN$ (**2.1a**), $[Fe^{III}Cl_3(Py_2F_2BTA)]\cdot 2DMF$ (**2.1b**), $[Fe^{III}Cl_3(Py_2F_2BTA)]\cdot 2DMA$ (**2.1c**), $[Fe^{III}Cl_2(Py_2F_2BTA)(MeOH)]Cl$ (**2.2**), $[Fe^{III}Cl_2(Py_2F_2BTA)(EtOH)]Cl$ (**2.3**), $[Fe^{III}Cl_3(Pm_2F_2BTA)]\cdot(MeOH)(MeCN)$ (**2.4**), $[Fe^{III}Br_3(Pm_2F_2BTA)]$ (**2.5**), $[Fe^{III}Cl_3(Py_2(OMe)_2BTA)]$ (**2.6**), and $[Fe^{III}Br_3(Py_2(OMe)_2BTA)]$ (**2.7**).

In our investigation of the ligating properties of our BTA ligands, we have employed chloride and bromide iron salts of differing oxidation states alongside various coordinative solvents. As highlighted in Scheme 2.1, by altering the reaction conditions, we were able to isolate a family of mononuclear Fe^{III} complexes.

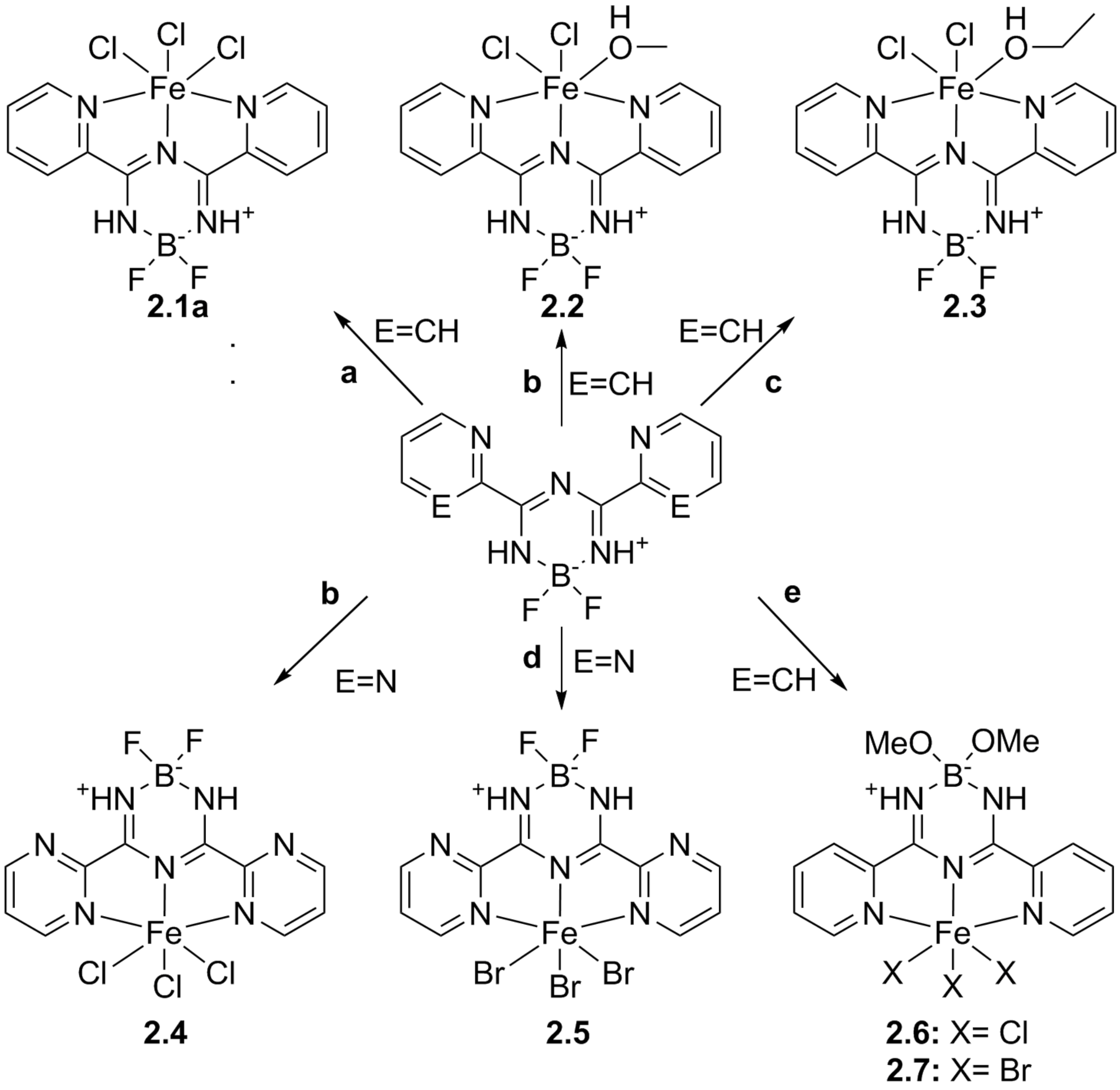

Scheme 2.1 – Synthesis of compounds **2.1-2.7**. Reagents and conditions: (a) $FeCl_3$, MeCN; (b) $FeCl_3$, MeCN, MeOH; (c) $FeCl_3$, MeCN, EtOH; (d) $FeBr_3$, MeOH; (e), FeX_2 (where X = Cl or Br), MeOH.

With respect to the first set of complexes, **2.1-2.3**, the key differentiating feature between the reactions to isolate these compounds was the choice of solvent. For example, a mononuclear iron complex can be achieved by reacting $FeCl_3$ and Py_2F_2BTA in acetonitrile (MeCN). After stirring for a few minutes this solution can be filtered and capped, affording yellow plates suitable for single crystal X-ray analysis (SCXRD) of

$[\mathrm{Fe^{III}Cl_3(Py_2F_2BTA)}]\cdot\mathrm{MeCN}$, (**2.1a**). Conversely, if the solution is stirred longer (30 minutes), a yellow precipitate with the same IR signature as compound **2.1a** forms. By placing either a dimethylformamide (DMF) or dimethylacetamide (DMA) solution of the isolated solid in a diethyl ether bath, crystals of $[\mathrm{Fe^{III}Cl_3(Py_2F_2BTA)}]\cdot\mathrm{2DMF}$ (**2.1b**) and $[\mathrm{Fe^{III}Cl_3(Py_2F_2BTA)}]\cdot\mathrm{2DMA}$ (**2.1c**), are afforded as orange needles and orange blocks, respectively, suitable for SCXRD (Figure 2.1).

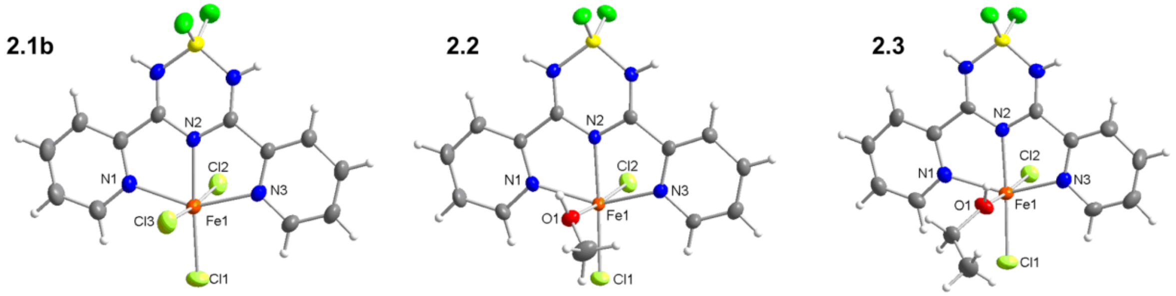

Figure 2.1 – Structural diagram of **2.1b**, **2.2**, and **2.3** illustrating their asymmetric units with 50% thermal ellipsoids. DMF in **2.1b** and chloride counterions in **2.2** and **2.3** are omitted for clarity. Compounds **2.1a** and **2.1c** are omitted from the scheme due to being isostructural to **2.1b**.

Complexes **2.1a**, **2.1b**, and **2.1c** crystallize in the orthorhombic *Pbca*, the triclinic $P\overline{1}$, and the monoclinic $P2_1/m$ space groups, respectively. Compound **2.1c** lies on a symmetry element which divides its molecular unit about the centre of the boratriazine ring of $\mathrm{Py_2F_2BTA}$. The molecular units of **2.1** contains an $\mathrm{Fe^{III}}$ central ion coordinated in *mer* fashion to a neutral $\mathrm{Py_2F_2BTA}$ ligand. The coordination environment about the metal centre is completed by three chloride anions. As such, the metal centres adopt a six-coordinate arrangement which are best described as distorted octahedra, as determined using the SHAPE software (Table 2.1 and Figure 2.2).[13]

Table 2.1 – Shape analysis of compounds **2.1–2.7**. Ideal geometry is a zero value, distortion from this geometry increases the value of the continuous shape measures.

	HP-6	**PPY-6**	**OC-6**	**TBR-6**	**JPPY-6**
2.1a	33.81	24.94	1.86	13.91	28.35
2.1b	33.21	23.28	2.17	12.17	26.63
2.1c	34.05	23.87	1.97	13.81	27.28
2.2	33.38	24.89	1.93	14.11	28.43
2.3	33.42	24.53	1.88	14.41	28.09
2.4	33.38	24.58	2.04	12.68	27.99
2.5	34.28	24.64	2.39	14.24	27.75
2.6	33.84	24.10	1.91	13.77	27.42
2.7	34.39	24.88	2.33	15.15	27.15

HP-6: D_{6h}, Hexagon; PPY-6: C_{5v}, Pentagonal pyramid; OC-6: O_h, Octahedron; TPR-6: D_{3h}, Trigonal prism; JPPY-6: C_{5v}, Johnson pentagonal pyramid J_2.

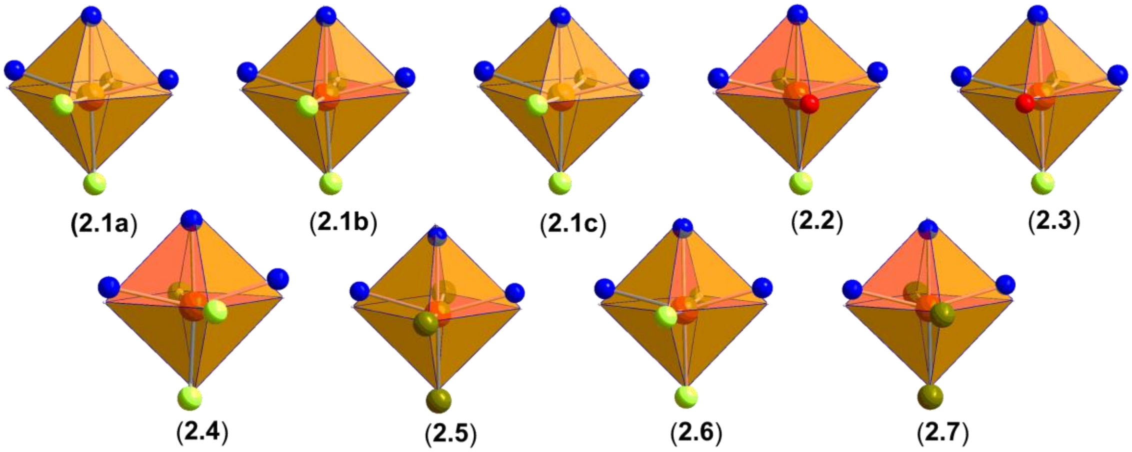
(2.1a) **(2.1b)** **(2.1c)** **(2.2)** **(2.3)**
(2.4) **(2.5)** **(2.6)** **(2.7)**

Figure 2.2 – Visual depiction of the distortion from ideal octahedral geometry in compounds **2.1**-**2.7**.

Interestingly, changing the solvent system of the above described reaction to a 1:1 mixture of methanol (MeOH) and MeCN does not afford a precipitate. Instead, here the solution was sealed and left to stand for several days, upon which time [$Fe^{III}Cl_2(Py_2F_2BTA)(MeOH)$]Cl (**2.2**) was isolated as yellow plates, as confirmed through SCXRD. Following a similar procedure, complex **2.3** can be prepared by replacing MeOH with ethanol (EtOH), affording [$Fe^{III}Cl_2(Py_2F_2BTA)(EtOH)$]Cl as yellow plates suitable for SCXRD (Figure 2.1). In the latter two complexes, changing the solvent system leads to substitution of an axial chloride ligand for a solvent molecule, either MeOH or EtOH, resulting in the displaced chloride being retained in the crystal lattice as a counterion. Consequently, both **2.2** and **2.3** crystallize in the non-centrosymmetric orthorhombic $Pca2_1$ space group. Nonetheless, a six-coordinate environment about the central metal ion in **2.2** and **2.3** is formed similar to that of **2.1**, which are also best described as distorted octahedra (Table 2.1 and Figure 2.2).

Upon changing the ligand framework to the pyrimidyl derivative, Pm_2F_2BTA, the tendency for substitution of an axial chloride ion for an alcoholic solvent molecule is no longer observed. For example, upon placing a solution of $FeCl_3$ and Pm_2F_2BTA in a 1:1 mixture of MeOH and MeCN into a diethyl ether bath, orange needles of $[Fe^{III}Cl_3(Pm_2F_2BTA)]\cdot(MeOH)(MeCN)$ (**2.4**) suitable for SCXRD analysis were obtained (Figure 2.3). As well, the bromide analogue, $[Fe^{III}Br_3(Pm_2F_2BTA)]$ (**2.5**), can be isolated as red plates by leaving a sealed solution of $FeBr_3$ and Pm_2F_2BTA in MeOH to stand for several days. Crystals of **2.4** and **2.5** belong to the monoclinic $P2_1/c$ and triclinic $P\overline{1}$ space groups, respectively. The asymmetric units for complexes **2.4** and **2.5** both consist of a six coordinate Fe^{III} central ion coordinated in *mer* fashion to a Pm_2F_2BTA ligand, with three halide ions completing the coordination environment, similar to **2.1-2.3**.

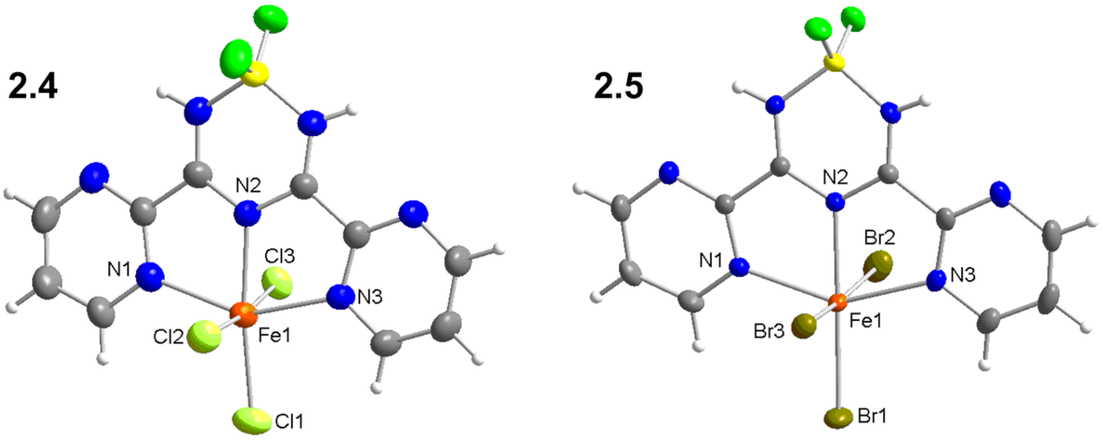

Figure 2.3 – Structural diagram of **2.4** and **2.5** illustrating their asymmetric units with 50% thermal ellipsoids. MeOH and MeCN in **2.4** are omitted for clarity.

In addition to substitution of an axial chloride ligand for a solvent molecule, either MeOH or EtOH, when the pyridyl ligand Py_2F_2BTA was employed, other modifications can be achieved by changing the oxidation of the metal salt. More specifically, upon reacting Py_2F_2BTA under a regular atmosphere with either $FeCl_2$ or $FeBr_2$ in MeOH and allowing the solutions to stand for several days, replacement of the fluoride ions on the Py_2F_2BTA ligand for methoxy groups occurs as confirmed through SCXRD analysis (Figure 2.4). The substitution of boron bound fluoride anions on bodipy-type frameworks for oxy substituents is well documented and can be a useful strategy in tuning the photophysical properties of the compound; however, such reactions typically require the use of a strong base.[14] In the case of Py_2F_2BTA, the free ligand is indeed stable in methanolic solutions, even when stirred overnight with excess triethylamine or at reflux. The addition of sodium methoxide or sodium bicarbonate can, however, promote substitution, with the reactions appearing to be at equilibrium under mild (RT) reaction conditions. Based on these preliminary results, the replacement of the fluoride ions for methoxy groups in **2.6** and **2.7** may be attributed to an aerobic metal-mediated process.

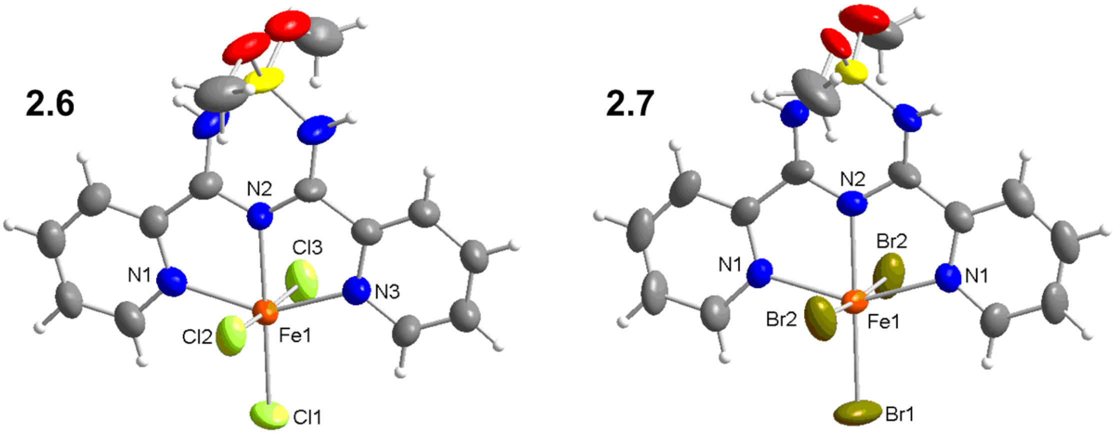

Figure 2.4 – Structural diagram of **2.6** and **2.7** illustrating their molecular units with 50% thermal ellipsoids. 50% positional disorders are present in both structures.

Crystals of **2.6** form as orange plates and belong to the orthorhombic *Pna*2_1 space group, while **2.7** crystallizes in the monoclinic *C*2/*c* space group as red plates. Although **2.6** and **2.7** belong to different space groups, the coordination environment about the central iron ions have significant similarities. In both cases, the central metal ion is six-coordinate binding three halide ions and a neutral molecule of $Py_2(OMe)_2BTA$, which coordinates in *mer*-fashion, with the BTA moiety exhibiting positional disorder of 50%. The asymmetric unit of **2.7** contains an internal plane of symmetry which runs through the centre of the boratriazine ring. Based on charge balance, along with the similarities to complexes **2.1**-**2.5**, an oxidation state of +3 for the central iron ion was determined.

In complexes **2.1**-**2.7**, the Fe–N bond lengths corresponding to the nitrogen atoms of the flanking pyridyl and pyrimidyl groups on Py_2F_2BTA and Pm_2F_2BTA are essentially equivalent, while the Fe–N bonds to the central BTA moieties are shorter (Table 2.2). Such features are commonly observed in terpy-based coordination complexes.[15–18]

Table 2.2 – Selected bond distances (Å) for compounds **2.1b**, and **2.2**-**2.7**.

	2.1b	**2.2**	**2.3**	**2.4**	**2.5**	**2.6**	**2.7**
Fe1-N1	2.1496(12)	2.125(3)	2.122(5)	2.142(8)	2.136(5)	2.149(4)	2.1803(19)
Fe1-N2	2.0956(13)	2.084(3)	2.095(5)	2.112(7)	2.103(7)	2.114(3)	2.112(2)
Fe1-N3	2.1594(12)	2.125(3)	2.116(6)	2.134(8)		2.161(4)	2.193(2)
Fe1-Cl1	2.2582(6)	2.2287(10)	2.228(2)	2.239(3)		2.2436(16)	
Fe1-Cl2	2.3600(5)	2.2896(10)	2.3043(19)	2.359(3)		2.3125(18)	
Fe1-Cl3	2.3522(5)			2.337(3)		2.3980(18)	
Fe1-O1		2.148(3)	2.105(5)				
Fe1-Br1					2.3793(16)		2.3936(5)
Fe1-Br2					2.5142(10)		2.4573(4)
Fe1-Br3							2.5432(5)

Solvatomorphs (**2.1a** and **2.1c**) of compound **2.1b** are omitted from this table.

Although the coordination environment about the central Fe^{III} ion in complexes **2.1**-**2.7** are all best described as distorted octahedra, the various alterations (e.g., halides, alkoxy groups) and supramolecular interactions within this family of complexes influences the level of distortion (Table 2.1 and Figure 2.2). The major source of distortion in these complexes can, however, be attributed to the enforced bite angle of the BTA ligands (148.2°-150.0°), which bind in *mer*-fashion. Substitution of an axial chloride ligand in **2.1** for a neutral alcohol (MeOH in **2.2**; EtOH in **2.3**) shortens the Fe–N bonds (Table 2.2) to the BTA ligand due to an increased electropositive character on the central metal ion, however, the overall differences in the distortion of the geometry are minimal. When the chloride ions in **2.4** and **2.6** are replaced with bromide ions (**2.5** and **2.7**), an increased distortion was observed, which is expected due to the increased size of the anions.

While compounds **2.1**-**2.7** are structurally related on the basis of their molecular units, and all tend to pack in the solid state to form layered arrays (Figure 2.5), the presence or absence of counter anions or solvent in the lattice, as well as the nature of the associated ligands, leads to significant differences between the observed supramolecular structures. For example, in complex **2.1a**, MeCN can be found interspersed between the layers of the metal complexes, which are arranged in a herringbone motif. Apart from one C–H···F hydrogen bond, all short contacts are found to connect with the chlorine atoms. These include one C–H···Cl intermolecular short contact between the solvent and the complex, alongside two N–H···Cl, five C–H···Cl intermolecular, and one intramolecular C–H···Cl interaction between the metal complexes. All hydrogen bonds in this chapter are calculated through the PLATON interface, which uses appropriate D–H···A distances and angles as defined in the literature,[19–21] where D and A are the donor and acceptor atoms, respectively. A list of all short contacts discussed herein are presented at the end of this chapter.

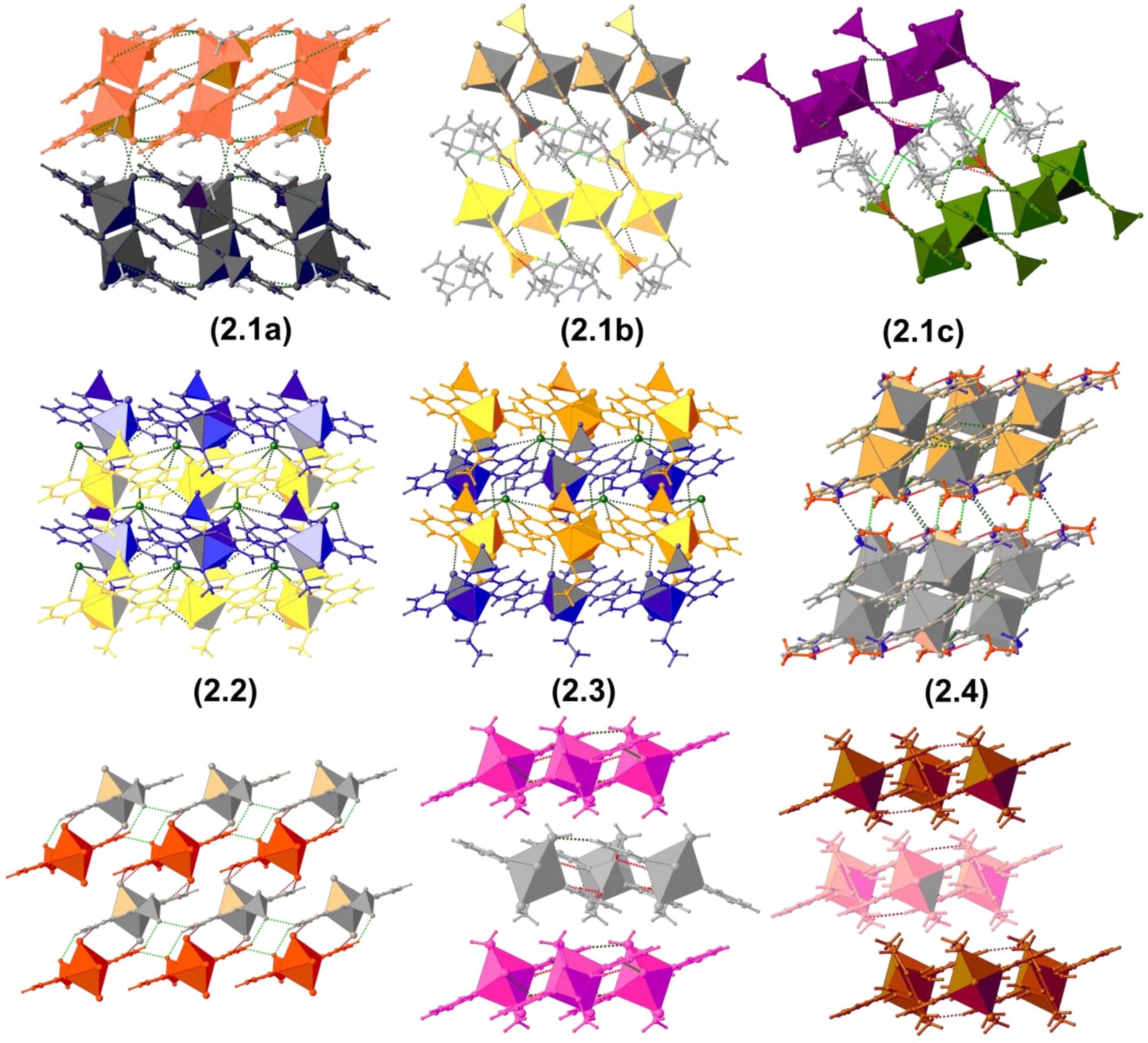

(2.1a) (2.1b) (2.1c)

(2.2) (2.3) (2.4)

(2.5) (2.6) (2.7)

Figure 2.5 – Packing diagrams for compounds **2.1**-**2.7.** Polyhedra are added about the metal centres (octahedra) and boron atoms (tetrahedra) to depict molecular orientation. Different layers are colored in alternating schemes; atoms or molecules in the lattice are colored separately. Possible hydrogen interactions D–H···N (blue), D–H···O (red), D–H···F (light green), D–H···Br (purple), and D–H···Cl (dark green), where D represents the donor atoms, are denoted by dotted lines.

When compared to **2.1a**, complexes **2.1b** and **2.1c** have twice the number of solvent molecules in the crystal lattice, leading to a separation of the layered coordination complexes such that a lamellar type arrangement is observed. This suggests that the use of crystallization solvents having higher hydrogen bonding opportunities through their additional polar groups, such as DMF in **2.1b** and DMA in **2.1c**, play a significant role in forming stable supramolecular assemblies. This is evidenced in the large degree of hydrogen bonding found between Py_2F_2BTA and the solvent molecules in these complexes, which serve to hold the structures together. Complex **2.1b** features solely short contacts with the solvent, these being two N–H···O, one C–H···F, three C–H···Cl, and two C–H···O intermolecular interactions alongside one C–H···O intramolecular hydrogen bond. Complex **2.1c** does feature one C–H···Cl intermolecular interaction between molecules of the metal complex, however, alike compound **2.1b**, the hydrogen bonding is dominated by interactions with the solvent. This includes one intramolecular C–H···O bond, and three N–H···O, three C–H···O, and three C–H···F intermolecular short contacts.

Upon substitution of an axial chloride ion for MeOH (**2.2**) or EtOH (**2.3**), the only non-coordinated specie that exists in the structure is the displaced chloride anion, which leads to a diminishing of the interlayer separation, affording 2D lamellar arrangements. Here, the displaced chloride ions in **2.2** and **2.3** serve as a link between the layers. In the case of complex **2.2**, this results in one O–H···Cl, two N–H···Cl, and one N–H···Cl intermolecular interaction, alongside one C–H···F hydrogen bond. In the case of complex **2.3**, the displaced chloride anion forms all observed hydrogen bonds, which are, three C–H···Cl, one O–H···Cl, and two N–H···Cl interactions.

Molecules of complex **2.4** are found to pack in an alternating face–to–face and end–to–end manner between layers. Additionally, the solvent molecules in the crystal lattice are found to separate the lamellar layers to a small degree, in a similar manner to complex **2.1**. The solvent molecules in this complex give rise to one O–H···N interaction between MeCN and MeOH, with only MeOH interacting with the iron complex through an

N–H···O bond. Additional intermolecular hydrogen bonds between the metal complexes exist in this compound, including one N–H···Cl, two C–H···Cl and one C–H···F short contacts.

Unlike the chloride analogues **2.1** and **2.4**, the bromide derivative **2.5** does not feature any solvent in the lattice. This results in a brick-like arrangement of molecules with few intermolecular (two C–H···F and two N–H···Br) hydrogen contacts. The uncoordinated nitrogen on the pyrimidyl rings are responsible for the formation of two N–H···N intramolecular hydrogen bonds both complexes **2.4** and **2.5**.

Due to the positional disorder in compounds **2.6** and **2.7**, which are dependent on the orientations of the methoxy groups, different D–H···A interactions are possible. Nonetheless, there are two N–H···O, three C–H···O, and one C–H···Cl unique intermolecular contacts in **2.6**, while compound **2.7** hosts three N–H···O, two C–H···O, one C–H···Br and one C–H···N intermolecular hydrogen bond. While compound **2.4** is found to pack in a herringbone motif, the bromido analogue **2.5** arranges in an alternating face–to–end and end–to–face manner between layers. Interestingly, **2.4** and **2.5** are the only two compounds in this family that do not exhibit short contacts between the various layers, which may be attributed to the loss of potential halide interactions through the fluoride ions.

2.1.2 Magnetic Susceptibility Determination for [Fe^{III}Cl$_3$(Py$_2$F$_2$BTA)]·MeCN

Compared to their low spin analogs, high spin compounds exhibit a stronger alignment to the magnetic field, or magnetic susceptibility (denoted by χ), due to having a larger number of unpaired electrons.[22] One method of measuring the spin state of a compound, is through the use of a magnetic susceptibility Johnson Matthey balance (or Evans balance). In an Evans balance, a pair of magnets are placed back to back on a suspension strip, making a balanced system with a homogenous magnetic field at both ends. When a sample, which is placed in a cylindrical glass tube, is introduced into the field of one magnet, a force can be measured upon the second magnet through a negative feedback mechanism. The magnitude of the field induced upon the analyte, which is proportional to the applied field, is termed magnetization (M) and can be written as:

$$\mathrm{B}/\mathrm{H}_0 = 1 + 4\pi(\mathrm{M}/\mathrm{H}_0) = 4\pi\chi_v$$

where B is the net field, H_0 is the applied field strength, M is the magnetization of the sample, and χ_v is a measure of how large the field is induced per unit applied field strength. The volume magnetic susceptibility, χ_v, is a dimensionless quantity that is constant for a given compound at a particular temperature. This can be converted to molar susceptibility, χ_m, which is the induced field on the analyte on a molar basis through the equation:

$$\chi_m = (\chi_v/\mathrm{d})(\mathrm{MW})$$

where d is the density of the analyte of interest and MW the molecular weight. The relationship between the applied magnetic field and the magnetic moments of the analyte can be described in terms of the effective magnetic moment, μ_{eff}, through the equation:

$$\mu_{eff} = \sqrt{\frac{3k\chi_a T}{N\beta^2}} = 2.828\sqrt{\chi_a T}$$

Where k is the Boltzmann's constant, T is the absolute temperature, β is the Bohr Magneton, N is Avogadro's number, and χ_a is χ_m plus the sum of all diamagnetic contributions of the compound. The diamagnetic corrections to the molar susceptibility are made to account for inner core electrons, ligands, atoms and ions of the compound which lower the apparent molar susceptibility. The magnetic moment in the above equation is expressed in Bohr Magneton (B.M.)

Once obtained, the measured μ_{eff} can be compared to literature values for compounds of known spin states. For example, iron (III) with five unpaired electrons (S = 5/2) typically has a magnetic moment of 5.7-6.0 B.M., whereas low spin state compounds of iron (III), with one unpaired electron (S = 1/2), have a magnetic moment of 2.0-2.5 B.M. Compound **2.1a** was chosen for analysis of its magnetic moment using a magnetic susceptibility Johnson Matthey balance due to having a similar ligand field to its chloride analogues. After analysis, a measured μ_{eff} of 7.56 B.M. was determined for compound **2.1a**. This value exceeds the literature values for high spin iron (III), which points to the likelihood for compounds **2.1b**, **2.1c**, and **2.2-2.7**, which share similar coordination geometries, to occupy high spin states at room temperature. It is worth noting that measured u_{eff} values obtained through this method are often higher than the expected ones due to orbital contributions, and zero-field splitting effects.[9]

2.1.3 Ligand Influence on Molecular Orbital Energies of Iron (III) Monomers

In order to better understand the effects of ligand substitution upon the ligand field of compounds **2.1-2.7**, theoretical calculations were employed using the density functional theory (DFT) method. All calculations presented were performed using the Gaussian09 program package.[23] The atomic positions, as elucidated using SCXRD analysis, were used as a starting point for single point energy calculations. Preoptimized molecular geometries and vibrational frequencies of the complexes were used for molecular orbital calculation using the hybrid density functional B3LYP with the 6-31G(d) basis set.[24–26] The calculations performed herein were done assuming high spin states (S = 5/2) for the iron (III) complexes. The high magnetic susceptibility (μ_{eff} = 7.56 B.M.) of compound **2.1a** helps support this assumption.

DFT calculations reveal that the electron density in the lowest unoccupied molecular orbitals (LUMO) in compounds **2.1**-**2.7** is delocalized onto the aromatic rings as well as the central boratriazine ring (Figures 2.6 and 2.7). Upon substitution of a chloride ligand in **2.1** for a molecule of alcohol in **2.2**-**2.3**, a decrease in the symmetry of the orbitals is observed. alongside a small increase in the LUMO energy (~0.04eV, Figure 2.8). Changing from the pyridyl to the pyrimidyl ligand system (**2.1** to **2.4**) causes an increase in stability of the LUMO energies by nearly 0.35 eV. This observation is consistent with theoretical calculations performed on the unbound ligands.[27] Substitution of chloride anions in **2.4** and **2.6** for bromide ions in **2.5** and **2.7** leads to a slight increase in the calculated LUMO energies. This may be due to the increased distortion in the geometries of these compounds, causing a less effective sharing of electrons throughout the structure. Modification of the anionic substituent on the boron atom, in **2.1**, for methoxy groups, in **2.6**, also lead to slight increase in the LUMO energy of the compound. This could be attributed to a small difference in the effective electropositive character of the boron atom.

The highest occupied molecular orbitals (HOMO) are the most affected by substitution of the anionic ligands on the metal centres. Replacement of a chlorine atom, in **2.1**, for alcohol substituents, in **2.2**-**2.3**, leads to a significant increase in the HOMO energies and thus decrease in the HOMO-LUMO energy gap. This can be visualized in Figure 2.6, where the HOMO electron density of compounds **2.2** and **2.3** resides preferentially on the displaced chloride anion. In all other complexes (**2.1**, and **2.4**-**2.7**) the electron density of the HOMO is shared between the central metal ion and the ligated atoms. Substitution of the chloride anions in **2.4** and **2.6** for bromide in **2.5** and **2.7** leads to a significant decrease (~0.4eV) in the calculated HOMO energies.

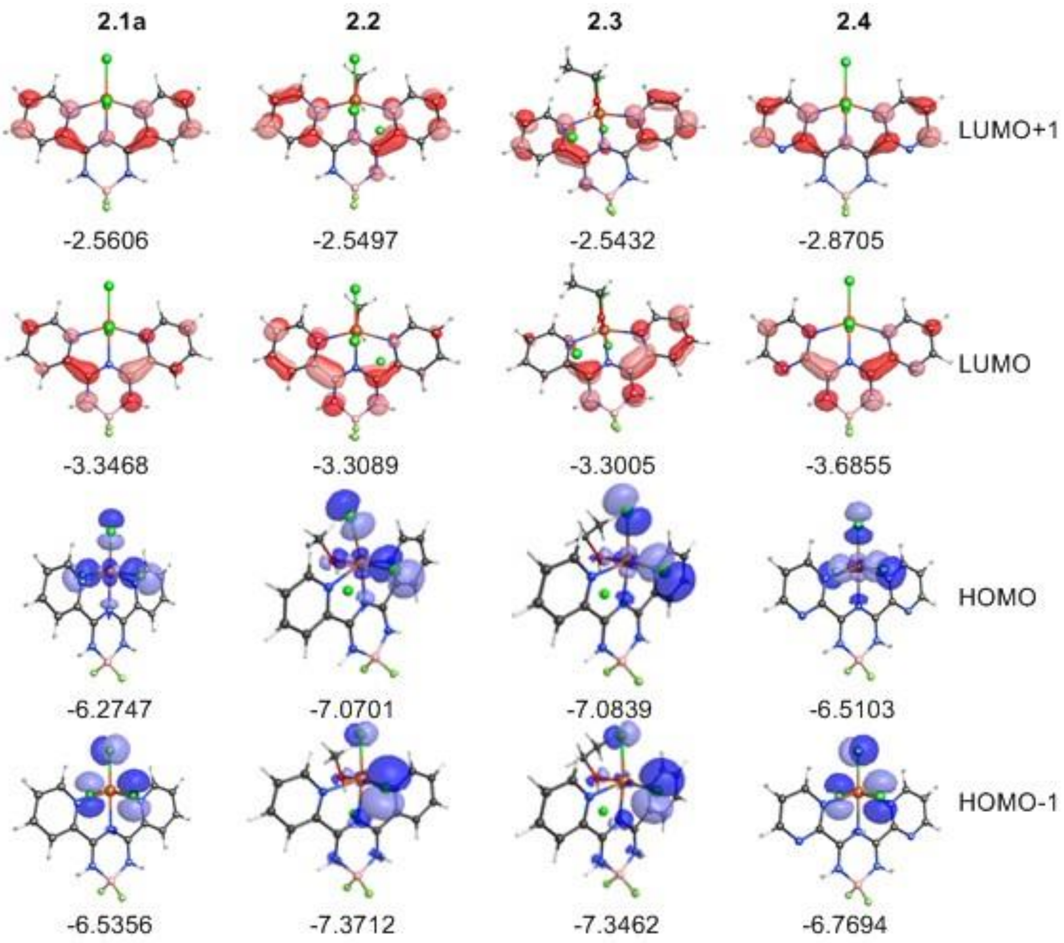

Figure 2.6 – Frontier molecular orbitals and corresponding energies (in eV) for **2.1a**, and **2.2-2.4**.

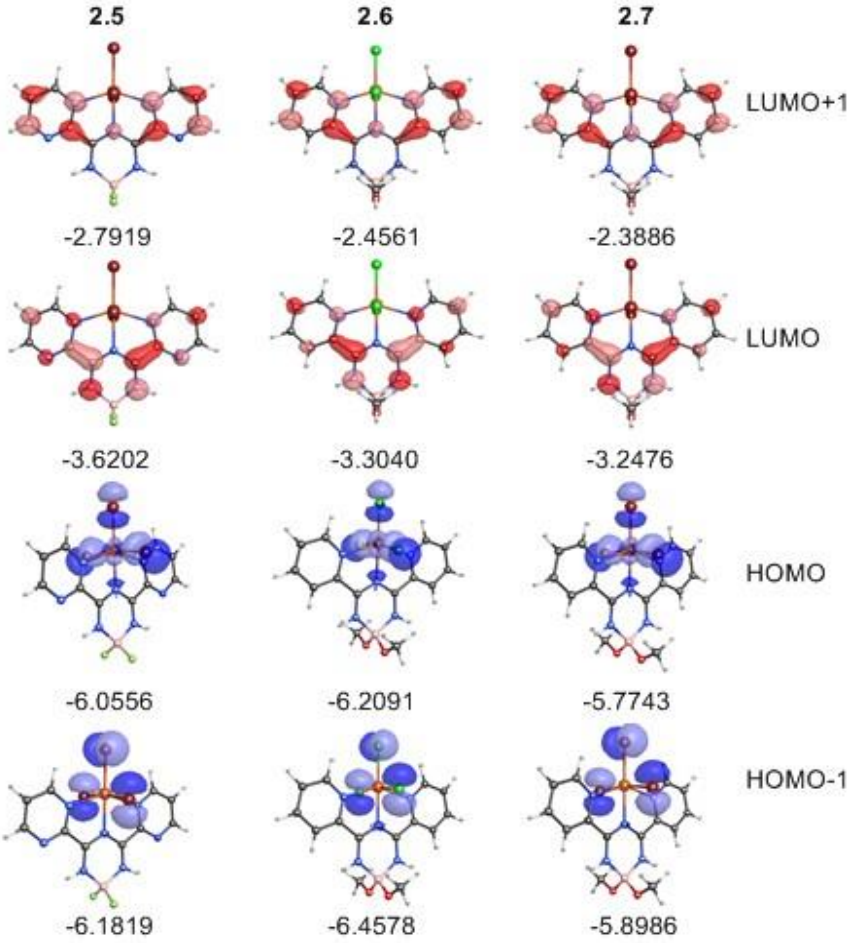

Figure 2.7 – Frontier molecular orbitals and corresponding energies (in eV) for **2.5-2.7**.

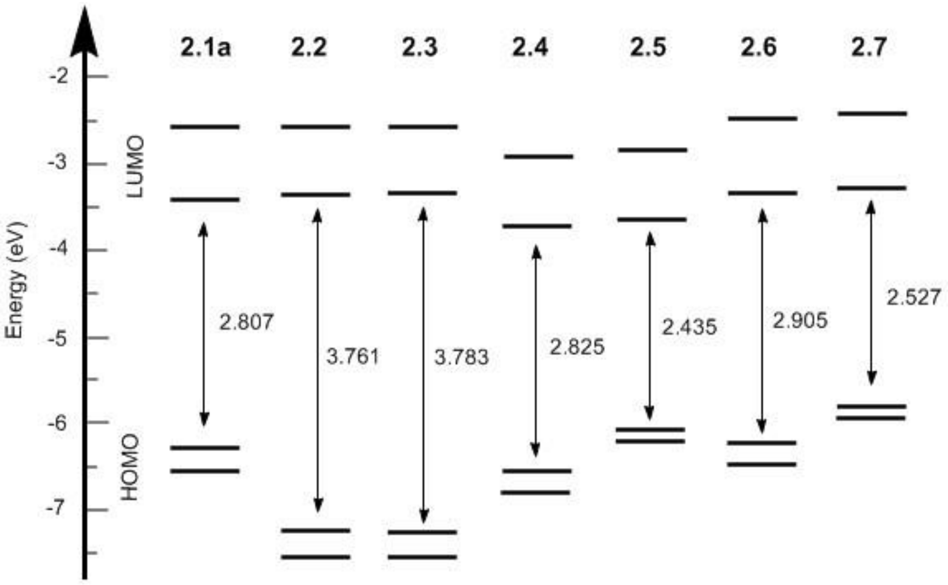

Figure 2.8 – Energy level diagram for the frontier orbitals of **2.1a**, and **2.2-2.7**.

By analysing the singly occupied molecular orbitals (SOMOs) of these octahedral complexes, perturbations in ligand field energies can also be described (Figure 2.9). Complex **2.1a** features a splitting energy of 0.33 eV between its E_g and T_{2g} set of frontier orbitals. Upon substitution of an axial chloride ligand in **2.1a** for neutral alcohols, increased splitting energies between the E_g and T_{2g} sets of orbitals are observed, with a separation of 0.84 eV and 0.89 eV being observed in complexes **2.2** and **2.3**, respectively. This increase in splitting energies is expected due to the substitution of weak field ligands for medium field ligands. The iron trichloride complexes **2.1a**, **2.4**, and **2.6**, were observed to share similar splitting energies, with the pyrimidyl complex **2.4** exhibiting a slightly larger splitting than its pyridyl analogue **2.1a**. Lastly, an increased separation of ~0.08 eV was observed upon substitution of the weaker field chloride ligands in **2.4** and **2.6** for stronger field bromide ligands in **2.5** and **2.7**.

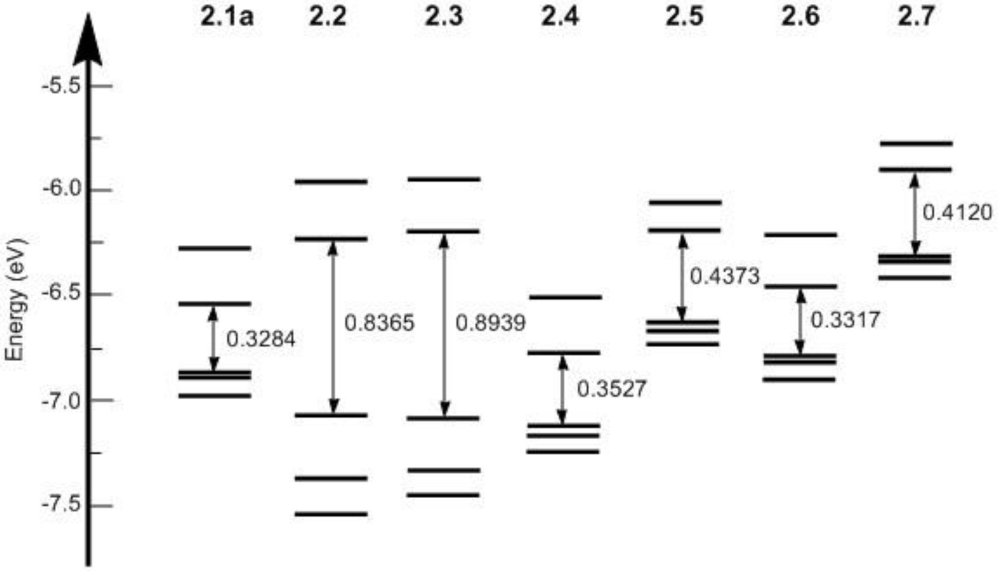

Figure 2.9 – Visual representation of SOMO energies in complexes **2.1a**, and **2.2-2.7**.

2.2 Synthesis and Structural Analysis of Boratriazine-Based Dinuclear Coordination Compounds Bridged through an Oxo Ligand

Dinuclear oxo-bridged iron complexes have become the subject of considerable attention in recent years for their interesting catalytic activities.[9] In proteins, the diferric Fe–O–Fe unit is responsible for storage and the reductive activation of molecular oxygen.[28–30] In synthesized dinuclear complexes, oxo bridged iron (III) compounds have seen use in the formation of important pharmacophores,[31] as potential photocytotoxic anti-cancer agents,[32] as well as in photocatalysis.[33–35] Additionally, magnetic interactions mediated through the Fe–O–Fe of an oxo-bridged dinuclear iron (III) has been reported leading to the development of magnetic anti-cancer agent. In this report, the low Fe–O–Fe angle of 146.36° was theorized to play an important role in the generation of the observed magnetism.[36]

Most terpy-based systems tend to prefer forming mononuclear species upon metal coordination; however, there exists several examples of dinuclear species being formed in serendipitous manner upon reacting with the appropriate metal salts (e.g., chlorides, hydroxides, oxides, nitrates, etc).[37–39] Using similar iron sources, we have observed the formation of six structurally related dinuclear iron (III) structures connected through a single μ-oxo bridging ligand. More specifically, here-in are presented the syntheses and crystal structures of $[\{Fe^{III}(NO_3)(Py_2F_2BTA)(H_2O)\}_2(\mu\text{-}O)](NO_3)_2\cdot4DMA$ (**2.8**), $[\{Fe^{III}(NO_3)(Pm_2F_2BTA)(H_2O)\}_2(\mu\text{-}O)](NO_3)_2\cdot4DMA$ (**2.9**), $[\{Fe^{III}(NO_3)(Py_2F_2BTA)(MeOH)\}_2(\mu\text{-}O)](NO_3)_2$ (**2.10**), $[\{Fe^{III}(NO_3)(terpy)(H_2O)\}_2(\mu\text{-}O)](NO_3)_2$ (**2.11**), $[\{Fe^{III}(NO_3)(terpy)(MeOH)\}_2(\mu\text{-}O)](NO_3)_2$ (**2.12**), and $[\{Fe^{III}(NCS)_2(Py_2F_2BTA)\}_2(\mu\text{-}O)]\cdot MeOH$ (**2.13**). Although the inclusion of the bridging oxygen occurred serendipitously, we have demonstrated the targeted synthesis of oxo bridged dinuclear iron compounds with tridentate chelates (Scheme 2.2).

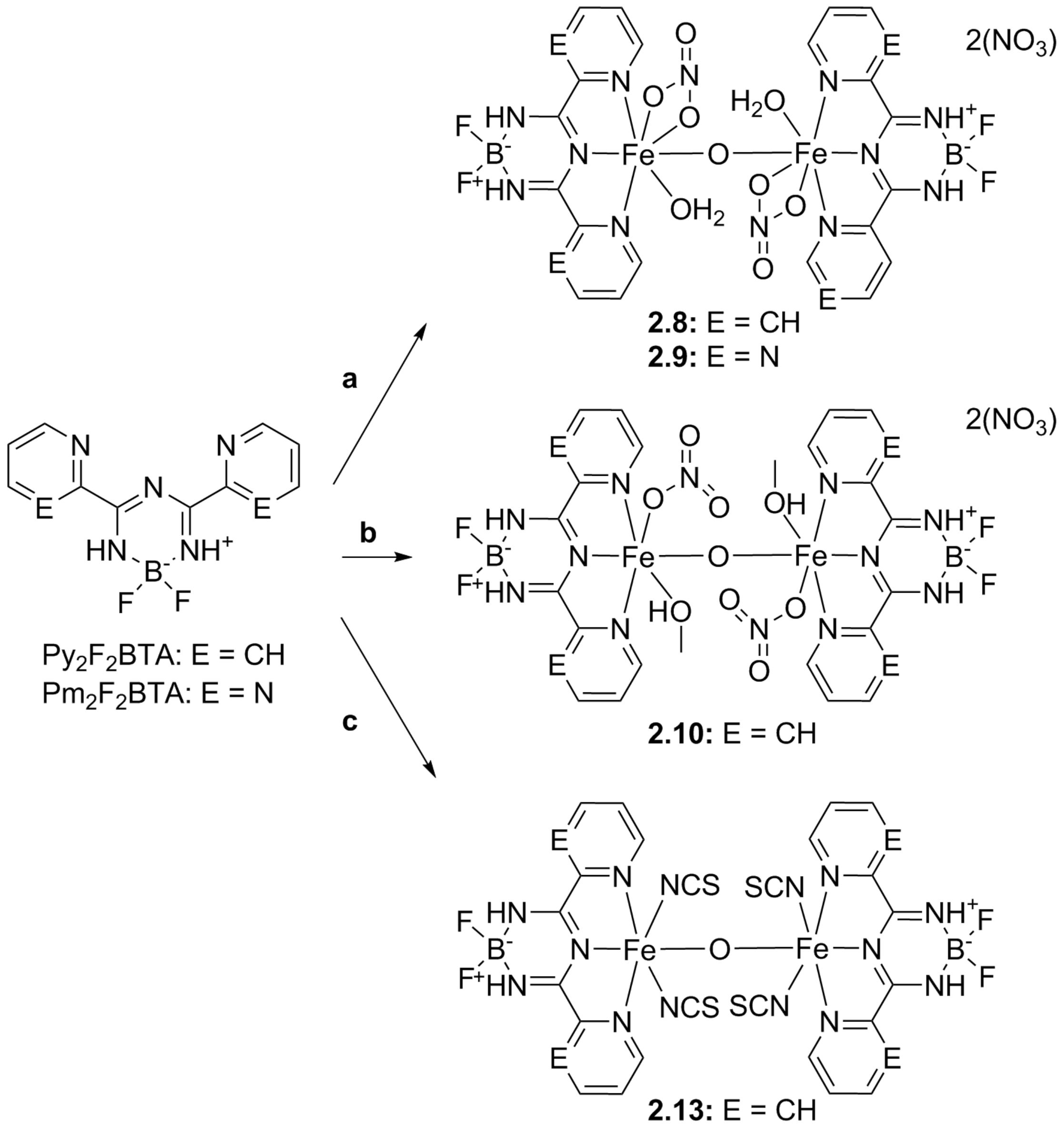

Scheme 2.2 – Synthesis of compounds **2.8**-**2.10** and **2.13**. Reagents and conditions: (a) $Fe(NO_3)_3$, EtOH, DMA; (b) $Fe(NO_3)_3$, dry MeOH; (c) $FeCl_3$, KSCN, MeCN, H_2O.

For comparative purposes, terpy complexes were studied under similar reaction conditions. To this effect, we successfully prepared the terpy analogues of compounds **2.8-2.10**, yielding complexes **2.11** and **2.12** (Scheme 2.3), demonstrating the versatility of the reaction. This shows that, through the use of tridentate ligands possessing of rigid conformations, it is possible to influence the molecular arrangement of the resulting complexes. This effectively opens up the possibility for the synthesis of future analogues.

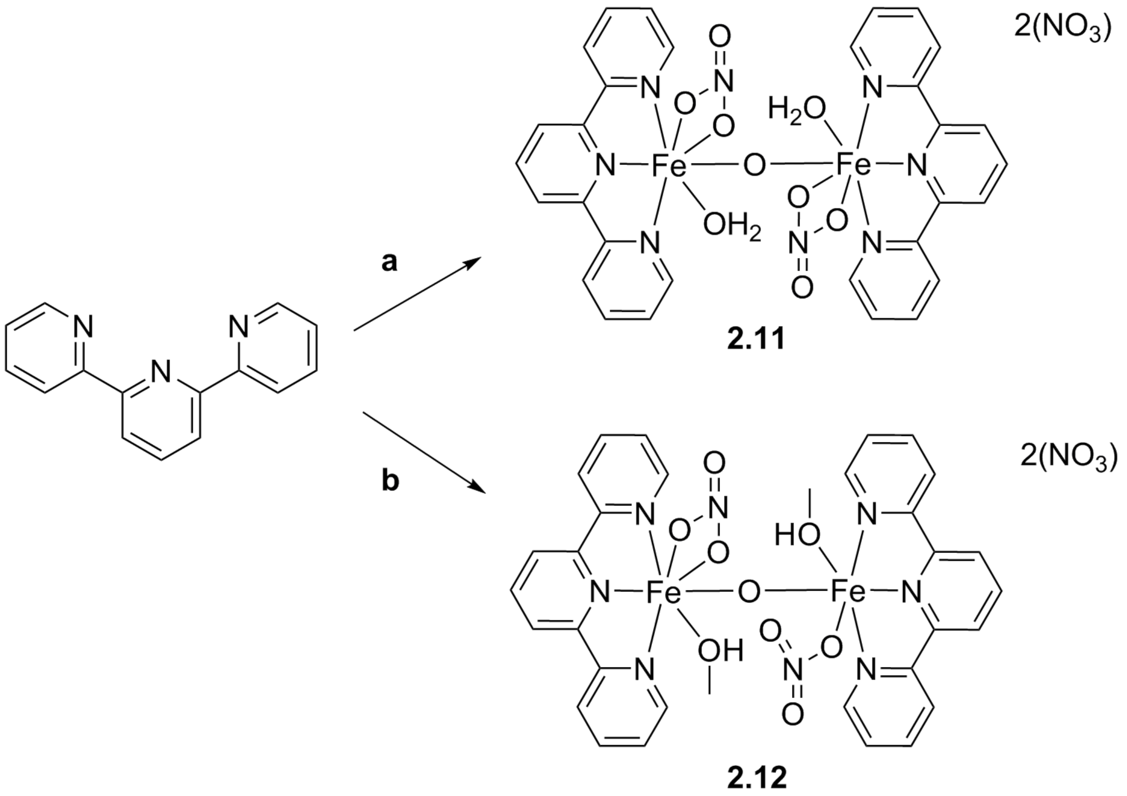

Scheme 2.3 – Synthesis of compounds **2.11-2.12**. Reagents and conditions: (a) $Fe(NO_3)_3$, EtOH; (b) $Fe(NO_3)_3$, dry MeOH.

It is worthwhile noting that attempts to isolate these compounds under dry conditions led to the production of non-crystalline material possessing of different IR spectra in all cases. This indicates that water is likely a necessary component for the formation of these complexes. The dinuclear Fe^{III} complexes **2.8** and **2.9** were achieved through similar procedures, with the sole differentiation being the ligand employed in coordination. For example, reacting the Py_2F_2BTA or Pm_2F_2BTA ligand with $Fe(NO_3)_3$ in EtOH affords the precipitation of the desired complexes **2.8** and **2.9** as orange or brown powders, respectively. By placing a DMA solution of the isolated solids in a diethyl ether bath, both $[\{Fe^{III}(NO_3)(Py_2F_2BTA)(H_2O)\}_2(\mu\text{-}O)](NO_3)_2\cdot 4DMA$ (**2.8**) and $[\{Fe^{III}(NO_3)(Pm_2F_2BTA)(H_2O)(NO_3)\}_2(\mu\text{-}O)](NO_3)_2\cdot 4DMA$ (**2.9**) are afforded as orange blocks suitable for SCXRD analysis (Figure 2.10 and Table 2.3). Although complexes **2.8** and **2.9** have similar coordination environments and crystallize in the same monoclinic $P2_1/c$ space group, they differ based on the identity of their asymmetric units. More specifically, compound **2.8** has an internal plane of symmetry located on the bridging oxo ligand, causing both Fe^{III} centres of the dimer to be equivalent, while compound **2.9** lacks this element. Regardless, both molecular units feature two Fe^{III} central ions, each coordinated in *mer* fashion to a neutral BTA ligand and are bridged by a single oxygen atom. The coordination environment is completed on each iron by one bidentate nitrate ion, and one water molecule. As such, the metal ions in both structures adopt coordination geometries best described as distorted pentagonal bipyramids (Table 2.4 and Figure 2.11), as determined by the SHAPE software.[13] The main source of distortion in these structures arise from the bidentate bound nitrate (bite angles: 55.33-55.66°). In both structures, two nitrate counterions and four molecules of DMA are found in the crystal lattice. As well, the BTA moieties are found to be oriented opposite one another in parallel planes.

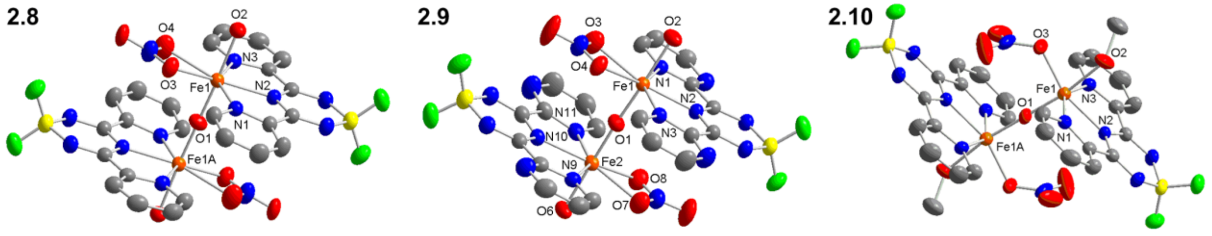

Figure 2.10 – Structural diagram of **2.8**, **2.9**, and **2.10** illustrating their molecular units with 50% thermal ellipsoids. Hydrogen atoms, counter ions and solvent molecules are omitted for clarity.

Table 2.3 – Select bond lengths (Å) for complexes **2.8-2.13**.

	2.8	**2.9**	**2.10**	**2.11**	**2.12**	**2.13**

Fe1–O1	1.7638(2)	1.7668(13)	1.7707(5)	1.7630(3)	1.7726(14)	1.781(5)
Fe1–O2	2.0408(14)	2.0138(15)	2.129(3)	2.0610(15)	2.0846(18)	
Fe1–O3	2.1978(14)	2.3557(18)	1.972(6)	2.3384(17)	2.2766(16)	
Fe1–O3*			2.190(17)			
Fe1–O4	2.3449(18)	2.1733(15)		2.2244(16)	2.2668(18)	
Fe1–N1	2.2547(14)	2.2444(15)	2.163(3)	2.2342(15)	2.2318(19)	2.136(8)
Fe1–N2	2.1373(14)	2.1380(15)	2.087(3)	2.1497(15)	2.1417(17)	2.134(7)
Fe1–N3	2.2406(14)	2.2712(15)	2.169(3)	2.2427(14)	2.2434(18)	2.158(8)
Fe1–N6						2.069(8)
Fe1–N7						2.061(8)
Fe2–O1		1.7639(13)			1.7642(15)	1.790(5)
Fe2–O5						
Fe2–O6		2.0293(15)			2.1301(18)	
Fe2–O7		2.2834(17)			2.0018(17)	
Fe2–O8		2.2057(16)				
Fe2–N5					2.1406(19)	
Fe2–N6					2.1023(19)	
Fe2–N7					2.1444(19)	
Fe2–N8						2.165(7)
Fe2–N9		2.2606(16)				2.138(7)
Fe2–N10		2.1409(16)				2.153(7)
Fe2–N11		2.2646(17)				
Fe2–N13						2.007(9)
Fe2–N14						2.129(8)

(*) denotes a 50% positional disorder about the ligand.

Table 2.4 – Shape analysis of compounds **2.8-2.13**. Ideal geometry is a zero value, distortion from this geometry increases the value of the continuous shape measures.

	2.8	**2.9**	**2.10**	**2.11**	**2.12**	**2.13**
HP-6			31.29, 33.50		40.00	33.09, 33.09
PPY-6			18.18, 22.54		23.15	23.68, 26.15
OC-6			4.22, 2.77		2.15	1.67, 1.40
TPR-6			8.42, 10.55		11.28	12.38, 13.51
JPPY-6			21.63, 26.07		27.31	27.70, 30.09
HP-7	32.83	32.96, 32.90		32.56	33.29	
HPY-7	24.31	23.98, 23.90		23.71	24.60	
PBPY-7	1.16	1.06, 1.20		1.08	0.99	
COC-7	7.72	8.27, 8.02		8.63	7.99	
CTPR-7	6.19	6.55, 6.41		6.49	6.04	
JPBPY-7	2.21	2.08, 2.13		2.19	2.28	
JETPY-7	23.44	24.26, 24.07		23.81	23.44	

HP-6: D_{6h}, Hexagon; PPY-6: C_{5v}, Pentagonal pyramid; OC-6: O_h, Octahedron; TPR-6: D_{3h}, Trigonal prism; JPPY-6: C_{5v}, Johnson pentagonal pyramid J_2, HP7: Heptagonal, D_{7h}, HPY-7: Hexagonal pyramid, C_{6v}, PBPY-7: Pentagonal bipyramid, D_{5h}, COC-7: Caped octahedron, C_{3v}, CTPR-7: Capped trigonal prism, C_{2v}, JPBPY-7: Johnson pentagonal bipyramid J_{13}, D_{5h}, JETPY-7: Elongated triangular pyramid J_7, C_{3v}.

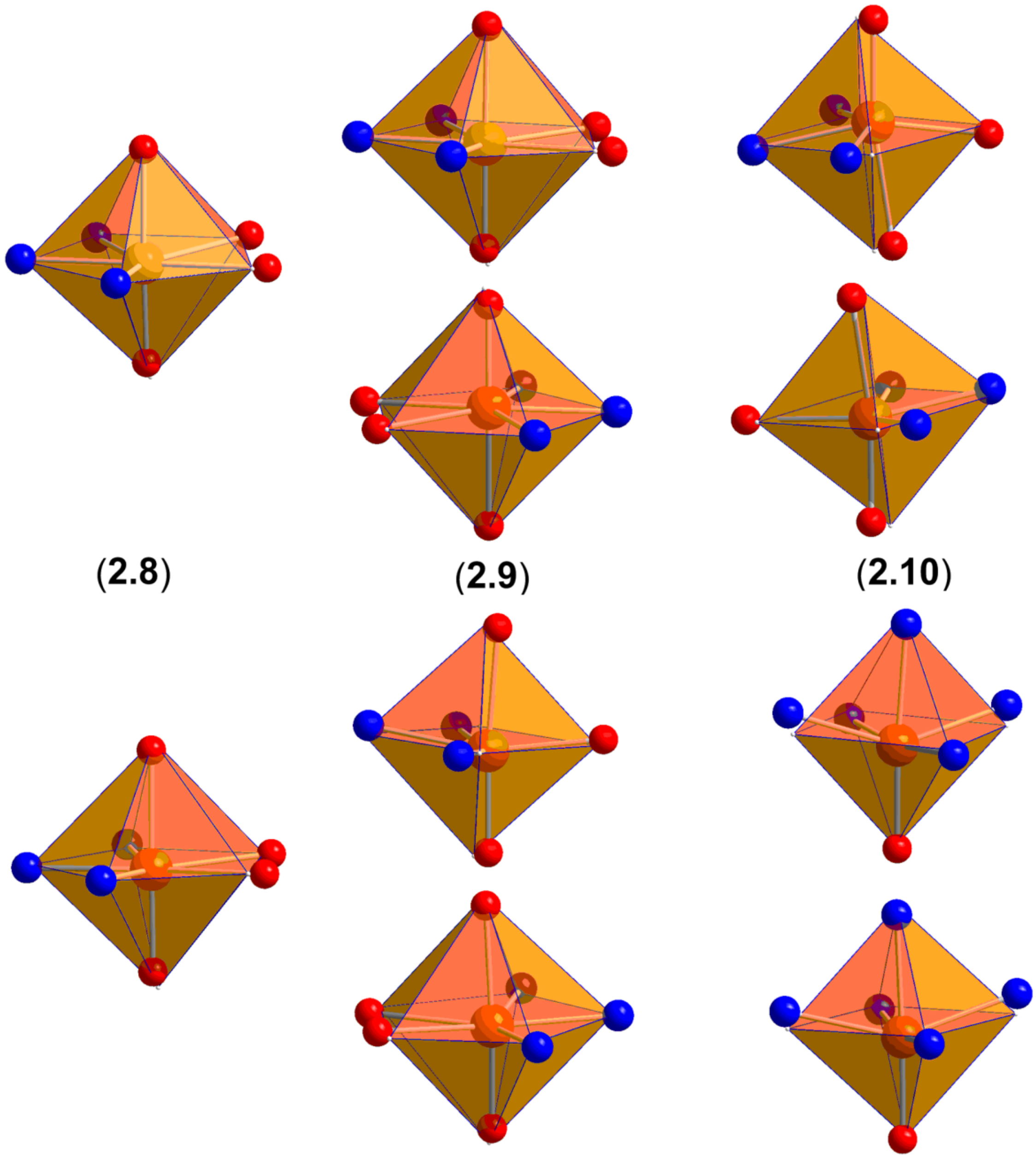

(2.8) (2.9) (2.10)

(2.11) (2.12) (2.13)

Figure 2.11 – Visual depiction of the distortion from ideal octahedral geometry in compounds **2.8-2.13**.

Interestingly, changing the solvent system for dry MeOH does not afford a precipitate when using Py_2F_2BTA, even with prolonged stirring. Instead, the solution must be placed in a diethyl ether bath, which after several days affords $[\{Fe^{III}(NO_3)(Py_2F_2BTA)(MeOH)\}_2(\mu\text{-}O)](NO_3)_2$, (**2.10**) as crystalline brown plates suitable for SCXRD studies (Figure 2.10). In this complex, a molecule of MeOH coordinates in place of water (compared to **2.8**). Similar to **2.8** and **2.9**, complex **2.10** crystallizes in the monoclinic $P2_1/c$ space group with two non-coordinated nitrate counterions found in the crystal lattice. Here, however, the ligated nitrate molecules are bound to the metal centres through only one oxygen, unlike **2.8** and **2.9** which coordinate in a bidentate fashion. As a result, the coordination geometry about the iron ions in **2.10** are best described as distorted octahedra. In the case of complex **2.10**, the molecule sits on a symmetry element leading to crystallographically equivalent iron centres within the dimer, similar to complex **2.8**. To date, efforts to crystallize the pyrimidyl derivative of **2.10** were unsuccessful.

For comparison purposes, we have extended this chemistry to include terpy in place of our BTA ligands in order to isolate terpy analogues of compounds **2.8**–**2.10**. In that regard, we have prepared $[\{Fe^{III}(NO_3)(terpy)(H_2O)\}_2(\mu\text{-}O)](NO_3)_2$ (**2.11**), which is analogous to compound **2.8**, and $[\{Fe^{III}(NO_3)(terpy)(MeOH)\}_2(\mu\text{-}O)](NO_3)_2$ (**2.12**), which can be considered as an intermediate between complexes **2.8** and **2.10**. Compound **2.11** was crystallized directly from an ethanolic solution, and compound **2.12** was obtained from a methanolic solution. Both compounds were immediately filtered after mixing solutions of the ligand and metal salts, then left to sit in a sealed vessel. After a couple days, both **2.11** and **2.12** crystallize as red blocks suitable for SCXRD analysis (Figure 2.12). Upon substitution of the BTA ligand framework to terpy, a change in the crystal system is obtained, with **2.11** and **2.12** crystallizing in the monoclinic $P2_1/n$ and the triclinic $P\bar{1}$ space groups, respectively. The coordination environment in **2.11** is akin to that of complex **2.8**. Compound **2.12**, however, is unique in that the coordination geometry is different between both iron centres due to the denticity of the bound nitrate. One of the metal centres takes the shape of a distorted octahedron, while the other resembles a distorted pentagonal bipyramid. The denticity of the ligated nitrate anions is dictated by the available inter- and intramolecular interactions. Due to the differences in the packing arrangements of the terpy and BTA analogues, it is unsurprising that different coordination geometries are observed about the central metal ion.

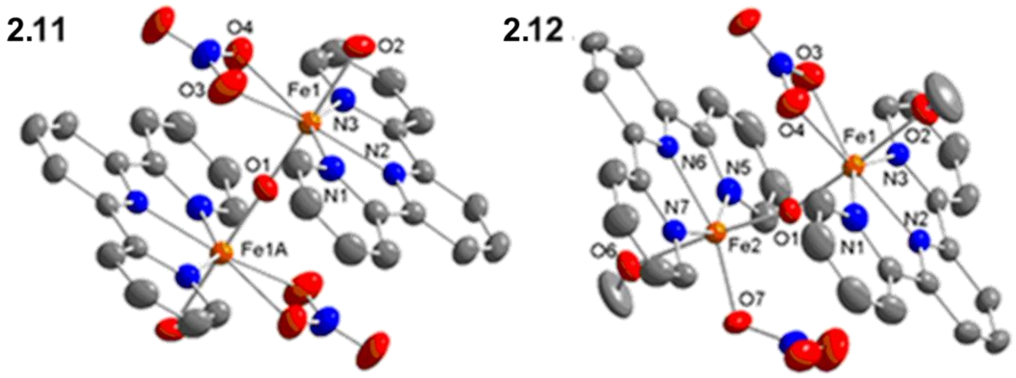

Figure 2.12 – Structural diagram of **2.11** and **2.12** illustrating their molecular units with 50% thermal ellipsoids. Hydrogen atoms and nitrate counterions are omitted for clarity.

By stirring Py_2F_2BTA with $FeCl_3$ in MeCN for thirty minutes, a yellow precipitate can be filtered off. Tuning of the ligand field through substitution of the labile chloride ligands for thiocyanate anions can be performed by dissolving this precipitate in a 2:1 mixture of MeOH and water alongside excess potassium thiocyanate (KSCN). The resulting instant colour change from orange to dark purple upon addition of KSCN in this reaction is indicative of ligand metastasis. Upon placing this solution in a diethyl ether bath, red needles are afforded after a week, which were determined to be $[\{Fe^{III}(NCS)_2(Py_2F_2BTA)\}_2(\mu\text{-}O)]\cdot MeOH$ (**2.13**) through SCXRD methods (Figure 2.13). Crystals of **2.13** belong to the triclinic $P\bar{1}$ space group, with two iron centres being bridged by a single oxygen atom, much like complexes **2.8-2.12**. The coordination environment about each of the metal centres are completed by the coordination of two thiocyanate ligands through their nitrogen atoms, with one MeOH molecule being found in the crystal lattice. Unlike complexes **2.8-2.12** where the BTA ligands are assembled such that they reside in parallel planes, the boratriazine ligands in **2.13** reside in planes perpendicular to one another. This suggests that the replacement of the nitrate ligands for thiocyanates could lead to control over the relative orientation between BTA units in dimeric structures.

2.13

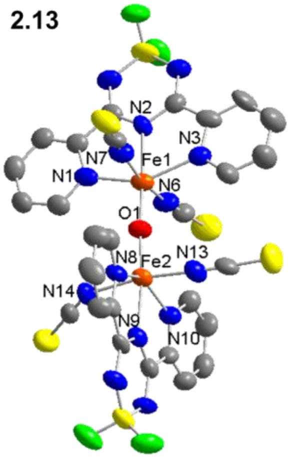

Figure 2.13 – Structural diagram of **2.13** illustrating its asymmetric unit with 50% thermal ellipsoids. Hydrogen atoms and MeOH are omitted for clarity.

In one literature example, ferromagnetic interactions have been shown to be communicated through a single oxygen bridging across two Fe^{III} centres in a dinuclear structure. Specifically, it has been shown that an angle of 146° was important in mediating the observed magnetism.[36] Although the bridging angles obtained in compounds **2.8-2.13** are significantly different to that of the literature example, an examination of the oxo bridging in the obtained compounds is deserved. In **2.8-2.11** and **2.13**, the Fe–O–Fe angle is found to be linear to quasilinear (174.8-180°) in all cases, with **2.12** being the notable exception, featuring a Fe–O–Fe angle of 162.22(10)°. Deviations from linearity can be attributed to differences in the packing arrangement of the compounds in solid state. All complexes having crystallographically equivalent iron centres (**2.8**, and **2.10**-**2.11**) exhibit total linearity about the Fe–O–Fe bonds.

While complexes **2.8-2.13** all pack in layered arrays in the solid state (Figure 2.14), the presence or absence of solvent and counterions in the lattice as well as the relative orientation of the bound ligands all play a role in the observed differences between supramolecular arrangements. Compounds **2.8** and **2.9**, for example, have DMA in the crystal lattice which separates the lamellar arrangements of the metal complexes. This results in the formation of several hydrogen bonds connecting the discrete layers of these structures. The nitrate anions, both bound and unbound, are responsible for the majority of hydrogen bonding in these complexes. In compound **2.8**, these interactions include two O–H···O, two N–H···O, five C–H···O, and one C–H···F intermolecular, along with two C–H···O intramolecular hydrogen bonds within the complex and one C–H···O intramolecular interaction within the solvent. Since compound **2.9** does not feature the same internal symmetry as compound **2.8**, a number of additional unique hydrogen bonds are found within this structure. These include four O–H···O, four N–H···N, six C–H···O and one C–H···F intermolecular, as well as four N–H···O, five C–H···O intramolecular hydrogen bonds within the complex, and three C–H···O intramolecular interaction within the solvent.

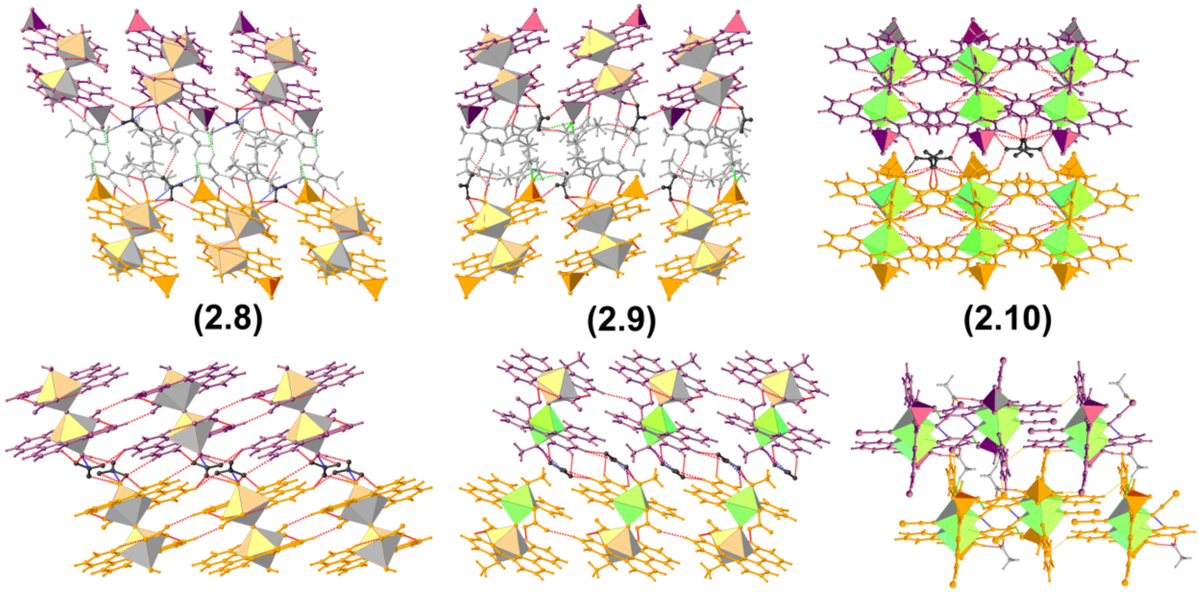

(2.8) (2.9) (2.10)

(2.11) (2.12) (2.13)

Figure 2.14 – Packing diagrams for compounds **2.8-2.13.** Polyhedra are added about the metal centres (lime green octahedra and beige nonahedra) and boron atoms (tetrahedra) to depict molecular orientation. Different layers are colored in alternating schemes; atoms or molecules in the lattice are colored separately. Possible hydrogen interactions include D–H···N (blue), D–H···O (red), D–H···S (yellow) and D–H···F (light green) where D represents the donor atoms, are denoted by dotted lines.

Upon omitting DMA as a crystallization solvent for the synthesis of compound **2.10**, the only non-coordinated species found in the crystal lattice are nitrate anions which localize between layers of the metal complexes. This leads to a reduced interlayer separation between the BTA compounds, which arrange themselves in a continuous head-to-end array as opposed to the alternating head-to-end, end-to-head orientation observed in **2.8** and **2.9**. The disorder about the bound nitrate ion in **2.10** lends to the observation of different hydrogen bonds depending on their orientation. The short contacts in this structure are entirely comprised of hydrogen bonding to different nitrate units, which includes two O–H···O, two N–H···O, and six C–H···O intermolecular hydrogen interactions, and three C–H···O intramolecular short contacts.

Complexes **2.11** and **2.12** host fewer supramolecular interactions than their BTA analogues, complexes **2.8** and **2.10**. This can be attributed to the absence of additional nitrogen and fluorine atoms in the terpy ligand framework. Compound **2.11** crystallizes in a brick-like arrangement, with the unbound nitrate anions being found sandwiched between layers of the metal complex. Interestingly, the ligation of a methanol molecule in place of water in **2.12** leads to the adoption of different coordination geometries about the two iron centres, with the nonacoordinate portions aligning to face one-another. Alike compounds **2.8**-**2.11**, the non-coordinated nitrate counterions in **2.12** are found between layers of the metal complexes. All hydrogen bonds in these structures involve nitrate ions. Two C–H⋯O, one O–H⋯N, and two O–H⋯O intermolecular and two C–H⋯O, one O–H⋯N, and two O–H⋯O intramolecular hydrogen bonds in **2.11**. Compound **2.12** features more contacts, mostly due to increased asymmetry, hosting ten C–H⋯O and one O–H⋯O intermolecular interactions alongside two C–H⋯O and one O–H⋯O intramolecular hydrogen bonds.

Exchanging the use of nitrate ligands for thiocyanate, giving rise to compound **2.13**, not only modifies the topology of the resulting structure, but leads to quite a different packing motif. For example, the solvent molecules are found interspersed within the brick-like arrangement of the metal complexes, as opposed to localizing between the layers. As a result, hydrogen bonding occurs between layers of the compound. Additionally, hydrogen bonding interactions are found to be much more diverse in **2.13**, this includes two intramolecular C—H⋯N interactions and two C–H⋯F, one C–H⋯O, two C–H⋯S, one O–H⋯S, one N–H⋯O, two N–H⋯S, and one N–H⋯F intermolecular hydrogen bonds.

2.3 Synthesis and Structural Analysis of Mononuclear Boratriazine-Based Iron (II) and Cobalt (II) Halide Complexes

In continuation of our investigation into the reactivity and coordination properties of our BTA ligands with first row transition metals, we sought to expand our series of BTA complexes to include transition metals of a lower oxidation state, namely, iron (II) and cobalt (II) compounds. As such, we have prepared and structurally characterized a series structurally related iron (II) and cobalt (II) halide complexes, these being, [$\mathrm{Fe^{II}Cl_2(Py_2F_2BTA)}$] (**2.14**), [$\mathrm{Co^{II}Cl_2(Py_2F_2BTA)}$] (**2.15**), [$\mathrm{Fe^{II}Br_2(Py_2F_2BTA)(MeOH)}$] (**2.16**), and [$\mathrm{Fe^{II}Br_2(Py_2F_2BTA)}$] (**2.17**). Five and six coordinate complexes are common to compounds of both $\mathrm{Fe^{II}}$ and $\mathrm{Co^{II}}$.[40] These metal halide complexes are advantageous for their ability to undergo further reactivity through substitution of the halogen anions for choice ligands (e.g., $\mathrm{CN^-}$, $\mathrm{SCN^-}$, $\mathrm{N_3^-}$, etc.), allowing for the tuning of their ligand field. In this investigation of the ligating properties of our BTA ligands, we have employed chloride and bromide iron salts, under an inert atmosphere, alongside coordinative solvents. As highlighted in Scheme 2.4, by altering the reaction conditions, we were able to isolate a family of mononuclear $\mathrm{Fe^{II}}$ and $\mathrm{Co^{II}}$ complexes.

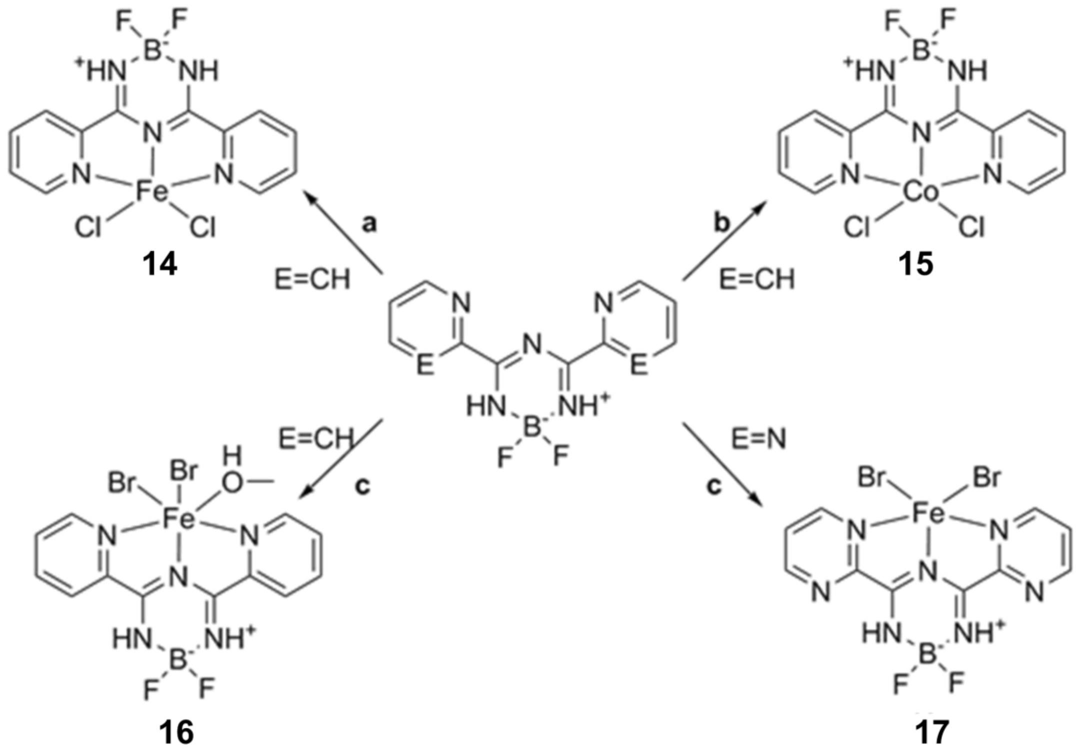

Scheme 2.4 – Synthesis of compounds **2.14-2.17**. Reagents and conditions: (a) $\mathrm{FeCl_2}$, MeCN, MeOH; (b) $\mathrm{CoCl_2}$, MeCN, EtOH; (c) $\mathrm{FeBr_2}$, MeOH.

Upon stirring $FeCl_2$ and Py_2F_2BTA in a 1:1 mixture of MeOH and MeCN under a N_2 atmosphere and dry conditions, a dark green solution is formed. By placing this solution in a diethyl ether bath, crystals of $[Fe^{II}Cl_2(Py_2F_2BTA)]$ (**2.14**, Figure 2.15 and Table 2.5) suitable for SCXRD can be isolated as thin plates that appear orange, or green, depending on the viewing orientation. Crystals of **2.14** belong to the Monoclinic $P2_1/c$ space group. The asymmetric unit of compound **2.14** contains an Fe^{II} central ion coordinated in *mer* fashion to Py_2F_2BTA. The coordination environment about the metal centre is completed by two chloride ions, forming a pentacoordinate environment that is best described as a strongly distorted square pyramid (Table 2.6 and Figure 2.16). The cause of distortion is due in part to the enforced geometry imposed by the ligand, as well as to the chloride anions which are bent out of ideal geometry to accommodate favorable supramolecular interactions.

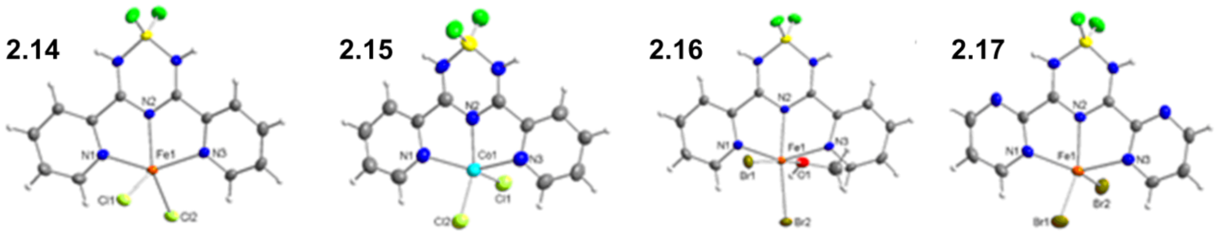

Figure 2.15 – Structural diagram of **2.14-2.17** illustrating their asymmetric units with 50% thermal ellipsoids. Solvent molecules are omitted for clarity.

Table 2.5 – Selected bond distances (Å) in compounds **2.14-2.17**.

	2.14	**2.15**	**2.16**	**2.17**
M1-N1	2.1666(16)	2.166(5)	2.192(2)	2.208(3)
M1-N2	2.1012(15)	2.013(5)	2.139(2)	2.096(3)
M1-N3	2.1913(16)	2.144(5)	2.208(2)	2.202(4)
M1-Cl1	2.3363(6)	2.305(2)		
M1-Cl2	2.2974(5)	2.260(2)		
M1-Br1			2.6069(7)	2.4034(7)
M1-Br2			2.5687(6)	2.4974(8)
M1-O1			2.287(2)	

M corresponds to the central metal ion (Fe in **2.14**, **2.16-2.17**, and Co in **2.15**).

Table 2.6 – Shape analysis of compounds **2.14**-**2.17**. Ideal geometry is a zero value, distortion from this geometry increases the value of the continuous shape measures.

	2.14	**2.15**	**2.16**	**2.17**
PP-5	27.27	29.00		31.68
vOC-5	4.59	4.20		5.38
TBPY-5	4.97	4.18		4.11
SPY-5	2.60	2.27		3.07
JTBPY-5	8.63	7.55		8.28
HP-6			33.93	
PPY-6			23.02	
OC-6			3.66	
TPR-6			12.58	
JPPY-6			26.23	

HP-6: D_{6h}, Hexagon; PPY-6: C_{5v}, Pentagonal pyramid; OC-6: O_h, Octahedron; TPR-6: D_{3h}, Trigonal prism; JPPY-6: C_{5v}, Johnson pentagonal pyramid J_2, PP-5: D_{5h}, Pentagon; vOC-5: C_{4v}, Vacant octahedron (Johnson square pyramid J1); TBPY-5: D_{3h}, Trigonal bipyramid; SPY-5: C_{4v}, Square pyramid; JTBPY-5: D_{3h}, Johnson trigonal bipyramid (J12).

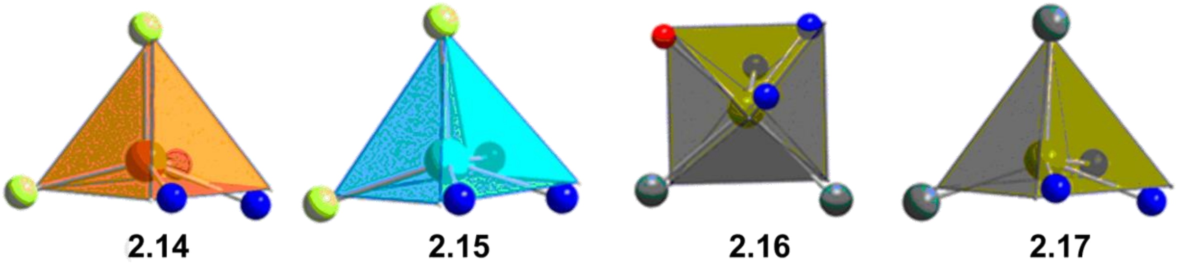

Figure 2.16 – Visual depiction of the distortion from ideal geometry in compounds **2.14**-**2.17**.

Preparation of the cobalt analogue of **2.14** was achieved by stirring $CoCl_2$ and Py_2F_2BTA in a 1:1 mixture of MeCN and EtOH. The resulting green solution was filtered, and after several days, $[Co^{II}Cl_2(Py_2F_2BTA)]$ (**2.15**) was isolated from the mother liquor as thin green plates suitable for SCXRD. Similar to its Fe^{II} analogue, complex **2.15** crystallizes in the monoclinic $P2_1/c$ space group and features a very similar coordination and geometry about the central metal ion, this being a distorted square pyramid. The smaller degree of distortion in the cobalt analogue from square pyramidal can be attributed to the orientation of the chloride anions which can be visualized in Figure 2.16. As expected, due to the smaller size of cobalt, slightly shorter bond lengths are observed to each ligand comparatively to complex **2.14** (Table 2.5).

By stirring Py_2F_2BTA and $FeBr_2$ in MeOH, a dark green solution is obtained which, when placed in a diethyl ether bath, produces dark green blocks of $[Fe^{II}Br_2(Py_2F_2BTA)(MeOH)]$ (**2.16**) suitable for SCXRD analysis. Alike **2.14**, crystals of complex **2.16** belong to the monoclinic $P2_1/c$ space group. The six-coordinate coordination environment about the central Fe^{II} ion in **2.16** constitutes of a BTA ligand bound in *mer* fashion, alongside two bromide anions, yet unlike **2.14**, an axial bound neutral molecule of MeOH is also present in **2.16**. The coordination geometry of **2.16** therefore is best described as a distorted octahedron (Table 2.6 and Figure 2.16). Inclusion of methanol within the coordination sphere likely occurs due to differences in the intramolecular electrostatic interactions offered by bromine coordination, as well as to the formation of favorable intermolecular interactions. In order to lend evidence to the oxidation state of the central metal ion in compound **2.16**, the bond valence sum is provided below, using the bond lengths from the crystal structure in the calculation (Table 2.7). The calculated oxidation states of 1.897 and 2.189, for the assumptions of an Fe^{II} and Fe^{III} metal centre, respectively, are both indicative of a +2 oxidation.

Table 2.7 – Oxidation state determination of **2.16** through the bond valence method.[41,42]

	Bond Valence Sum
Fe^{II}	1.897
Fe^{III}	2.189

Interestingly, using the pyrimidyl BTA ligand under the same reaction and crystallization conditions used to isolate **2.16**, the coordination of MeOH is not observed. This may be due to the lower energy of the LUMO orbitals of Pm_2F_2BTA which stabilizes the complex. When Pm_2F_2BTA is employed using same reaction conditions as **2.16**, dark green blocks suitable for SCXRD analysis are produced, revealing a similar coordination behaviour to **2.14** and **2.15**. Solvent is not coordinated as seen in **2.16**, however, it fills a void within the crystal lattice. Crystals of **2.17** are found to belong to the monoclinic $P2_1/n$ space group. Due to the larger bromine atoms which increase distortion from ideal geometry, the coordination environment about the metal centre in

2.17 can be best described as an intermediate between both square planar and trigonal bipyramidal with the former being the favored geometry.

While compounds **2.14**-**2.17** all tend to pack in the solid state to form layered arrays (Figure 2.17), the nature of the central metal ion, presence of solvent molecules in the lattice, differences in coordination number, and nature of the associated ligands all lead to significant differences in their supramolecular arrangements. For example, although the molecular units between layers of complex **2.14** and **2.15** are both aligned in similar face-to-end orientations, different intramolecular interactions are observed between the Fe^{II} and Co^{II} complexes. In complex **2.14** there is one C–H···Cl, one C–H···F, and three N–H···Cl intermolecular hydrogen bonds, whereas in complex **2.15** there are one C–H···Cl, four C–H···F, and two N–H···Cl intermolecular hydrogen bonds.

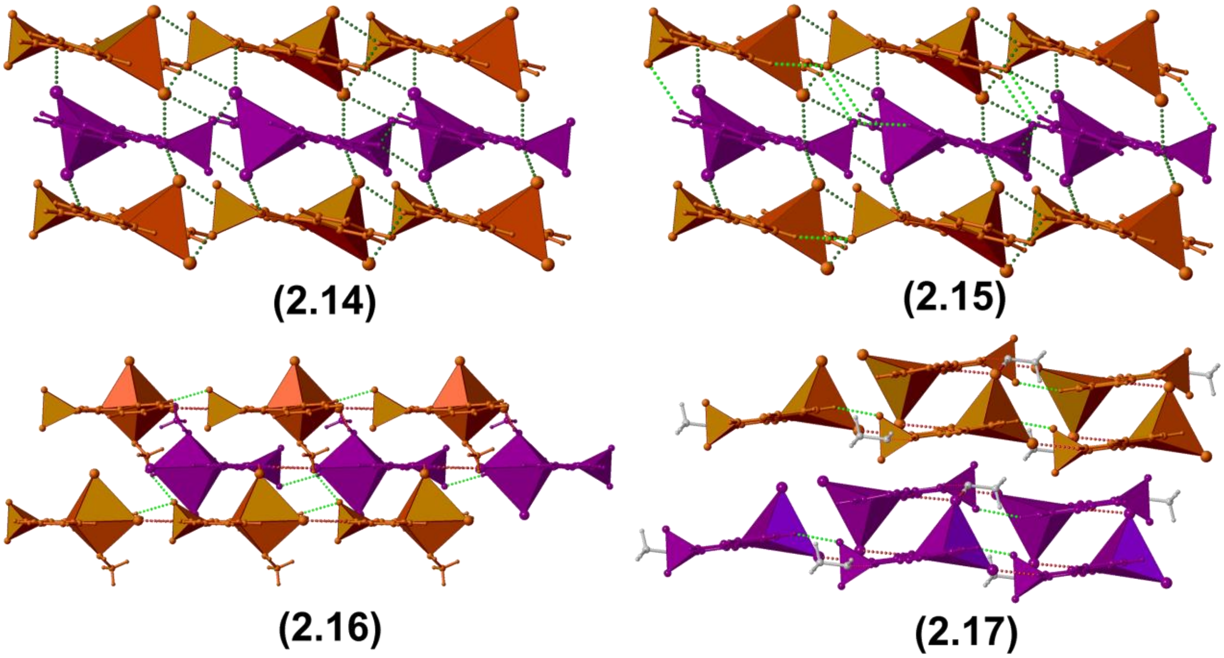
(2.14) **(2.15)** **(2.16)** **(2.17)**

Figure 2.17 – Packing diagrams for compounds **2.14-2.17.** Polyhedra are added about the metal centres (heptahedra for **2.14-2.15** and **2.17**, and octahedra for **2.16**) and boron atoms (tetrahedra) to depict molecular orientation. Different layers are colored in alternating schemes; molecules in the lattice are colored separately. Possible hydrogen interactions D–H···N (blue), D–H···F (light green), D–H···Br (purple), and D–H···Cl (dark green), where D represents the donor atoms, are denoted by dotted lines.

Upon coordination of bromide instead of chloride anions and a neutral molecule of MeOH to the iron centre, the molecular units in complex **2.16** instead pack in a brick-like arrangement between layers. The ligated alcohol in this structure participates in the supramolecular interactions, which include one O–H···Br, two N–H···Br, one C–H···Br, and two C–H···F hydrogen bonds. The Fe^{II} bromide complex of the pyrimidyl ligand (**2.17**), on the other hand, incorporates an uncoordinated molecule of MeOH in the crystal lattice that is interspersed within the layers. This leads to the alternating face-to-end orientation of its molecular units within discrete layers that are two units thick (Figure 2.17). The uncoordinated pyrimidyl nitrogen atoms in this structure participates in two intramolecular N–H···N bonds. The MeOH molecules participate in on O–H···Br and one N–H···O intermolecular bond, and one N–H···Br in addition to one C–H···F intermolecular hydrogen bonds are found between metal complexes.

2.4 Synthesis and Structural Analysis of Cobalt (II/III) Mononuclear Coordination Compounds Bound by Multiple Boratriazine Ligands

In recent years, octahedral Fe^{II} and Co^{II} complexes coordinated through multiple neutral nitrogen ligands have shown promise as useful magnetic materials. More specifically, systems featuring the $[M^{II}(N)_6]^{2+}$ motif have been pursued for their potential spin crossover properties, where M is the metal ion. This type of ligation in Fe^{II} and Co^{II} metal complexes has been shown to impart electron pairing and crystal field splitting energies compatible for crossover between low-spin and high-spin states upon exposure to an external stimuli (e.g., temperature or pressure variance, application of magnetic field, or light irradiation).[43] To achieve this type of coordination, the use of chelating ligands such as terpy-type, and bis-pyrrole based ligands have been employed.[44] Owing to the ability of larger anions (NCS^-,ClO_4^-, BF_4^- , etc) to stabilize metal ions within complexes,[45,46] we sought to pursue *bis*-coordination of our BTA ligands with Fe^{II} and Co^{II}

metal centres using salts featuring large counterions. While this avenue of research is still under investigation, due to time limitations only early results stemming from this research can be presented here. To that end, the preparation of two cobalt complexes displaying differing coordination behaviours were prepared, namely, $[Co^{II}(Py_2F_2BTA)_2][Co^{II}(NCS)_4]\cdot 4DMF$ (**2.18**), and $[Co^{III}(Py_2F_2BTA)_2(CH_3CO_2)]\cdot 1.5MeCN$ (**2.19**).

Upon stirring $Co^{II}(NCS)_2$ and Py_2F_2BTA in dry acetonitrile for thirty minutes, a green solid was isolated through filtration. Upon dissolution in DMF, and placing the resulting dark green solution in a diethyl ether bath, crystals of $[Co^{II}(Py_2F_2BTA)_2][Co^{II}(NCS)_4]\cdot 4DMF$ (**2.18**, Figure 2.18 and Table 2.8) suitable for SCXRD were isolated after a week as green needles. Crystals of **2.18** belong to the orthorhombic *Pbca* space group and consists of one $[Co(Py_2F_2BTA)_2]^{2+}$ cation, one $[Co(NCS)_4]^{2-}$ anion, and four molecules of solvent in the asymmetric unit. The cation features a central six-coordinate Co^{II} ion possessing of a distorted octahedral geometry with two BTA ligands, which are approximately perpendicular to one another and bound in *mer* fashion (Table 2.9 and Figure 2.19). The $[Co(NCS)_4]^{2-}$ structure has a tetrahedral arrangement, with the NCS ligands coordinating through the nitrogen atoms. Close inspection of the Co-N bond lengths reveals an average bond length of 2.13Å (Co1) and 1.95 Å (Co2). As has been observed with previously discussed BTA complexes, the distance between the metal and the nitrogen of the central boratriazine ring is typically on the order of 0.1 Å shorter than that of the peripheral pyridyl nitrogen atoms. As such, the observation of the two shortest C–N bonds (Co1-N1 and Co1-N6) being in the same plane in the *bis*-BTA bound Co^{II} ion cannot be conclusively determined to be caused by a Jahn-Teller distortion of the geometry. The shortest intermetal distance in **2.18** is of 5.875(1) Å, representing the distance between the octahedral and tetrahedral Co^{II} ions. Weak intermolecular ferromagnetic interactions have previously been reported between an octahedral and tetrahedral Co^{II} separated by a distance of 7.05 Å,[46] as such, magnetic coupling is expected to occur between the two Co^{II} species in **2.18**.[22]

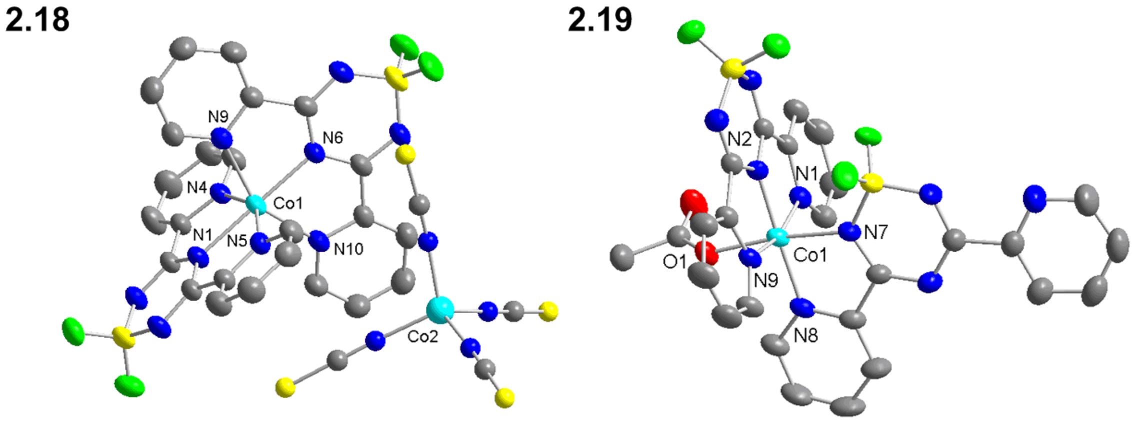

Figure 2.18 – Structural diagram of **2.18-2.19** illustrating their asymmetric units with 50% thermal ellipsoids. Hydrogen atoms and solvent molecules are omitted for clarity.

Table 2.8 – Selected bond distances (Å) in compound **2.18-2.19**.

2.18				**2.19**	
Co1-N1	2.060(3)	Co2-N11	1.959(4)	Co1-N1	1.945(2)
Co1-N4	2.178(3)	Co2-N12	1.946(4)	Co1-N2	1.847(2)
Co1-N5	2.176(3)	Co2-N13	1.957(4)	Co1-N7	1.927(2)
Co1-N6	2.074(3)	Co2-N14	1.940(4)	Co1-N8	1.946(3)
Co1-N9	2.151(3)			Co1-N9	1.955(3)
Co1-N10	2.140(3)			Co1-O1	1.928(2)

Table 2.9 – Shape analysis of compounds **2.18-2.19**. Ideal geometry is a zero value, distortion from this geometry increases the value of the continuous shape measures. Tetrahedral Co^{II} counterion in **2.18** is omitted from this analysis.

	2.18	**2.19**
HP-6	33.17	31.29
PPY-6	20.34	25.77
OC-6	4.45	0.88
TPR-6	10.65	13.20
JPPY-6	24.30	29.33

PPY-6: C_{5v}, Pentagonal pyramid; OC-6: O_h, Octahedron; TPR-6: D_{3h}, Trigonal prism; JPPY-6: C_{5v}, Johnson pentagonal pyramid J_2

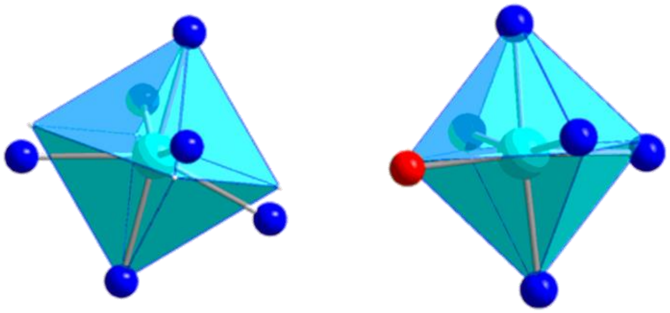
(2.18) (2.19)

Figure 2.19 – Visual depiction of the distortion from ideal octahedral geometry in compounds **2.18** and **2.19**.

Changing the metal salt in the above reaction for $Co^{II}(CH_3CO_2)_2$ affords a yellow solution, which when placed in a diethyl ether bath, yields orange blocks suitable for SCXRD analysis of $[Co^{III}(Py_2F_2BTA)_2(CH_3CO_2)]\cdot 2MeCN$ (**2.19**) after two weeks. This reaction led to oxidation of the metal centre from Co^{II} to Co^{III}, with concomitant reduction of both the BTA ligands to their anionic form. This is evidenced through the deprotonation of a nitrogen atom on each boratriazine ring, as confirmed through SCXRD analysis. The coordination environment in **2.19** therefore involves both an anionic *mer* coordinated and an anionic bidentate bound molecule of the Py_2F_2BTA ligand (Figure 2.18). Completing the coordination sphere is an acetate anion bound through one oxygen. This results in an octahedral geometry with a small distortion due largely to the tridentate bound chelate. One molecule of acetonitrile can be found in the crystal lattice of **2.19** with full occupancy, while another molecule can be found with half occupancy.

2.5 Summary of Findings

Based on the structural analyses, it becomes possible to draw conclusions which may aid in the targeted preparation of new compounds. For example, based on these studies, replacement of a chloride ion in **2.1** for an alcohol ligand (e.g., MeOH and EtOH in **2.2** and **2.3**, respectively) provides evidence that the labile halide anion can be easily replaced with other coordinating ligands. This is further explored in the synthesis of **2.13**, in which complete metastasis of the chloride ligands occurs for thiocyanate anions. Using this methodology, we have garnered the ability to finetune the ligand field around the metal ion while retaining the overall topology and geometry of the system. By taking advantage of these properties, we have used Fe^{II} and Co^{II} halide complexes in the preparation of compounds of magnetic interest. In particular, we prepared Fe^{II} and Co^{II} compounds of Py_2F_2BTA through the use of thiocyanate and azide anions (presented in chapters 3 and 4, respectively). In addition, a coordination trend was identified based on the identity of the boratriazine ligand employed. In the case of Py_2F_2BTA, neutral alcohols were found to ligate to the central metal ion in the right reaction conditions. In all cases, it was found that through the use of the similar methodologies, the Pm_2F_2BTA does to not undergo this type of coordination. This was postulated to be owed to fundamental differences in the frontier orbitals of the ligands employed, in which the pyrimidyl ligand hosts lower energy levels. We also demonstrated methodologies towards accessing oxo bridged dimeric structures using tridentate ligands, which could be useful in the preparation of diverse catalysts and possibly magnetic materials. Lastly, we presented the feasibility for accessing complexes featuring the $[M^{II}(N)_6]$ motif. It is expected that this type of coordination will lead to BTA systems with magnetically interesting features.

2.6 Experimental Procedures

General Procedures

The ligands Py_2F_2BTA and Pm_2F_2BTA were synthesize following previously reported procedures.[27] $Fe(NO_3)_3$ and $FeCl_3$ were obtained from Sigma-Aldrich, $FeBr_3$ was obtained from Oakwood Chemicals, $Co(CH_3CO_2)_2$, $Co(NCS)_2$, $FeBr_2$ and $FeCl_2$ were obtained from Alfa Aesar, KSCN was obtained from VWR, and 2,2’,6’,2”-terpyridine was obtained from Strem chemicals.

All solvents used were of reagent grade, except for dry MeOH and dry MeCN which were of HPLC grade and obtained from Fischer Scientific. Unless otherwise specified, all reactions were performed at room temperature under regular atmosphere. FT-IR spectra in the range 4000-650 cm^{-1} were recorded on an Agilent Cary 630 FT-IR spectrometer.

Synthetic Procedures

Preparation of [Fe^{III}Cl$_3$(Py$_2$F$_2$BTA)]·MeCN (2.1a): A solution of FeCl$_3$ (41 mg, 0.25 mmol) in MeCN (10 mL) was added to a solution of Py$_2$F$_2$BTA (68 mg, 0.25 mmol) in MeCN (10 mL). After stirring 5 minutes, the solution was filtered and capped. After several days, yellow plates are formed, which were isolated, washed with diethyl ether, then left to dry in air. Yield = 96%. IR (neat, cm^{-1}): 3332(*br*), 3290(*br*), 3029(*br*), 1649(*m*), 1604(*m*), 1578(*w*), 1501(*s*), 1464(*s*), 1421(*s*), 1334(*m*), 1297(*s*), 1282(*s*), 1166(*w*), 1115(*m*), 1091(*s*), 1050(*s*), 1025(*m*), 973(*s*), 909(*w*), 813(*m*), 761(*s*), 704(*s*).

Preparation of [Fe^{III}Cl$_3$(Py$_2$F$_2$BTA)]·2DMF (2.1b): To a solution of FeCl$_3$ (41 mg, 0.25 mmol) in MeCN (5 mL) was added a solution of Py$_2$F$_2$BTA (68 mg, 0.25 mmol) in MeCN (5 mL). After stirring 30 minutes, a brown solid was filtered, dissolved in DMF (2 mL), then placed in an diethyl ether bath. After several days, orange needles are formed which were isolated, washed with diethyl ether, then left to dry in air. Yield = 75%. IR (neat, cm^{-1}): 3084(*br*), 3032(*br*), 2939(*br*), 1648(*m*), 1602(*s*), 1498(*s*), 1474(*s*), 1425(*s*), 1400(*s*), 1345(*m*), 1323(*m*), 1283(*s*), 1195(*m*), 1170(*m*), 1145(*m*), 1098(*s*), 1053(*m*), 1016(*s*), 992(*m*), 978(*s*), 868(*m*), 828(*m*), 816(*m*), 807(*m*), 760(*m*), 740(*m*), 714(*s*), 689(*m*).

Preparation of [Fe^{III}Cl$_3$(Py$_2$F$_2$BTA)]·2DMA (2.1c): To a solution of FeCl$_3$ (41 mg, 0.25 mmol) in MeCN (5 mL) was added a solution of Py$_2$F$_2$BTA (68 mg, 0.25 mmol) in MeCN (5 mL). After stirring 30 minutes, a brown solid was filtered, dissolved in DMA (2 mL), then placed in a diethyl ether bath. After several days, orange blocks are formed, which were isolated, washed with diethyl ether, then left to dry in air. Yield = 94%. IR (neat, cm^{-1}): 3049(*m*), 2936(*m*), 1652(*m*), 1616(*s*), 1565(*m*), 1504(*s*), 1468(*s*), 1422(*m*), 1398(*m*), 1341(*m*), 1301(*s*), 1273(*m*), 1191(*m*), 1169(*m*), 1150(*m*), 1093(*s*), 1048(*m*), 1022(*m*), 978(*s*), 924(*m*), 819(*m*), 766(*m*), 742(*m*), 712(*m*), 688(*m*).

Preparation of [Fe^{III}Cl$_2$(Py$_2$F$_2$BTA)(MeOH)]Cl (2.2): A solution of FeCl$_3$ (41 mg, 0.25 mmol) in 1:1 MeOH/MeCN (10 mL) was added to a solution of Py$_2$F$_2$BTA (68 mg, 0.25 mmol) in 1:1 MeOH/MeCN (10 mL). After stirring 5 minutes, the solution was filtered and capped. After several days, yellow plates are formed, which were isolated, washed with diethyl ether then left to dry in air. Yield = 41%. IR (neat, cm^{-1}): 3017.5(*br)*, 2767.4(*w)*, 1650.0(*s)*, 1606.2(*m*), 1501.1(*s*), 1473.8(*s*), 1464.3(*s*), 1432.1(*s*), 1339.1(*s*), 1304.5(*m*), 1294.2(*s*), 1279.2(*m*), 1157.2(*w*), 1124.2(*m*), 1088.3(*s*), 1050.2(*m*), 1026.3(*s*), 1006.1(*s*), 975.4(*s*), 803.9(*m*), 792.0(*m*), 758.3(*s*), 709.3(*s*).

Preparation of [Fe^{III}Cl$_2$(Py$_2$F$_2$BTA)(EtOH)]Cl (2.3): A solution of FeCl$_3$ (41 mg, 0.25 mmol) in 1:1 EtOH/MeCN (10 mL) was added to a solution of Py$_2$F$_2$BTA (68 mg, 0.25 mmol) in 1:1 EtOH/MeCN (10 mL). After stirring 5 minutes, the solution was filtered and capped. After several days, yellow plates are formed, which were isolated, washed with diethyl ether then left to dry in air. Yield = 52%. IR (neat, cm^{-1}): 3013.2(*br*), 2790.2(*w*), 1647.8(*s*), 1607.2(*m*), 1502.7(*s*), 1469.6(*s*), 1432.5(*m*), 1420.9(*m*), 1340.1(*m*), 1296.4(*s*), 1280.1(*m*), 1158.2(*w*), 1123.1(*m*), 1103.2(*m*), 1088.6(*s*), 1051.9(*s*), 1026.9(*s*), 993.1(*m*), 975.4(*s*), 874.9(*m*), 802.1(*m*), 756.9(*s*), 709.9(*s*).

Preparation of [Fe^{III}Cl$_3$(Py$_2$MeO$_2$BTA)] (2.4): A solution of FeCl$_2$ (32 mg, 0.25 mmol) in MeOH (10 mL) was added to a solution of Py$_2$F$_2$BTA (68 mg, 0.25 mmol) in MeOH (10 mL). The resulting green solution was filtered and capped. After a month, crystals growing as orange plates can be isolated, washed with diethyl ether and dried in air. Yield = 35%. IR (neat, cm^{-1}): 3022.6(*br*), 2932.6(*br*), 2905.6(*br*), 2829.4(*w*), 1634.4(*s*), 1603.0(*s*), 1570.5(*w*), 1506.6(*s*), 1466.2(*s*), 1436.2(*s*), 1421.0(*s*), 1335.9(*m*), 1295.9(*s*), 1281.8(*m*), 1196.3(*s*), 1108.9(*s*), 1093.9(*s*), 1057.3(*m*), 1042.5(*m*), 1025.5(*s*), 941.1(*s*), 862.4(*w*), 815.4(*s*), 760.3(*s*), 708.9(*s*).

Preparation of [$Fe^{III}Br_3(Py_2MeO_2BTA)$] (2.5): A solution of $FeBr_2$ (54 mg, 0.25 mmol) in MeOH (10 mL) was added to a solution of Py_2F_2BTA (68 mg, 0.25 mmol) in MeOH (10 mL). The resulting red solution was filtered and capped. After a month, crystals growing as red plates are isolated, washed with diethyl ether and dried in air. Yield = 42%. IR (neat, cm^{-1}): 3088.3(*br*), 3055.9(*br*), 2828.8(*w*), 1637.1(*s*), 1603.4(*m*), 1507.7(*s*), 1465.8(*s*), 1423.5(*s*), 1335.2(*m*), 1297.0(*s*), 1198.0(*s*), 1160.9(*m*), 1093.9(*s*), 1054.9(*m*), 1043.6(*m*), 1023.5(*s*), 941.1(*s*), 814.4(*s*), 757.5(*s*), 707.8(*s*).

Preparation of [$Fe^{III}Cl_3(Pm_2F_2BTA)$] (2.6): A solution of $FeCl_3$ (41 mg, 0.25 mmol) in MeOH (5 mL) was added to a solution of Pm_2F_2BTA (68 mg, 0.25 mmol) in MeCN (5 mL). The resulting orange solution was stirred, filtered and placed in a diethyl ether bath. Orange needles developed overnight. Yield = 72%. IR (neat, cm^{-1}): 3187.5(*br*), 3061.3(*w*), 1664.3(*s*), 1584.7(*s*), 1523.0(*s*), 1444.9(*w*), 1406.8(*s*), 1316.1(*m*), 1279.6(*m*), 1196.7(*w*), 1169.2(*w*), 1119.2(*s*), 1066.0(*m*), 1019.1(*m*), 974.0(*s*), 816.7(*m*), 807.6(*m*), 786.9(*m*), 716.9(*s*), 668.87(*s*).

Preparation of [$Fe^{III}Br_3(Pm_2F_2BTA)$] (2.7): A solution of $FeBr_3$ (50 mg, 0.25 mmol) in MeOH (10 mL) was added to a solution of Pm_2F_2BTA (68 mg, 0.25 mmol) in MeOH (10 mL). The resulting red solution was filtered and capped. After two weeks, crystals growing as red plates are isolated, washed with diethyl ether and dried in air. Yield = 79%. IR (neat, cm^{-1}): 3261(*br*), 3179(*br*), 1660(*m*), 1582(*m*), 1524(*s*), 1444(*w*), 1407(*s*), 1317(*m*), 1280(*m*), 1196(*w*), 1181(*w*), 1144(*m*), 1110(*s*), 1059(*m*), 1016(*m*), 988(*m*), 974(*s*), 841(*w*), 826(*m*), 814(*m*), 799(*m*), 715(*s*), 668(*m*).

Preparation of $[\{Fe^{III}(NO_3)(Py_2F_2BTA)(H_2O)\}_2(\mu\text{–}O)](NO_3)_2\cdot 4DMA$ (2.8): A solution of $Fe(NO_3)_3$ (101 mg, 0.25 mmol) in ethanol (5 mL) was added to a solution of Py_2F_2BTA (68 mg, 0.25 mmol) in ethanol (5 mL). After stirring 2 hours, an orange solid was filtered from the solution, dissolved in DMA (3 mL), then placed in a diethyl ether bath. After a week, orange block-shaped crystals were isolated from solution, then washed with diethyl ether. Yield = 88%. IR (neat, cm^{-1}): 3153(*br*), 3058(*br*), 2936(*br*), 1648(*m*), 1603(*s*), 1499(*s*), 1475(*s*), 1426(*m*), 1397(*s*), 1346(*m*), 1323(*m*), 1284(*s*), 1196(*m*), 1170(*w*), 1145(*w*), 1098(*s*), 1053(*m*), 1042(*w*), 1016(*m*), 992(*m*), 979(*s*), 869(*m*), 828(*m*), 816(*m*), 807(*m*), 760(*s*), 742(*m*), 714(*s*).

Preparation of $[\{Fe^{III}(NO_3)(Py_2F_2BTA)(MeOH)\}_2(\mu\text{–}O)](NO_3)_2$ (2.9): To a dry, N_2 purged Schlenk flask (50 mL) equipped with a filter stick and a second Schlenk flask (50 mL) was added a solution of $Fe(NO_3)_3$ (101 mg, 0.25 mmol) in dry MeOH (10 mL) followed by a solution of Py_2F_2BTA (68 mg, 0.25 mmol) in dry MeOH (10 mL). After stirring 5 minutes, the solution was filtered, then placed in a dry diethyl ether bath. After several days, the compound crystallises as brown plates, which were then isolated from solution and washed with diethyl ether. Yield = 64.2%. IR (neat, cm^{-1}): 3190(*br*), 3073(*br*), 1653(*m*), 1606(*w*), 1506(*s*), 1473(*s*), 1436(*s*), 1311(m), 1281(*s*), 1190(*s*), 1089(*m*), 1051(*m*), 1018(*m*), 976(*s*), 850(*s*), 815(*s*), 757(*s*), 710(*s*).

Preparation of $[\{Fe^{III}(NO_3)(Pm_2F_2BTA)(H_2O)\}_2(\mu\text{–}O)](NO_3)_2$ (2.10): A solution of $Fe(NO_3)_3$ (101 mg, 0.25 mmol) in ethanol (5 mL) was added to a solution of Pm_2F_2BTA (68 mg, 0.25 mmol) in ethanol (5 mL). After stirring 2 hours, a brown solid was filtered from the solution, dissolved in DMA (3 mL), then placed in a diethyl ether bath. After a week, orange block-shaped crystals were isolated from solution, then washed with diethyl ether. Yield = 73%. IR (neat, cm^{-1}): 3276(*br*), 3094(*br*), 1664(*m*), 1625(*w*), 1586(*m*), 1560(*w*), 1523(*s*), 1483(*s*), 1478(*s*), 1444(*m*), 1412(*s*), 1327(*m*), 1279(*s*), 1224(*m*), 1200(*m*), 1135(*m*), 1112(*m*), 1066(*m*), 1015(*m*), 976(*s*), 842(*s*), 827(*s*), 806(*s*), 742(*m*), 720(*s*), 665(*s*).

Preparation of [{$Fe^{III}(NO_3)$(terpy)$(H_2O)\}_2(\mu\text{–}O)](NO_3)_2$ (2.11): A solution of $Fe(NO_3)_3$ (101 mg, 0.25 mmol) in ethanol (10 mL) was added to a solution of terpy (51 mg, 0.25 mmol) in ethanol (10 ml). The solution was immediately filtered and capped. After a couple days, red block-shaped crystals were isolated from solution and washed with diethyl ether. Yield = 72%. IR (neat, cm^{-1}): 3082(*br*), 1599(*w*), 1578(*w*), 1486(*s*), 1466(*m*), 1453(*m*), 1441(*m*), 1400(*m*), 1326(*m*), 1296(*s*), 1241(*m*), 1190(*m*), 1168(*m*), 1136(*w*), 1107(*w*), 1075(*w*), 1059(*w*), 1040(*w*), 1027(*m*), 1015(*m*), 875(*s*), 827(*m*), 810(*w*), 773(*s*), 735(*s*), 663(*m*).

Preparation of [{$Fe^{III}(NO_3)$(terpy)(MeOH)$\}_2(\mu\text{–}O)](NO_3)_2$ (2.12): To a dry, N_2 purged Schlenk flask (50 mL) equipped with a filter stick and a second Schlenk flask (50 mL) was added a solution of $Fe(NO_3)_3$ (101 mg, 0.25 mmol) in dry MeOH (10 mL) followed by a solution of terpy (50.5 mg, 0.25 mmol) in dry MeOH (10 ml). The solution was immediately filtered and capped. After 2 days, red block-shaped crystals were isolated from solution and washed with diethyl ether. Yield = 69%. IR (neat, cm^{-1}): 3086(*br*), 2974(*br*), 1599(*w*), 1578(*w*), 1486(*s*), 1466(*m*), 1453(*m*), 1442(*m*), 1397(*m*), 1327(*m*), 1296(*s*), 1241(*m*), 1190(*m*), 1167(*m*), 1137(*w*), 1107(*w*), 1076(*w*), 1059(*w*), 1050(*w*), 1040(*w*), 1027(*m*), 1015(*s*), 872(*s*), 827(), 809(*w*), 772(*s*), 735(*s*), 684(*w*), 664(*m*).

Preparation of [{$Fe^{III}(NCS)_4(Py_2F_2BTA)\}_2(\mu\text{–}O)$] (2.13): A solution of $FeCl_3$ (41 mg, 0.25 mmol) and Py_2F_2BTA (68 mg, 0.25 mmol) in MeCN (5 mL) was stirred for 30 minutes. Filtration of the solution afforded a yellow powder which was then dissolved in H_2O (5 mL). To this was added a solution of KSCN (100 mg, 1 mmol) in MeOH (10 mL). After stirring 5 minutes, the solution was filtered and placed in a diethyl ether bath. After a week, red needles were then isolated. Yield = 25%. IR (neat, cm^{-1}): 3092(*br*), 2059(*s*), 2050(*s*), 1638(*m*), 1601(*m*), 1567(*w*), 1504(*s*), 1464(*m*), 1435(*m*), 1332(*w*), 1294(*m*), 1277(*m*), 1105(*s*), 1088(*s*), 1047(*s*), 1020(*s*), 965(*s*), 828(*m*), 816(*s*), 786(*m*), 752(*m*), 710(*s*), 663(*m*).

Preparation of [$Fe^{II}Cl_2(Py_2F_2BTA)$] (2.14): Under a N_2 atmosphere, a solution of Py_2F_2BTA (30 mg, 0.12 mmol) in dry MeCN (10 mL) was added to a solution of anhydrous $FeCl_2$ (15 mg, 0.12 mmol) in dry MeOH (5 mL). The resulting green solution was immediately filtered and placed in a diethyl ether bath. After a week, plates which appear green to orange depending on the orientation from which they are observed can be isolated, then washed with dry diethyl ether. Yield = 82%. IR (neat, cm^{-1}): 3236(*br*), 1647(*s*), 1599(*w*), 1570(*w*), 1502(*s*), 1468(*s*), 1430(*m*), 1331(*m*), 1292(*s*), 1274(*m*), 1168(*w*), 1151(*w*), 1111(*m*), 1093(*s*), 1050(*m*), 1011(*w*), 977(*s*), 815(*w*), 755(*s*), 700(*m*), 681(*m*), 669(*w*).

Preparation of [$Co^{II}Cl_2(Py_2F_2BTA)$] (2.15): Under a N_2 atmosphere, a solution of Py_2F_2BTA (60 mg, 0.22 mmol) in dry MeCN (5 mL) was added to a solution of $CoCl_2$ (35 mg, 0.22 mmol) in dry EtOH (5 mL). The resulting green solution was filtered and capped. After a few days, green crystals growing as plates are isolated, washed with diethyl ether and dried in air. Yield = 94%. IR (neat, cm^{-1}): 3228(*br*), 3069(*br*), 1647(*m*), 1597(*w*), 1571(*w*), 1501(*s*), 1466(*m*), 1421(*m*), 1329(*m*), 1292(*s*), 1275(*m*), 1168(*w*), 1151(*w*), 1111(*s*), 1093(*s*), 1049(*m*), 1011(*m*), 995(*m*), 978(*s*), 815(*m*), 755(*s*), 698(*s*).

Preparation of [$Fe^{II}Br_2(Py_2F_2BTA)(MeOH)$] (2.16): Under a N_2 atmosphere, a solution of Py_2F_2BTA (30 mg, 0.12 mmol) in dry MeOH (3 mL) was added to a solution of anhydrous $FeBr_2$ (25 mg, 0.12 mmol) in dry MeOH (5 mL). The resulting green solution was stirred 5 minutes, then filtered and placed in a diethyl ether bath. After several days, dark green blocks are isolated and washed with dry diethyl ether. Yield = 67%. IR (neat, cm^{-1}): 3240(*br*), 3101(*br*), 2764 (*br*), 1645(*m*), 1580(*m*), 1530(*s*), 1476(*w*), 1408(*s*), 1308(*m*), 1260(*w*), 1220 (*m*), 1174(*w*), 1145(*m*), 1101(*m*), 1040(*s*), 1017(*m*), 998(*m*), 970(*s*), 835(*w*), 822(*m*), 810(*m*), 795(*m*), 715(*s*), 665(*m*).

Preparation of [$Fe^{II}Br_2(Pm_2F_2BTA)$]·MeOH (2.17): Under a N_2 atmosphere, a solution of Pm_2F_2BTA (30 mg, 0.12 mmol) in dry MeOH (5 mL) was added to a solution of anhydrous $FeBr_2$ (25 mg, 0.12 mmol) in dry MeOH (5 mL). The resulting green solution was stirred 5 minutes, then filtered and placed in a diethyl ether bath. After several days, dark green blocks are isolated, washed with dry diethyl ether. Yield = 53%. IR (neat, cm^{-1}): 3148 (*br*), 3091(*br*), 1638(*m*), 1581(*m*), 1522(*s*), 1474(*w*), 1448(*s*), 1402(*w*), 1310(*m*), 1280(*m*), 1211 (*w*), 1194(*m*), 1125(*m*), 1100(*m*), 1001(*m*), 980(*w*), 966(*m*), 920(w), 840(*m*), 820(*m*), 810(*w*), 785(*m*), 716(*s*), 660(*m*).

Preparation of [$Co^{II}(Py_2F_2BTA)_2$][$Co^{II}(NCS)_4$]·4DMF (2.18): Under a regular atmosphere, a solution of Py_2F_2BTA (30 mg, 0.12 mmol) in dry MeCN (5 mL) was added to a solution of $Co(NCS)_2$ (22 mg, 0.12 mmol) in dry MeCN (5 mL). The resulting green solution was stirred 30 minutes, and a green solid was filtered, dissolved in DMF (3 mL), then placed in a diethyl ether bath. After two weeks, green needles are isolated, washed with diethyl ether and dried in air. Yield = 21%. IR (neat, cm^{-1}): 2967(*br*), 2927(*br*), 2873(*br*), 2089(*s*), 2045(*s*), 2000(*s*), 1956(*s*), 1645(*s*), 1602(*m*), 1582(*w*), 1508(*s*), 1466(*m*), 1426(*m*), 1379(*w*), 1335(*w*), 1323(*w*), 1298(*s*), 1164(*m*), 1118(*m*), 1086(*s*), 1045(*s*), 1021(*s*), 969(*s*), 893(*m*), 803(*m*), 752(*s*), 714(*s*).

Preparation of [$Co^{III}(Py_2F_2BTA)_2(CH_3CO_2)$]·2MeCN (2.19): Under a regular atmosphere, a solution of Py_2F_2BTA (30 mg, 0.12 mmol) in dry MeCN (5 mL) was added to a solution of $Co(CH_3CO_2)_2$ (32 mg, 0.12 mmol) in dry MeCN (5 mL). The resulting yellow solution was stirred 30 minutes, filtered, then placed in a diethyl ether bath. After two weeks, orange blocks are isolated, washed with diethyl ether and dried in air. Yield = 39%. IR (neat, cm^{-1}): 3094(*br*), 2838(*br*), 1643(*m*), 1604(*m*), 1501(*s*), 1474(*s*), 1426(*m*), 1326(*m*), 1285(*s*), 1206(*m*), 1112(*m*), 1094(*s*), 1053(*m*), 1015(*s*), 968(*s*), 951(*s*), 853(*m*), 815(*s*), 752(*s*), 711(*s*).

2.7 Crystallographic Information

Single Crystal X-Ray Diffraction Procedures

Prior to data collection, crystals were cooled to 200(2) K. Data was collected on a Bruker APEX II CCD detector with a sealed Mo tube source (wavelength 0.71073 Å). Raw data collection and processing were performed with the APEX II and SAINT software packages from BRUKER AXS.[47] The SHELXT and SHELXL programs were used to solve and refine the structures.[48] All non-H atoms were refined anisotropically. The hydrogen atoms of N-H groups were located in a difference Fourier map and refined using bond distance restraints (DFIX in Shelxl), while the remaining hydrogen atoms were placed in idealized positions.

Tables of Crystallographic Data

Table 2.10 – Crystal data and structural refinement for compounds **2.1**-**2.2**.

Crystal data	**2.1a**	**2.1b**	**2.1c**	**2.2**
FW	476.31	581.45	609.50	457.30
Crystal system	Orthorhombic	Triclinic	Monoclinic	Orthorhombic
Space group	$Pbca$	$P\bar{1}$	$P2_1/m$	$Pca2_1$
a, (Å)	14.5646(15)	8.3263(5)	7.3848(17)	14.4383(4)
b, (Å)	13.3330(14)	11.1770(6)	15.240(2)	14.3617(3)
c, (Å)	20.026(2)	14.7673(8)	12.3865(5)	8.8908(2)
α, (°)	90	68.324(1)	90	90
β, (°)	90	86.072(1)	106.813	90
γ, (°)	90	85.857(1)	90	90
V, (Å^3)	3888.9(7)	1272.48 (12)	1334.4(4)	1843.58(8)
Z	8	2	2	4
D_x, (Mg m^{-3})	1.627	1.518	1.517	1.684
μ, (mm^{-1})	1.22	0.95	0.91	1.29
Reflections measured	45674	27820	44150	22906
Independent Reflections	5071	7559	4166	6093
Reflections with $I>2\sigma(I)$	3880	6417	2898	5500
R_{int}	0.051	0.021	0.094	0.029
θ_{max}, θ_{min}, (°)	29.2, 2.0	30.5, 1.5	30.5, 1.7	32.5, 2.0
h	$-19\rightarrow19$	$-11\rightarrow11$	$-10\rightarrow10$	$-19\rightarrow19$
k	$-17\rightarrow18$	$-15\rightarrow15$	$-20\rightarrow21$	$-20\rightarrow21$
l	$-27\rightarrow27$	$-20\rightarrow20$	$-17\rightarrow17$	$-13\rightarrow13$
$R[F^2 > 2\sigma(F^2)]$	0.038	0.032	0.065	0.040
$wR(F^2)$	0.107	0.093	0.15	0.079
$\Delta\rho_{max}$, $\Delta\rho_{min}$ (e Å^{-3})	0.82, -0.47	0.49, -0.40	0.78, -0.80	0.66, -0.40

Table 2.11 – Crystal data and structural refinement for compounds **2.3-2.7**.

Crystal data	**2.3**	**2.4**	**2.5**	**2.6**	**2.7**
FW	481.33	510.34	570.62	459.33	592.71
Crystal system	Orthorhombic	Monoclinic	Triclinic	Orthorhombic	Monoclinic
Space group	$Pca2_1$	$P2_1/c$	$P\bar{1}$	$Pna2_1$	$C2/c$
a, (Å)	14.8084(4)	10.224(5)	9.0128(7)	8.5169(9)	15.3686(13)
b, (Å)	13.9188(3)	24.514(11)	9.7560(7)	16.739(2)	16.9805(13)
c, (Å)	9.1787(3)	8.636(4)	10.3776(8)	13.1900(16)	8.7187(6)
α, (°)	90	90	68.160(2)	90	90
β, (°)	90	104.563(6)	80.758(2)	90	118.672(2)
γ, (°)	90	90	80.101(2)	90	90
V, (Å^3)	1891.87(9)	2094.9(17)	829.71(11)	1880.5(4)	1996.3(3)
Z	4	4	2	4	4
D_x, (Mg m^{-3})	1.690	1.618	2.284	1.622	1.972
μ, (mm^{-1})	1.25	1.14	8.16	1.25	6.78
Reflections measured	8856	21815	16797	29617	30032
Independent Reflections	3397	4889	4626	4516	3320
Reflections with $I>2\sigma(I)$	2397	2677	3852	3104	2093
R_{int}	0.056	0.081	0.030	0.064	0.051
$\theta_{\max}$, $\theta_{\min}$, (°)	27.9, 2.0	28.6, 1.7	30.5, 2.1	28.6, 2.0	31.6, 1.9
h	$-18\rightarrow19$	$-13\rightarrow13$	$-12\rightarrow12$	$-11\rightarrow11$	$-22\rightarrow22$
k	$-17\rightarrow18$	$-32\rightarrow32$	$-13\rightarrow13$	$-22\rightarrow20$	$-24\rightarrow24$
l	$-8\rightarrow11$	$-10\rightarrow11$	$-14\rightarrow14$	$-17\rightarrow17$	$-12\rightarrow12$
$R[F^2 > 2\sigma(F^2)]$	0.0392	0.056	0.026	0.068	0.071
$wR(F^2)$	0.1033	0.176	0.056	0.212	0.236
$\Delta\rho_{\max}$, $\Delta\rho_{\min}$ (e Å^{-3})	0.53, -0.72	0.83, -0.79	0.71, -0.84	0.87, -0.99	1.49, -0.85

Table 2.12 – Crystal data and structural refinement for compounds **2.8-2.10**.

Crystal data	**2.8**	**2.9**	**2.10**
FW	653.19	1310.34	985.94
Crystal system	Monoclinic	Monoclinic	Monoclinic
Space group	$P2_1/c$	$P2_1/c$	$P2_1/c$
a, (Å)	17.0432(5)	18.754(5)	12.0145(7)
b, (Å)	9.2916(3)	9.526(2)	15.1396(8)
c, (Å)	19.5771(6)	31.581(7)	11.1136(7)
α, (°)	90	90	90
β, (°)	111.868(2)	90.280(6)	109.838(3)
γ, (°)	90	90	90
V, (Å^3)	2877.12(16)	5642(2)	1901.54(19)
Z	4	4	2
D_x, (Mg m^{-3})	1.508	1.543	1.722
μ, (mm^{-1})	0.60	0.62	0.87
Reflections measured	54491	149879	17813
Independent Reflections	8946	17075	4966
Reflections with $I>2\sigma(I)$	5938	10840	2520
R_{int}	0.046	0.065	0.058
θ_{max}, θ_{min}, (°)	31.2, 2.1	30.8, 1.7	29.6, 1.8
h	$-24\rightarrow24$	$-27\rightarrow25$	$-12\rightarrow16$
k	$-13\rightarrow13$	$-13\rightarrow13$	$-19\rightarrow20$
l	$-28\rightarrow28$	$-44\rightarrow45$	$-15\rightarrow15$
$R[F^2 > 2\sigma(F^2)]$	0.044	0.042	0.066
$wR(F^2)$	0.130	0.108	0.158
$\Delta\rho_{max}$, $\Delta\rho_{min}$ (e Å^{-3})	0.46, -0.34	0.43, -0.33	0.76, -0.33

Table 2.13 – Crystal data and structural refinement for compounds **2.11-2.13**.

Crystal data	**2.11**	**2.12**	**2.13**
FW	878.31	906.36	938.18
Crystal System	Monoclinic	Triclinic	Triclinic
Space group	$P2_1/n$	$P\bar{1}$	$P\bar{1}$
a, (Å)	10.1216(4)	8.691(2)	8.869(2)
b (Å)	9.8510(4)	9.839(3)	13.967(4)
c (Å)	17.6542(7)	21.839(6)	16.059(4)
α, (°)	90	99.566(4)	91.772(9)
β, (°)	98.576(1)	94.195(4)	92.064(8)
γ, (°)	90	92.438(4)	100.028(8)
V, (Å^3)	1740.58(12)	1833.7(9)	1956.3(9)
Z	2	2	2
D_x, (Mg m^{-3})	1.676	1.642	1.593
μ, (mm^{-1})	0.92	0.88	1.02
Reflections measured	26291	23344	16924
Independent Reflections	4913	9179	6154
Reflections with $I>2\sigma(I)$	3673	6613	2522
R_{int}	0.031	0.034	0.107
θ_{max}, θ_{min}, (°)	30.3, 2.2	29.2, 1.9	24.1, 1.5
h	$-14\rightarrow14$	$-11\rightarrow11$	$-10\rightarrow9$
k	$-13\rightarrow13$	$-13\rightarrow13$	$-13\rightarrow16$
l	$-20\rightarrow25$	$-29\rightarrow29$	$-18\rightarrow18$
$R[F^2 > 2\sigma(F^2)]$	0.033	0.046	0.066
$wR(F^2)$	0.090	0.113	0.205
$\Delta\rho_{max}$, $\Delta\rho_{min}$ (e Å^{-3})	0.44, -0.34	0.75, -0.24	0.95, -0.44

Table 2.14 – Crystal data and structural refinement for compounds **2.14-2.17**.

Crystal data	**2.14**	**2.15**	**2.16**	**2.17**
FW	200.05	402.89	520.77	521.75
Crystal system	Monoclinic	Monoclinic	Monoclinic	Monoclinic
Space group	$P2_1/c$	$P2_1/\mathrm{c}$	$P2_1/c$	$P2_1/n$
a, (Å)	7.5471(2)	7.587(5)	9.7528(17)	6.8385(3)
b, (Å)	12.4760(3)	12.433(8)	13.216(2)	14.2493(5)
c, (Å)	15.7679(4)	15.533(10)	13.904(2)	17.7146(6)
α, (°)	90	90	90	90
β, (°)	98.739(1)	98.815(9)	107.323(1)	98.846(2)
γ, (°)	90	90	90	90
V, (Å^3)	1467.43(6)	1447.9(16)	1710.9(5)	1705.65
Z	8	4	4	4
D_x, (Mg m^{-3})	1.811	1.848	2.022	2.032
μ, (mm^{-1})	1.42	1.58	5.59	5.61
Reflections measured	49273	14017	22514	9746
Independent Reflections	3385	2615	3722	4384
Reflections with $I>2\sigma(I)$	3296	1591	3029	3066
R_{int}	0.024	0.146	0.052	0.029
θ_{max}, θ_{min}, (°)	27.6, 2.1	25.2, 2.7	27, 2.2	30.2, 1.8
h	-9→9	-9→9	-12→12	-4→9
k	-16→16	-14→14	-16→16	-19→15
l	-20→20	-18→18	-17→17	-23→23
$R[F^2 > 2\sigma(F^2)]$	0.028	0.064	0.028	0.048
$wR(F^2)$	0.072	0.174	0.069	0.118
$\Delta\rho_{max}$, $\Delta\rho_{min}$ (e Å^{-3})	0.56, -0.23	0.99, -0.70	0.54, -0.60	1.02, -1.35

Table 2.15 – Crystal data and structural refinement for compounds **2.18-2.19**.

Crystal data	2.18	2.19
FW	1188.68	1447.31
Crystal system	Orthorhombic	Monoclinic
Space group	*Pbca*	*Cc*
a, (Å)	19.232(3)	25.4787(10)
b (Å)	18.245(3)	14.0027(5)
c (Å)	30.868(5)	10.1044(5)
α , (°)	90	90
β , (°)	90	102.780(1)
γ , (°)	90	90
V, (Å^3)	10831(3)	3515.6(2)
Z	8	2
D_x, (Mg m^{-3})	1.458	1.67
μ, (mm^{-1})	0.84	0.55
Reflections measured	95498	25906
Independent Reflections	9795	8762
Reflections with $I>2\sigma(I)$	5830	7475
R_{int}	0.093	0.027
θ_{max}, θ_{min}, (°)	25.3, 1.3	28.5, 2.5
h	$-23\rightarrow22$	$-34\rightarrow34$
k	$-21\rightarrow21$	$-18\rightarrow18$
l	$-37\rightarrow37$	$-13\rightarrow13$
$R[F^2 > 2\sigma(F^2)]$	0.041	0.035
$wR(F^2)$	0.128	0.083
$\Delta\rho_{max}$, $\Delta\rho_{min}$ (e Å^{-3})	0.47, -0.43	0.52, -0.20

Powder Crystal X-Ray Diffraction (PXRD) Procedures

Bulk purity of the complexes described here was obtained on a Rigaku Ultima IV diffractometer and assessed by comparison of the obtained PXRD patterns with predicted patterns from single crystal data. The experimental PXRD patterns reported herein are found to convincingly match the predicted patterns.

Overlay of Experimental PXRD and Predicted (through Mercury) SCXRD Patterns

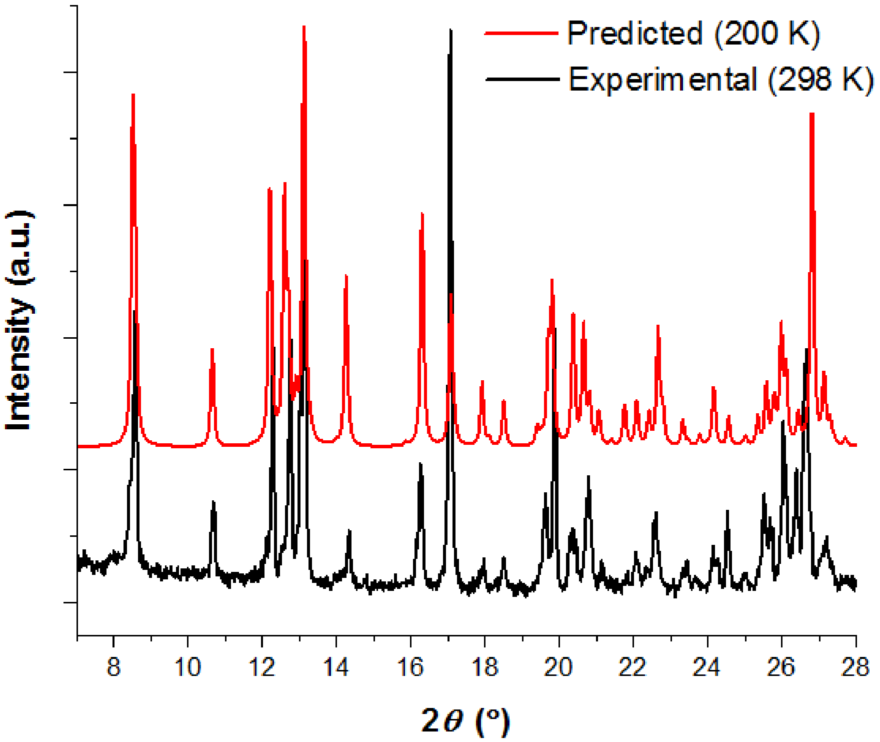

Figure 2.20 – PXRD pattern overlay of experimental microcrystalline sample of **2.1b** with the predicted pattern.

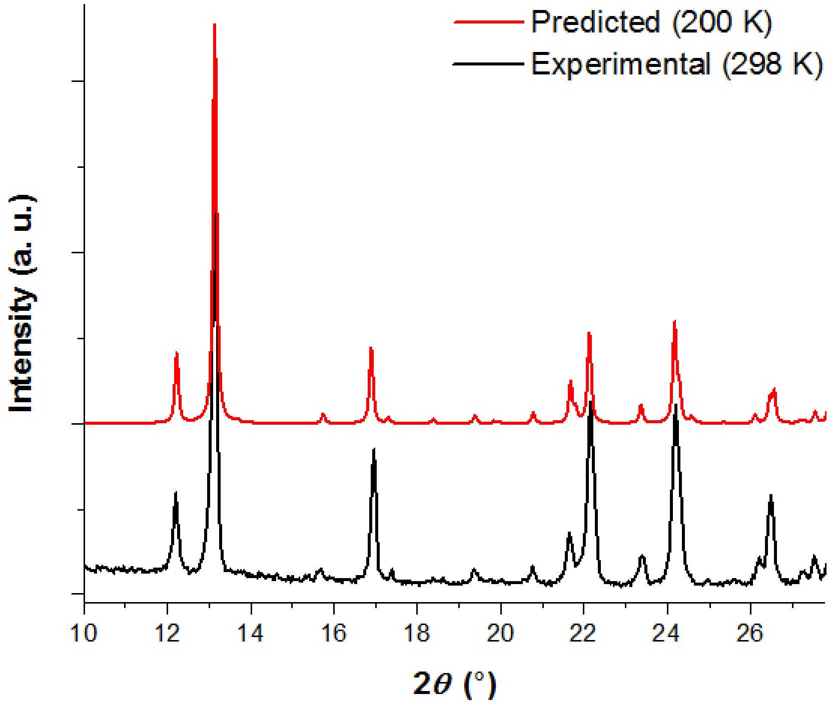

Figure 2.21 – PXRD pattern overlay of experimental microcrystalline sample of **2.2** with the predicted pattern.

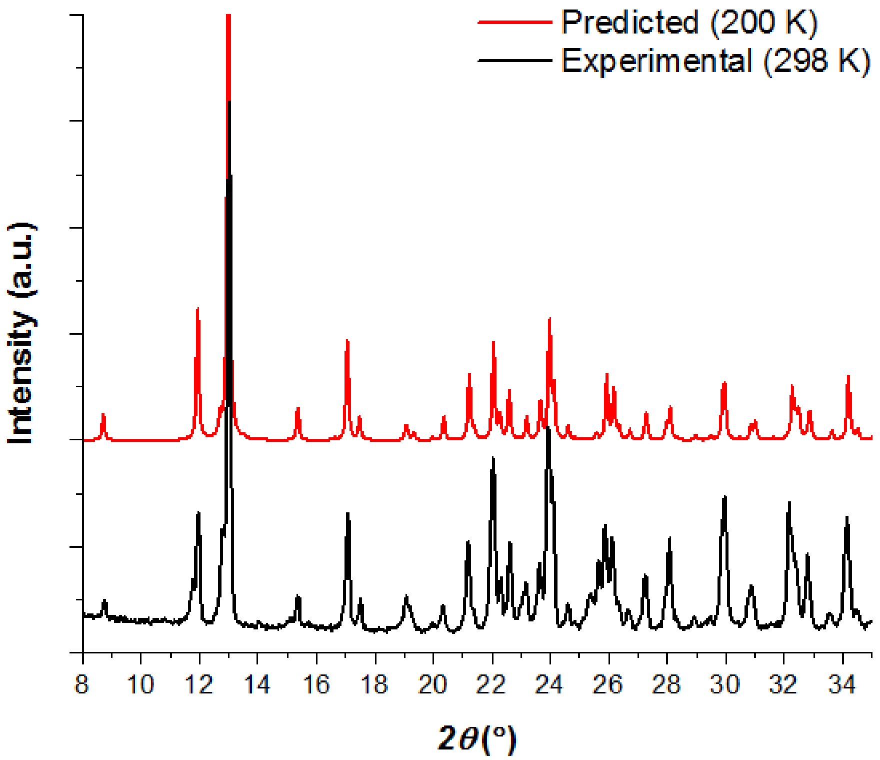

Figure 2.22 – PXRD pattern overlay of experimental microcrystalline sample of **2.3** with the predicted pattern.

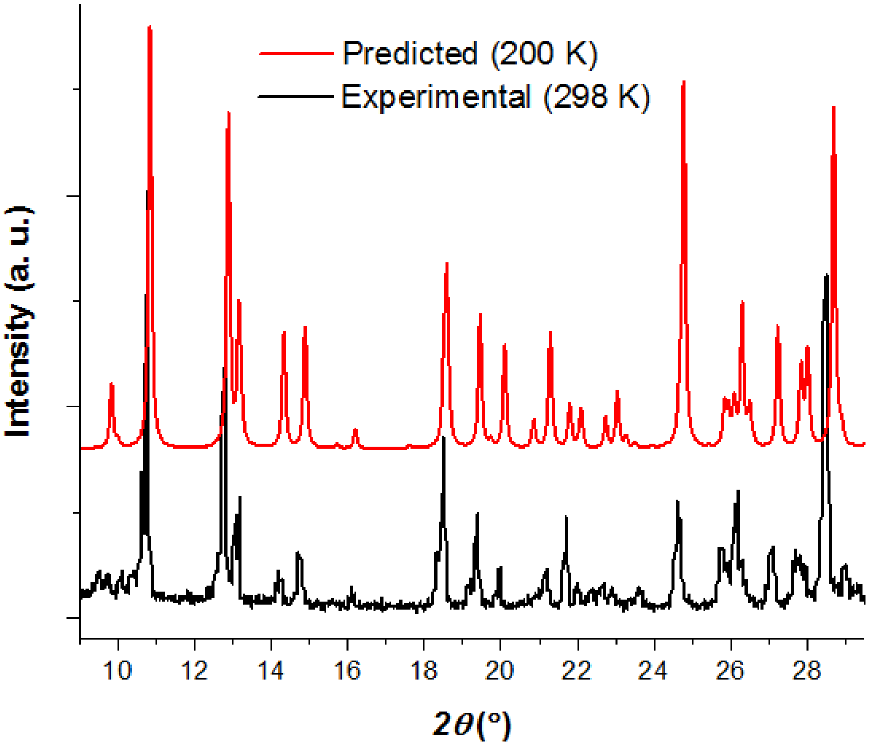

Figure 2.23 – PXRD pattern overlay of experimental microcrystalline sample of **2.5** with the predicted pattern.

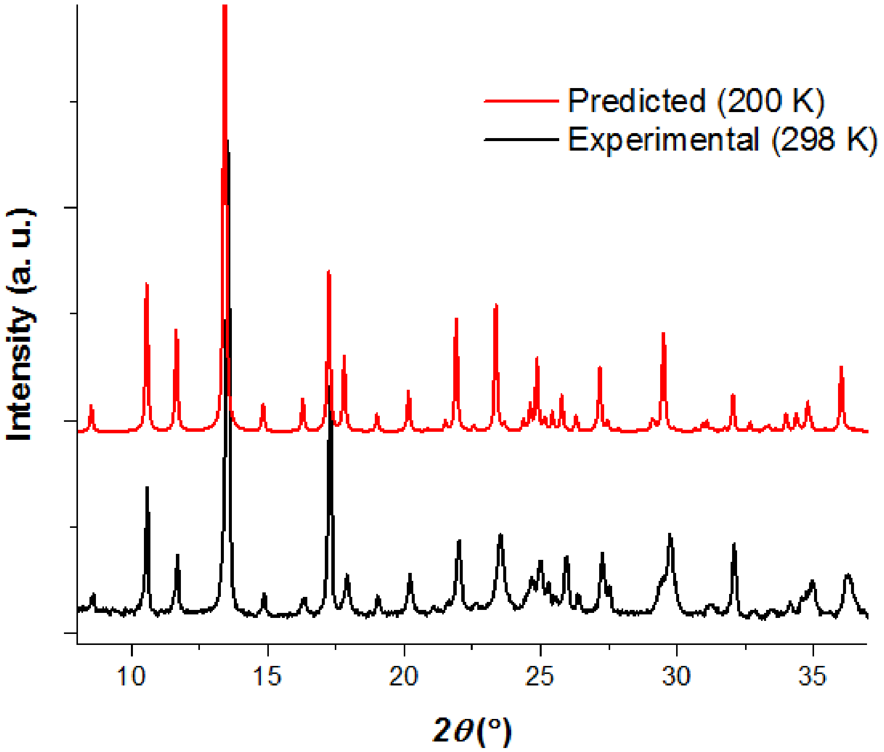

Figure 2.24 – PXRD pattern overlay of experimental microcrystalline sample of **2.6** with the predicted pattern.

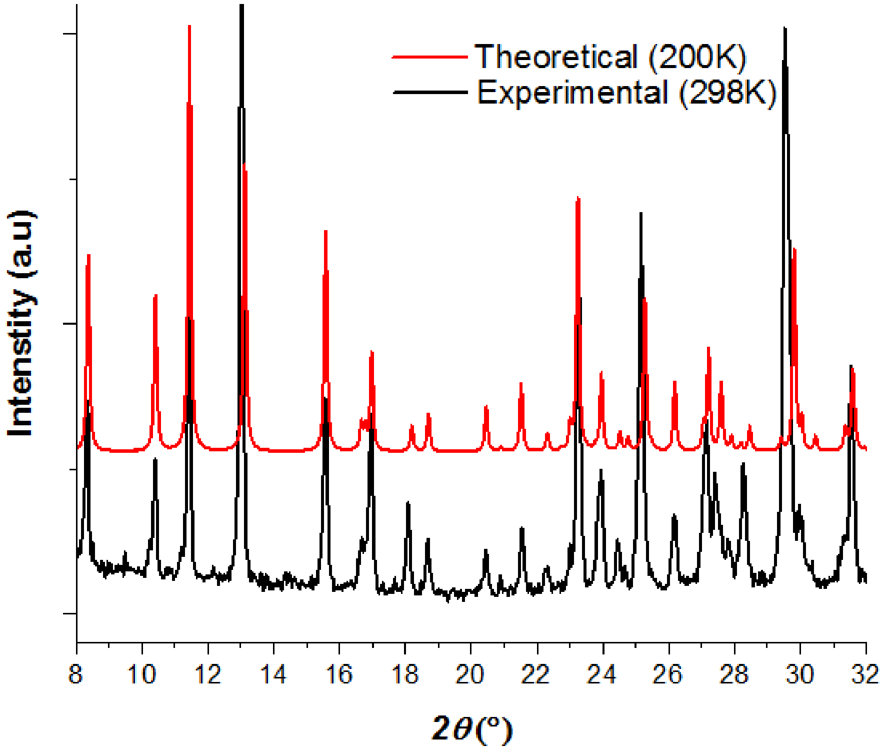

Figure 2.25 – PXRD pattern overlay of experimental microcrystalline sample of **2.7** with the predicted pattern.

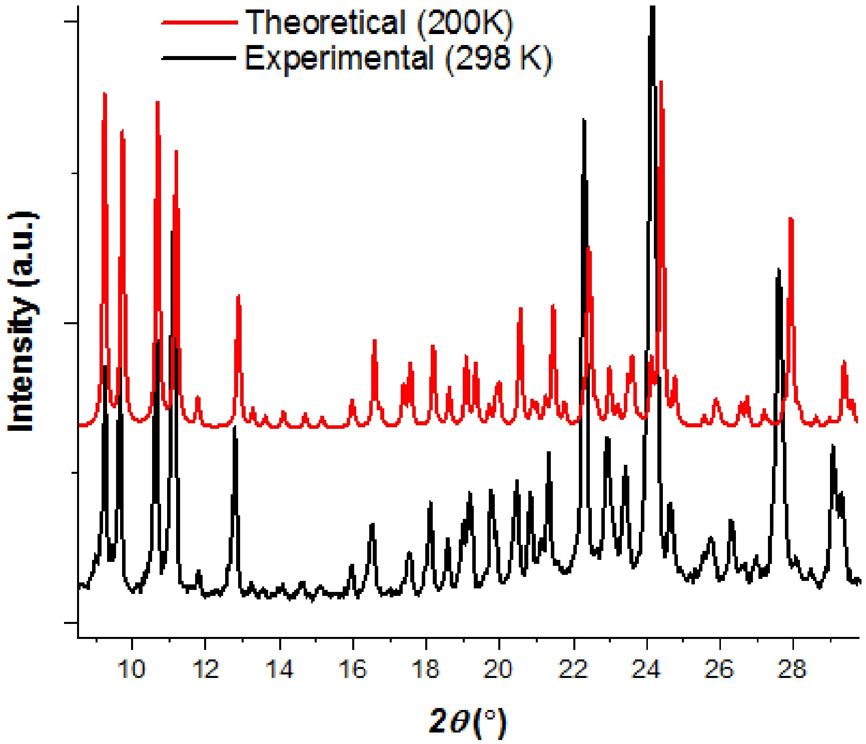

Figure 2.26 – PXRD pattern overlay of experimental microcrystalline sample of **2.8** with the predicted pattern.

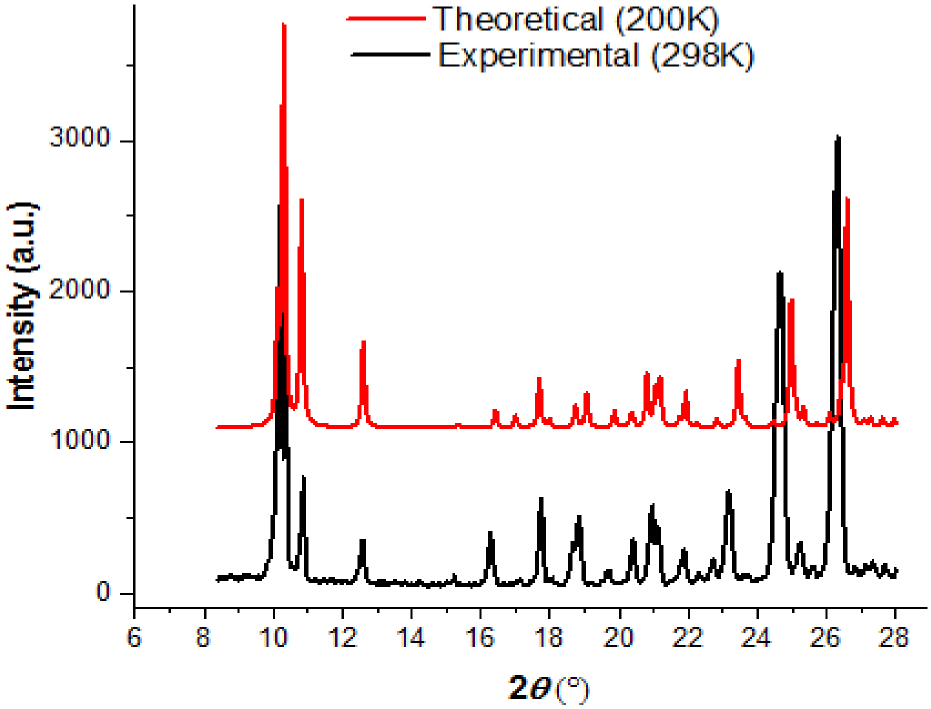

Figure 2.27 – PXRD pattern overlay of experimental microcrystalline sample of **2.11** with the predicted pattern.

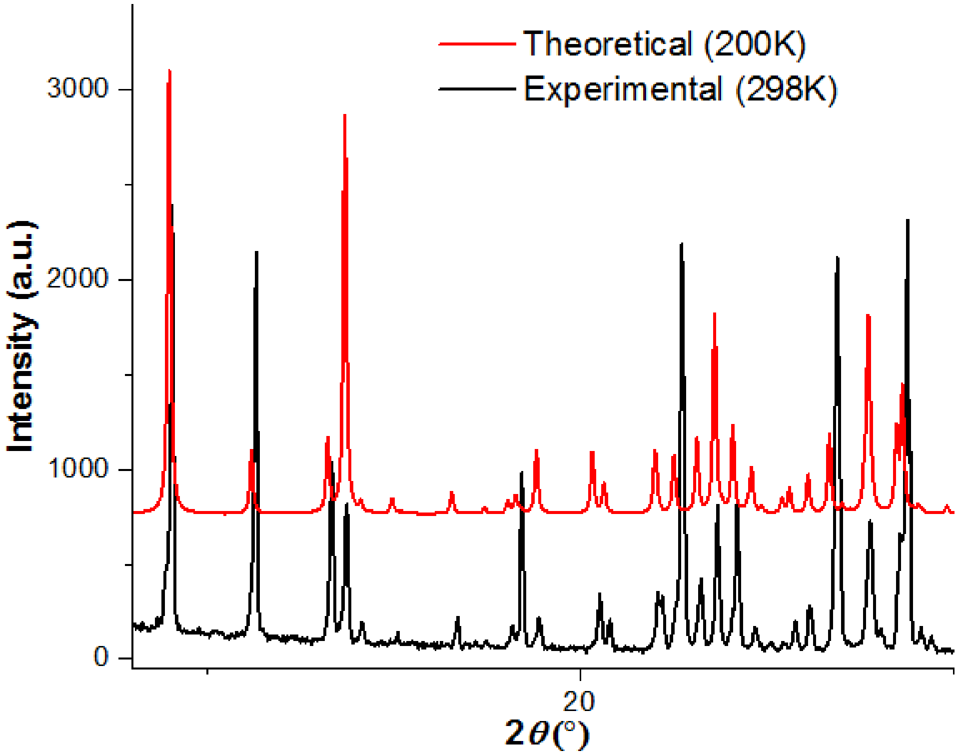

Figure 2.28 – PXRD pattern overlay of experimental microcrystalline sample of **2.14** with the predicted pattern.

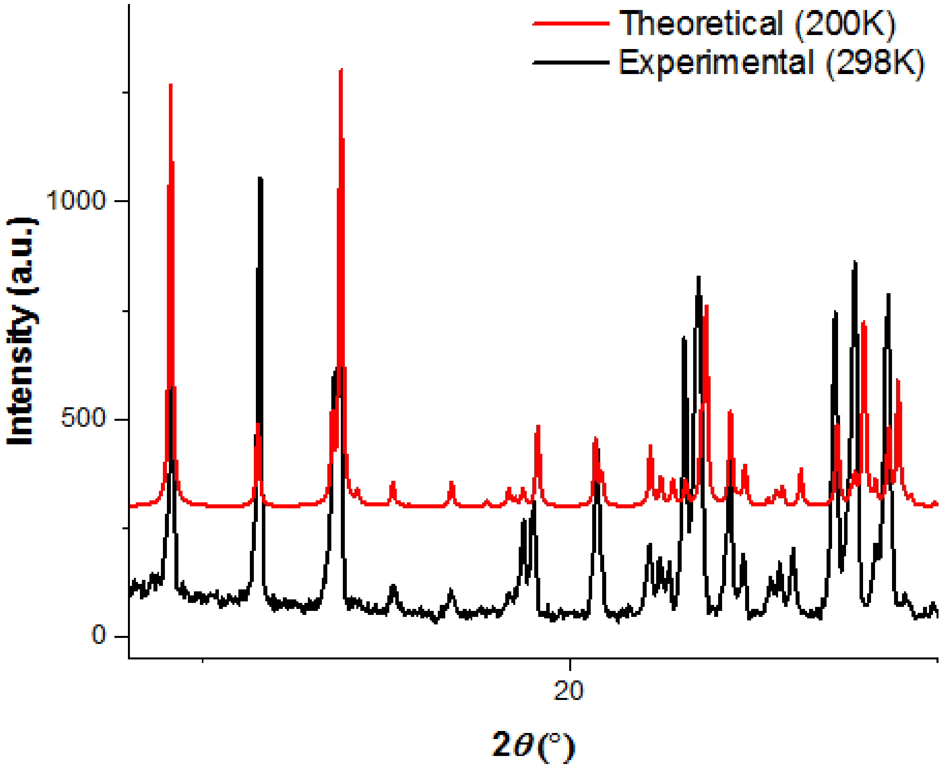

Figure 2.29 – PXRD pattern overlay of experimental microcrystalline sample of **2.15** with the predicted pattern.

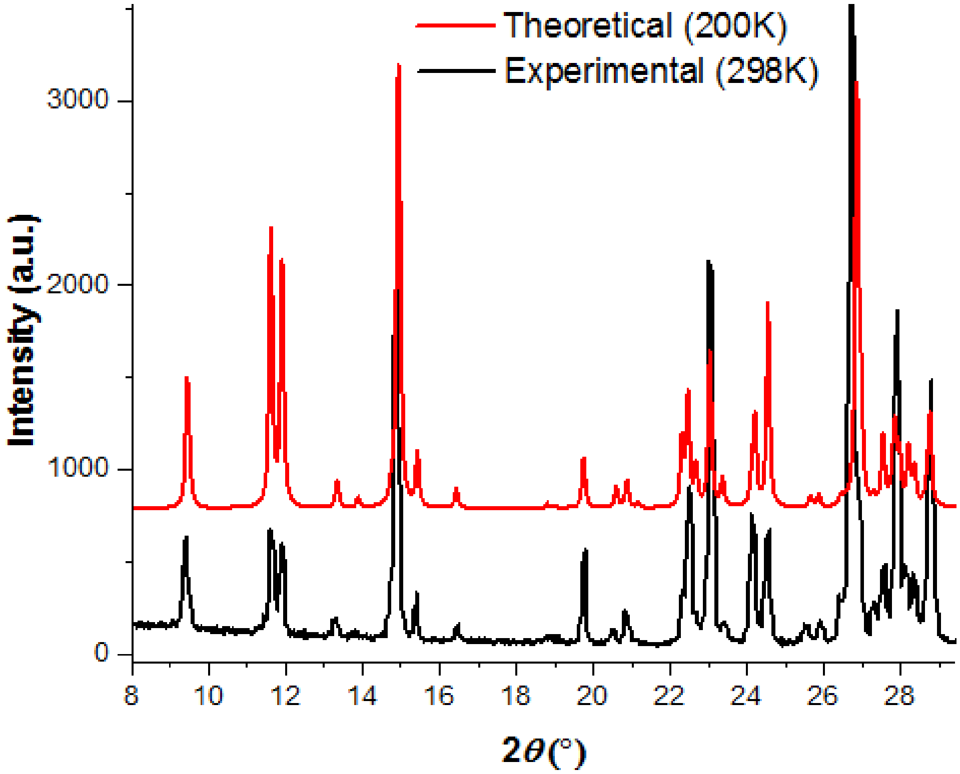

Figure 2.30 – PXRD pattern overlay of experimental microcrystalline sample of **2.17** with the predicted pattern.

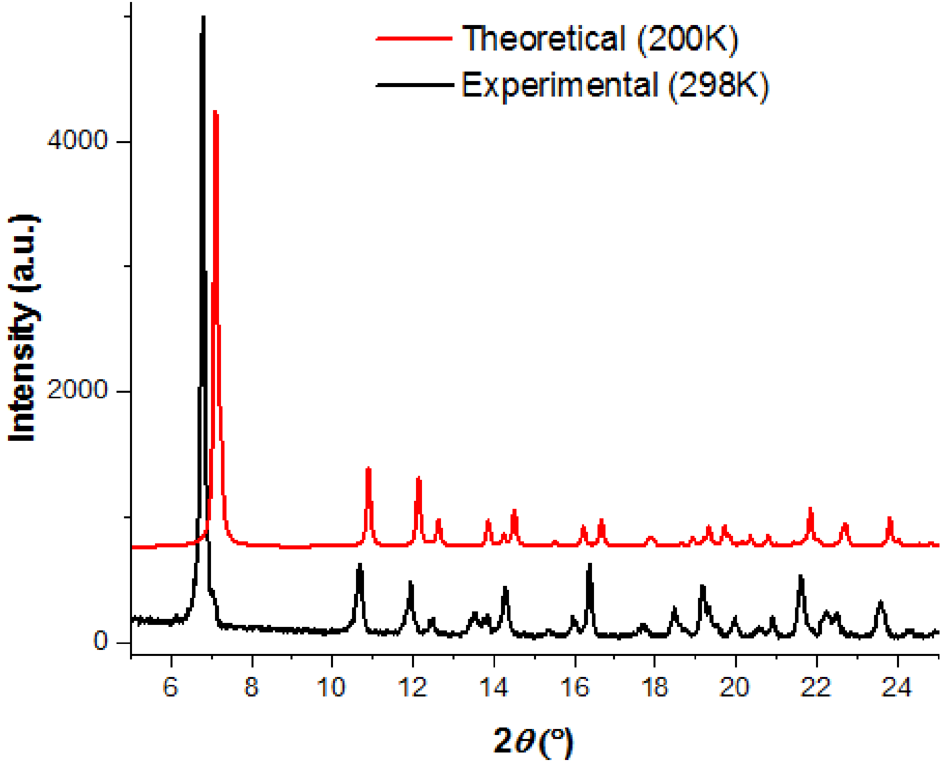

Figure 2.31 – PXRD pattern overlay of experimental microcrystalline sample of **2.19** with the predicted pattern.

2.8 Supramolecular Interactions

Table 2.16 – Hydrogen-bonding in **2.1a** (Å, °)

D—H···*A*	*D*—H	H···*A*	*D*···*A*	*D*—H···*A*
N4–H4A···Cl2^{i}	0.79(3)	2.73(3)	3.438(2)	151(2)
N5–H5A···Cl3^{ii}	0.82(3)	2.59(3)	3.3976(19)	171(2)
C1–H1···Cl1	0.95(3)	2.83(3)	3.479(3)	127(2)
C2–H2···Cl2^{iii}	0.94(3)	2.76(3)	3.478(3)	135(2)
C1S–H1S3···Cl2	0.98	2.77	3.565(4)	138
C4–H4···Cl2^{i}	0.97(3)	2.71(3)	3.665(3)	169(2)
C9–H9···Cl3^{ii}	1.03(3)	2.59(3)	3.602(2)	167.5(18)
C10–H10···Cl3^{iv}	0.92(3)	2.76(3)	3.458(2)	133(2)
C11–H11···Cl1^{v}	0.95(3)	2.70(3)	3.636(2)	169(2)
C12–H12···F1^{vi}	0.96(2)	2.40(2)	2.997(3)	120.0(16)

Symmetry codes: (i) 1/2-x,1/2+y,z; (ii) -1/2+x,1/2-y,1-z; (iii) 1-x,1/2+y,3/2-z; (iv) 1/2-x,-1/2+y,z; (v) 1-x,-y,1-z; (vi) 1/2+x,1/2-y,1-z.

Table 2.17 – Hydrogen-bonding in **2.1b** (Å, °)

D—H···*A*	*D*—H	H···*A*	*D*···*A*	*D*—H···*A*
C1S–H1B···F2^{i}	0.98	2.39	3.347(2)	164.4
C2S–H2A···O1S^{i}	0.98	2.63	3.325(3)	127.8
C2S–H2B···Cl1^{ii}	0.98	2.72	3.681(2)	168.4
C3S–H3A···Cl3^{iii}	0.95	2.97	3.9024(19)	168.6
C4–H4···F1^{iv}	0.95	2.62	3.2191(17)	121.7
C4–H4···O1S	0.95	2.39	3.273(2)	154.7
C4S–H4D···F1	0.98	2.58	3.511(3)	159.4
C4S–H4B···Cl1^{v}	0.98	2.81	3.713(2)	154.0
C4S–H4C···Cl2^{vi}	0.98	2.93	3.863(3)	159.0
C6S–H6A···Cl2^{vii}	0.95	2.78	3.5179(17)	135.2
C9–H9···O2S	0.95	2.43	3.3327(19)	159.6
C12–H12···Cl1	0.95	2.99	3.5782(16)	121.8
N4–H4A···O1S	0.81(3)	1.98(3)	2.7688(16)	166(3)
N5–H5A···O2S	0.85(3)	1.91(3)	2.7434(17)	166(3)

Symmetry codes: (i) -x+2,-y,-z+1; (ii) -x+1,-y+1,-z+1; (iii) x+1,y,z; (iv) -x+1,-y,-z+1; (v) x+1,y-1,z; (vi) x,y-1,z; (vii) -x+1,-y+1,-z.

Table 2.18 – Hydrogen-bonding in **2.1c** (Å, °)

D—H⋯*A*	*D*—H	H⋯*A*	*D*⋯*A*	*D*—H⋯*A*
N3–H3A⋯O1^{i}	0.86(3)	1.93(4)	2.776(14)	168(4)
N3–H3A⋯O2^{i}	0.86(3)	2.12(4)	2.898(10)	150(5)
N3–H3A⋯O3^{i}	0.86(3)	1.91(6)	2.76(4)	172(5)
C2–H2⋯Cl3^{ii}	0.95	2.69	3.449(3)	137
C4–H4⋯O1^{i}	0.95	2.36	3.255(13)	157
C4–H4⋯O2^{i}	0.95	2.35	3.219(11)	153
C4–H4⋯O3^{i}	0.95	2.31	3.22(4)	161
C7–H7A⋯F2^{iii}	0.98	2.54	3.46(2)	156
C7–H7C⋯O1	0.98	2.27	2.695(19)	105
C8–H8B⋯F1^{iv}	0.98	2.46	3.18(2)	130
C10–H10B⋯F2^{v}	0.98	2.39	3.361(18)	169

Symmetry codes: (i) x,y,-1+z; (ii) 2-x,-1/2+y,1-z; (iii) 1-x,-1/2+y,1-z; (iv) -x,-1/2+y,1-z; (v) x,y,1+z.

Table 2.19 – Hydrogen-bonding in **2.2** (Å, °)

D—H⋯A	D—H	H⋯A	D⋯A	D—H⋯A
O1—H1⋯Cl1^{i}	0.83(5)	2.17(5)	2.987(3)	167(6)
N5—H5⋯Cl3^{ii}	0.82(3)	2.46(3)	3.265(3)	169(4)
N4—H4⋯Cl3^{iii}	0.81(4)	2.54(4)	3.299(3)	158(5)
C9—H9⋯Cl3^{ii}	0.94	2.62	3.549(4)	164
C3—H3⋯F1^{iv}	0.94	2.52	3.002(4)	112
C13—H13c⋯Cl1	0.97	2.83	3.344(6)	114

Symmetry codes: (i) x,y,z; (ii) 1/2-x,y,1/2+z; (iii) 1-x,1-y,1/2+z; (iv) 1/2+x,1-y,z.

Table 2.20 – Hydrogen-bonding in **2.3** (Å, °)

D—H⋯*A*	*D*—H	H⋯*A*	*D*⋯*A*	*D*—H⋯*A*
C1—H1⋯Cl1	0.95	2.98	3.569(7)	121
C1—H1⋯Cl2^{i}	0.95	2.94	3.661(7)	134
C4—H4⋯Cl3^{ii}	0.95	2.76	3.687(8)	164
C9—H9⋯Cl3^{iii}	0.95	2.63	3.549(7)	164
C11—H11⋯Cl1^{iv}	0.95	2.98	3.600(7)	124
C12—H12⋯Cl1	0.95	2.96	3.554(7)	122
C12—H12⋯Cl2^{v}	0.95	2.85	3.654(7)	142
C13—H13B⋯F1^{vi}	0.99	2.63	3.404(8)	135
C14—H14B⋯Cl2^{vii}	0.98	2.98	3.869(8)	151
O1—H1A⋯Cl3	0.88(8)	2.13(8)	3.010(5)	176(8)
N4—H4A⋯Cl3^{ii}	0.79(8)	2.58(9)	3.363(6)	177(8)
N5—H5A⋯Cl3^{iii}	0.83(8)	2.57(8)	3.374(6)	163(7)
C1—H1⋯Cl1	0.95	2.98	3.569(7)	121

Symmetry codes: (i) −x+3/2, y, z+1/2; (ii) −x+1, −y+1, z−1/2; (iii) −x+1/2, y, z−1/2; (iv) x−1/2, −y+2, z; (v) −x+1, −y+2, z+1/2; (vi) −x+1, −y+1, z+1/2; (vii) x, y, z+1.

Table 2.21 – Hydrogen-bonding in **2.4** (Å, °)

D—H···A	D—H	H···A	D···A	D—H···A
C1—H1···Cl1^{i}	0.95	2.89	3.410(5)	116
C1—H1···Cl2^{i}	0.95	2.83	3.609(5)	140
C1S—H1B···Cl3^{ii}	0.98	2.92	3.878(6)	166
C2—H2···Cl2^{iii}	0.95	2.92	3.598(5)	129
C3—H3···F1^{iv}	0.95	2.36	2.983(5)	123
C3S—H3B···Cl3^{v}	0.98	2.92	3.760(7)	144
C3S—H3C···Cl2^{vi}	0.98	2.88	3.720(7)	145
C9—H9···Cl3^{vii}	0.95	2.89	3.474(5)	121
C10—H10···Cl1	0.95	2.97	3.533(5)	119
C10—H10···Cl1^{viii}	0.95	2.70	3.334(4)	125
O1S—H1S···N1S	0.77(5)	2.19(5)	2.936(7)	165(6)
N4—H4A···O1S	0.88(6)	2.06(6)	2.843(5)	148(6)
N5—H5A···Cl3^{ix}	0.87(5)	2.43(5)	3.224(4)	152(5)

Symmetry codes: (i) x, −y+1/2, z+1/2; (ii) −x+1, −y+1, −z+2; (iii) x, y, z+1; (iv) −x+2, −y+1, −z+2; (v) −x+1, y+1/2, −z+3/2; (vi) −x+2, y+1/2, −z+3/2; (vii) x, y, z−1; (viii) x, −y+1/2, z−1/2; (ix) −x+1, −y+1, −z+1.

Table 2.22 – Hydrogen-bonding in **2.5** (Å, °)

D—H···A	D—H	H···A	D···A	D—H···A
C1—H1···F1^{i}	0.95	2.23	3.063(3)	146
C2—H2···Br3^{ii}	0.95	3.06	3.927(2)	153
C3—H3···Br1^{iii}	0.95	3.13	3.731(2)	123
C8—H8···F2^{iv}	0.95	2.49	3.106(3)	122
C9—H9···F2^{v}	0.95	2.56	3.290(3)	134
C10—H10···Br2^{vi}	0.95	2.94	3.847(3)	159
N4—H4A···Br3^{vii}	0.84(2)	2.77(2)	3.4829(18)	144(2)
N5—H5A···Br1^{viii}	0.85(2)	2.76(2)	3.4968(18)	147(2)

Symmetry codes: (i) x, y−1, z; (ii) −x+1, −y, −z; (iii) x+1, y, z; (iv) x−1, y, z; (v) −x, −y+1, −z+1; (vi) −x, −y, −z+1; (vii) −x+1, −y+1, −z; (viii) x, y+1, z.

Table 2.23 – Hydrogen-bonding in **2.6** (Å, °)

D—H···A	D—H	H···A	D···A	D—H···A
N4—H4A···O1^{i}	0.95	2.98	3.569(7)	121
N5—H5A···O2^{ii}	0.95	2.94	3.661(7)	134
C4—H4···O1^{i}	0.95	2.76	3.687(8)	164
C9—H9···O2^{ii}	0.95	2.63	3.549(7)	164
C9—H9···O2’ ^{ii}	0.95	2.98	3.600(7)	124
C12—H12···Cl1^{iii}	0.95	2.96	3.554(7)	122

Symmetry codes: (i) 1/2+x,3/2-y,z; (ii) -1/2+x,3/2-y,z; (iii) -1/2+x,1/2-y,z

Table 2.24 – Hydrogen-bonding in **2.7** (Å, °)

D—H···A	D—H	H···A	D···A	D—H···A
C1—H1···Br^{1}	0.95	3.08	3.688(8)	124
C1—H1···Br1^{ii}	0.95	2.92	3.556(8)	125
C1—H1···Br1	0.95	3.08	3.688(8)	124
C1—H1···Br1^{ii}	0.95	2.92	3.556(8)	125
C2—H2···Br2^{iii}	0.95	3.14	3.744(7)	123
C2—H2···Br2^{iii}	0.95	3.14	3.744(7)	123
C4—H4···O1^{iv}	0.95	2.38	3.27(2)	157
C4—H4···O1^{iv}	0.95	2.38	3.27(2)	157
C4—H4···O2^{v}	0.95	2.29	3.226(18)	167
C4—H4···O2^{v}	0.95	2.29	3.226(18)	167

Symmetry codes: (ii) −x+1, −y, −z+1; (iii) −x+1, y, −z+3/2; (iv) x, −y+1, z+1/2; (v) −x+1, −y+1, −z+1.

Table 2.25 – Hydrogen-bonding in **2.8** (Å, °)

D—H···*A*	*D*—H	H···*A*	*D*···*A*	*D*—H···*A*
O2—H·2A··O6^{i}	0.79(3)	1.88(3)	2.663(2)	175(3)
O2—H2B···O2S^{i}	0.85(2)	1.81(2)	2.651(2)	173(2)
N4—H4A···O7^{ii}	0.78(3)	2.14(3)	2.857(3)	153(3)
N5—H5A···O1S^{i}	0.82(3)	1.99(3)	2.812(2)	174(2)
C1—H1···O3	0.95	2.24	2.842(3)	121
C3S—H3C···F1^{iii}	0.98	2.54	3.339(3)	139
C4—H4···O6^{ii}	0.95	2.27	3.156(3)	155
C4S—H4C···O2S^{i}	0.98	2.44	3.287(3)	145
C8S—H8B···O8^{iv}	0.98	2.49	3.371(4)	149
C8S—H8C···O2S	0.98	2.16	2.623(4)	107
C9—H9···O1S^{i}	0.95	2.24	3.164(3)	164
C10—H10···O6^{i}	0.95	2.40	3.274(2)	153
C12—H12···O4	0.95	2.18	2.836(3)	125

Symmetry codes: Symmetry codes: (i) *x*, -1+*y*, *z*; (ii) *x*, 3/2-*y*, 1/2+*x*; (iii) -*x*,1-*y*,1-*z*; (iv)) -*x*,-1/2+*y*,1/2-*z*.

Table 2.26 – Hydrogen-bonding in **2.9** (Å, °)

D—H⋯*A*	*D*—H	H⋯*A*	*D*⋯*A*	*D*—H⋯*A*
O2—H2A⋯O4S^{i}	0.84(2)	1.77(2)	2.603(2)	170(3)
O2—H2B⋯O13^{ii}	0.82(2)	1.73(2)	2.552(3)	172(2)
N4—H4A⋯O1S^{i}	0.831(17)	2.245(17)	3.002(3)	151.5(18)
N4—H4A⋯N6	0.831(17)	2.46(2)	2.7992(2)	104.7(15)
N5—H4A⋯N7	0.867(19)	2.36(2)	2.749(3)	107.5(15)
N5—H5A⋯O11^{iii}	0.867(19)	2.10(2)	2.905(2)	153.4(19)
O6—H6A⋯O12^{i}	0.82(2)	1.78(2)	2.598(2)	173(2)
O6—H6A⋯O2S^{i}	0.80(2)	1.83(2)	2.624(2)	168(3)
N12—H12A⋯O3S^{ii}	0.874(17)	2.055(18)	2.824(2)	146.4(19)
N12—H12A⋯N14	0.874(17)	2.43(2)	2.791(3)	105.4(15)
N13—H13A⋯N15	0.858(19)	2.40(2)	2.747(3)	104.7(16)
N13—H13A⋯O14^{iv}	0.85(19)	2.02(2)	2.830(2)	158(2)
C1—H1⋯O3	0.95	2.30	2.919(3)	122
C1S—H1A⋯F1^{i}	0.98	2.36	3.292(3)	159
C1S—H1C⋯O10^{iii}	0.98	2.49	3.448(4)	167
C3—H3⋯O4^{v}	0.95	2.60	3.288(3)	130
C3—H3⋯O13^{i}	0.95	2.28	3.098(3)	144
C4S—H4B⋯O1S	0.98	2.22	2.675(3)	107
C8S—H8A⋯O2S	0.98	2.08	2.553(3)	108
C9S—H9C⋯O6^{i}	0.98	2.51	3.484(4)	176
C10—H10⋯O4	0.95	2.33	2.889(3)	117
C11—H11⋯O7	0.95	2.29	2.897(3)	121
C11S—H11B⋯O15^{vi}	0.98	2.51	3.442(4)	160
C12S—H12D⋯O3S	0.98	2.29	2.712(4)	105
C13—H13⋯O12^{ii}	0.95	2.29	3.156(3)	151
C13S—H13D⋯O15^{ii}	0.98	2.54	3.467(4)	159
C20—H20⋯O8	0.95	2.32	2.887(3)	118

Symmetry codes: (i) *x*, *y*, *z*; (ii)*x*, 1+*y*, *z*; (iii) 1-*x*,1/2+*y*,3/2-*z*; (iv) 2-*x*,1/2+*y*,3/2-z; (v) *x*,-1+*y*,*z*; (vi) *x*,1/2-*y*,-1/2+*z*.

Table 2.27 Hydrogen-bonding in **2.10** (Å, °)

D—H⋯A	D—H	H⋯A	D⋯A	D—H⋯A
O2—H2A⋯O6^{i}	0.82(5)	2.46(5)	3.118(5)	138(4)
O2—H2A⋯O7^{i}	0.82(5)	2.06(5)	2.866(5)	168(4)
N4—H4A⋯O6^{ii}	0.84(3)	2.00(4)	2.819(5)	168(5)
N5—H5A⋯O7^{iii}	0.85(3)	2.02(4)	2.745(5)	143(3)
C1—H1⋯O4’	0.95	2.14	2.886(17)	135
C2—H2⋯O5^{iv}	0.95	2.27	3.167(7)	158
C2—H2⋯O5’^{iv}	0.95	2.52	3.425(14)	158
C3—H3⋯O3^{ii}	0.95	2.51	3.262(8)	136
C4—H4⋯O6^{ii}	0.95	2.31	3.222(6)	162
C9—H9⋯O8^{iii}	0.95	2.59	3.520(6)	167
C11—H11⋯O4^{v}	0.95	2.45	3.370(10)	163
C12—H12⋯O3’	0.95	2.30	2.908(18)	121
C13—H13B⋯O3	0.98	2.48	2.952(8)	109

Symmetry codes: (i) *x*, *y*, *z*; (ii) *x*,3/2-*y*,1/2+z; (iii) 1-*x*,1-*y*,2-z; (iv) 2-*x*,1/2+*y*,3/2-*z*; (v) 2-*x*,-1/2+*y*,3/2-*z*.

Table 2.28 Hydrogen-bonding in **2.11** (Å, °)

D—H···*A*	*D*—H	H···*A*	*D*···*A*	*D*—H···*A*
C1—H1···O3	0.95	2.21	2.840(3)	123
C2—H2···O5^{i}	0.95	2.52	3.419(3)	157
C7—H7···O6^{ii}	0.95	2.48	3.384(2)	158
C15—H15···O4	0.95	2.19	2.812(2)	122
O2—H2A···N5	0.81(3)	2.54(3)	3.313(2)	159 (2)
O2—H2A···O6	0.81(3)	1.88(3)	2.676(2)	166 (3)
O2—H2A···O7	0.81(3)	2.53(3)	3.151(2)	134 (2)
O2—H2B···N5^{iii}	0.76(3)	2.64(3)	3.349(2)	158 (3)
O2—H2B···O7^{iii}	0.76(3)	2.61(3)	3.163(2)	131 (3)
O2—H2B···O8^{ii}	0.76(3)	1.96(3)	2.717(2)	174 (3)

Symmetry codes: (i) −*x*+1/2, *y*+1/2, −*z*+1/2; (ii) *x*, *y*+1, *z*; (iii) −*x*+3/2, *y*+1/2, −*z*+1/2.

Table 2.29 – Hydrogen-bonding in **2.12** (Å, °)

D—H···*A*	*D*—H	H···*A*	*D*···*A*	*D*—H···*A*
C1—H1···O4	0.95	2.21	2.837 (3)	123
C2—H2···O9^{i}	0.95	2.43	3.365 (4)	167
C7—H7···O15^{ii}	0.95	2.30	3.223 (3)	165
C8—H8···O14^{iii}	0.95	2.58	3.199(4)	123
C9—H9···O13^{iii}	0.95	2.49	3.407 (3)	164
C15—H15···O3	0.95	2.18	2.808 (3)	123
C15—H15···O8^{iv}	0.95	2.50	3.291 (3)	141
C23—H23···O10^{iv}	0.95	2.50	3.215 (3)	132
C24—H24···O11^{iv}	0.95	2.56	3.409(3)	148
C25—H25···O11^{v}	0.95	2.57	3.222 (3)	126
C25—H25···O12^{v}	0.95	2.47	3.419 (4)	174
C28—H28···O12^{v}	0.95	2.59	3.535 (3)	175
O2—H2A···O15^{vii}	0.81 (2)	1.79 (2)	2.560 (3)	159 (3)
O6—H6A···O10	0.77 (2)	1.90 (2)	2.634 (3)	160 (3)

Symmetry codes: (i) *x*, *y*+1, *z*; (ii) *x*−1, *y*, *z*+1; (iii) −*x*+1, −*y*+1, −*z*+1; (iv) *x*+1, *y*, *z*; (v) −*x*+1, −*y*+2, −*z*+1; (vi) *x*−1, *y*, *z*; (vii) *x*, *y*, *z*+1.

Table 2.30 – Hydrogen-bonding in **2.13** (Å, °)

D—H···*A*	*D*—H	H···*A*	*D*···*A*	*D*—H···*A*
C1—H1···N14	0.95	2.60	3.549 (12)	174
C2—H2···F4^{i}	0.95	2.45	3.176 (10)	133
C4—H4···O1S^{ii}	0.95	2.27	3.191 (13)	163
C9—H9···S2^{iii}	0.95	3.01	3.930 (11)	163
C23—H23···S4^{iv}	0.95	2.72	3.651 (10)	168
C26—H26···N6	0.95	2.63	3.517 (12)	156
C1*S*—H1*S*3···F3^{v}	0.98	2.35	3.193 (17)	144
O1*S*—H1S···S4^{i}	0.83 (2)	2.37 (3)	3.195 (9)	175 (17)
N4—H4A···O1S^{ii}	0.87 (2)	1.93 (4)	2.781 (13)	165 (11)
N5—H5A···S2^{iii}	0.87 (2)	2.58 (3)	3.411 (8)	161 (7)
N11—H11A···F2^{vi}	0.87 (2)	2.07 (4)	2.888 (8)	156 (8)
N12—H12A···S4^{iv}	0.87 (2)	3.00 (7)	3.765 (9)	148 (11)

Symmetry codes: (i) −*x*+1, −*y*, −*z*+1; (ii) *x*, *y*, *z*−1; (iii) −*x*+1, −*y*+1, −*z*; (iv) −*x*+2, −*y*, −*z*+1; (v) *x*−1, *y*, *z*; (vi) *x*, *y*, *z*+1.

Table 2.31 – Hydrogen-bonding in **2.14** (Å, °)

D—H⋯*A*	*D*—H	H⋯*A*	*D*⋯*A*	*D*—H⋯*A*
N4—H4⋯Cl1$^{\mathrm{i}}$	0.88	2.55	3.3091(16)	145
N5—H5⋯Cl1$^{\mathrm{ii}}$	0.88	2.50	3.2164(17)	139
N5—H5⋯Cl2$^{\mathrm{iii}}$	0.88	2.79	3.3529(17)	123
C3—H3⋯F1$^{\mathrm{iv}}$	0.95	2.49	3.059(3)	119
C11—H11⋯Cl2$^{\mathrm{v}}$	0.95	2.71	3.642(2)	167

Symmetry codes: (i) x,3/2-y,1/2+z; (ii) *-x,1-y,1-z*; (iii) 1-x,1-y,1-z; (iv) -x,1/2+y,3/2-z; (v) *1-x,-1/2+y,1/2-z*.

Table 2.32 – Hydrogen-bonding in **2.15** (Å, °)

D—H⋯*A*	*D*—H	H⋯*A*	*D*⋯*A*	*D*—H⋯*A*
N2—H2A⋯Cl1$^{\mathrm{i}}$	0.90(6)	2.53(6)	3.309(7)	146(4)
N3—H3A⋯Cl1$^{\mathrm{ii}}$	0.83(6)	2.49(6)	3.200(7)	144(5)
C1—H1⋯F2$^{\mathrm{iii}}$	0.95	2.55	3.473(9)	165
C3—H3⋯F1$^{\mathrm{iv}}$	0.95	2.50	3.080(9)	120
C4—H4⋯F1$^{\mathrm{iv}}$	0.95	2.53	3.090(8)	117
C11—H11⋯Cl2$^{\mathrm{v}}$	0.95	2.70	3.633(7)	167
C12—H12⋯F2$^{\mathrm{vi}}$	0.95	2.55	3.269(8)	133

Symmetry codes: (i) x,3/2-y,-1/2+z; (ii) *2-x,1-y,1-z*; (iii) x,3/2-y,1/2+z; (iv) 2-x,1/2+y,1/2-z; (v) *1-x,-1/2+y,3/2-z*; (vi) *1-x,1-y,1-z*.

Table 2.33 Hydrogen-bonding in **2.16** (Å, °)

D—H⋯*A*	*D*—H	H⋯*A*	*D*⋯*A*	*D*—H⋯*A*
N1—H1A⋯Br2$^{\mathrm{i}}$	0.85(3)	2.69(3)	3.500(3)	162(2)
O1—H1B⋯Br2$^{\mathrm{ii}}$	0.81(3)	2.63(3)	3.414(2)	164(4)
N2—H2A⋯Br1$^{\mathrm{iii}}$	0.849(17)	2.63(2)	3.427(2)	158(3)
C3—H3⋯Br1$^{\mathrm{iv}}$	0.95	2.82	3.558(3)	135
C12—H12⋯F1$^{\mathrm{v}}$	0.95	2.35	3.123(4)	138
C13—H13B⋯F1$^{\mathrm{v1}}$	0.98	2.42	3.280(4)	146

Symmetry codes: (i) -1+x,y,z; (ii) 2-x,1-y,1-z; (iii) 1-x,-1/2+y,1/2-z; (iv) 1-x,1/2+y,1/2-z; (v) 1+x,y,z; (vi) 1+x,1/2-y,1/2+z.

Table 2.34 Hydrogen-bonding in **2.17** (Å, °)

D—H⋯*A*	*D*—H	H⋯*A*	*D*⋯*A*	*D*—H⋯*A*
O1—H1A⋯Br2$^{\mathrm{i}}$	0.80(3)	2.53(3)	3.313(3)	168(5)
N2—H2A⋯O1	0.86(4)	1.97(6)	2.782(4)	155(8)
N2—H2A⋯N5	0.86(4)	2.40(8)	2.796(4)	109(7)
N3—H3A⋯N7	0.87(6)	2.40(7)	2.778(4)	107(7)
N3—H3A⋯Br1$^{\mathrm{ii}}$	0.87(6)	2.72(8)	3.466(3)	145(6)
C10—H10⋯F1$^{\mathrm{iii}}$	0.95	2.42	3.308(4)	156

Symmetry codes: (i) 1/2-x,-1/2+y,3/2-z; (ii) 1/2+x,3/2-y,1/2+z; (iii) -1/2+x,3/2-y,-1/2+z.

2.9 References

1. K. G. M. Laurier, F. Vermoortele, R. Ameloot, D. E. De Vos, J. Hofkens, and M. B. J. Roeffaers, *J. Am. Chem. Soc.*, 2013, **135**, 14488.
2. S. Telitel, F. Dumur, D. Campolo, J. Poly, D. Gigmes, J. P. Fouassier, and J. Lalevée, *J. Polym. Sci. Part A Polym. Chem.*, 2016, **54**, 702.
3. P. Salvatori, G. Marotta, A. Cinti, E. Mosconi, M. Panigrahi, L. Giribabu, M. K. Nazeeruddin, and F. De Angelis, *Inorg. Chim. Acta*, 2013, **406**, 106.
4. H. Li and Y. Li, *Nanoscale*, 2009, **1**, 128.
5. T. Sarkar, S. Banerjee, A. Hussain, *RSC Adv.*, 2015, **5**, 16641
6. S. Mossin, B. L. Tran, D. Adhikari, M. Pink, F. W. Heinemann, J. Sutter, R. K. Szilagyi, K. Meyer and D. J. Mindiola, *J. Am. Chem. Soc.*, 2012, **134**, 13651
7. S. Hayami, Y. Komatsu, T. Shimizu, H. Kamihata and Y. H. Lee, *Coord. Chem. Rev.*, 2011, **255**, 1981
8. M. Murrie, *Chem. Soc. Rev.*, 2010, **39**, 1986
9. E. Bauer, *Iron Cataysis II*, 2015, **50**, Springer, Switzerland
10. G. Cahiez, A. Moyeux, *Chem. Rev.* 2010, **110**, 1435
11. K. S. Egorova and V. P. Ananikov, *Angew. Chem. Int. Ed.*, 2016, **55**, 12150
12. K. S. Egorova and V. P. Ananikov, *Organometallics*, 2017, **36**, 4071
13. D. Casanova, M. Llunell, P. Alemany, S. Alvarez, *Chem. Eur. J.*, 2005, **11,** 1479
14. A. Loudet and K. Burgess, *Chem. Rev.*, 2007, **107**, 4891
15. A. M. Tondreau, C. C. H. Atienza, J. M. Darmon, C. Milsmann, H. M. Hoyt, K. J. Weller, S. A. Nye, K. M. Lewis, J. Boyer, J. G. P. Delis, E. Lobkovsky and P. J. Chirik, *Organometallics*, 2012, **31**, 4886
16. S. A. Cotton, V. Franckevicius, J. Fawcett, *Polyhedron*, 2002, **21**, 2055
17. Y. Nakayama, Y. Baba, H. Yasuda and K. Kawakita, *Macromolecules*, 2003, **36**, 7953
18. J. England, C. C. Scarborough, T. Weyhermüller, S. Sproules and K. Wieghardt, *Eur. J. Inorg. Chem.*, 2012, **2012**, 4605
19. G. A. Jeffrey, H. Maluszynska and J. Mitra, *Int. J. Biol. Macromol.*, 1985, **7**, 336
20. G. A. Jeffrey and W. Saenger, *Hydrogen Bonding in Biological Structures*, 1991, Springer Nature, Switzerland
21. T. Steiner, *Crystallogr. Rev.*, 1996, **6**, 1
22. O. Kahn, *Molecular Magnetism*, 1993, VCH, United States of America
23. M. J. Frisch, G. W. Trucks, H. B. Schlegel, G. E. Scuseria, M. A. Robb, J. R. Cheeseman,G. Scalmani, V. Barone, B. Mennucci, G. A. Petersson, H. Nakatsuji, M. Caricato, X. Li, H. P. Hratchian, A. F. Izmaylov, J. Bloino, G. Zheng, J. L. Sonnenberg, M. Hada, M. Ehara, K.Toyota, R. Fukuda, J. Hasegawa, M. Ishida, T. Nakajima, Y. Honda, O. Kitao, H. Nakai, T. Vreven, J. J. A. Montgomery, J. E. Peralta, F.Ogliaro, M. Bearpark, J. J. Heyd, E. Brothers, K. N. Kudin, V. N. Staroverov, R. Kobayashi, J. Normand, K. Raghavachar, A. Rendell, J. C. Burant, S. S. Iyengar, J. Tomasi, M. Cossi, N. Rega, J. M. Millam, M. Klene, J. E. Knox, J. B. Cross, V. Bakken, C. Adamo, J. Jaramillo, R.Gomperts, R. E. Stratmann, O. Yazyev, A. J. Austin, R. Cammi, C. Pomelli, J. W. Ochterski, R. L. Martin, K. Morokuma, V. G. Zakrzewski, G. A. Voth, P. Salvador, J. J. Dannenberg, S. Dapprich, A. D. Daniels, O. Farkas, J. B. Foresman, J. V. Ortiz, J.

Cioslowski and D. J. Fox, Gaussian 09, Revision A.02; Gaussian, Inc.: Wallingford, CT, 2009

24. J. P. Mcnamara, M. Sundararajan, I. H. Hillier, J. Ge, A. Campbell, and C. Morgado, *J. Comput. Chem*., 2006, **27**, 12, 1307
25. J. Tirado-Rives and W. Jorgensen, *J. Chem. Theory Comput.*, 2008, **4**, 297
26. V. A. Rassolov, M. A. Ratner, J. A. Pople, P. C. Redfern and L. A. Curtiss, *J. Comput. Chem.*, 2001, **22**, 9, 976
27. M. Yousaf, N. J. Yutronkie, R. Castañeda, J. A. Klein and J. Brusso, *New J. Chem.*, 2017, **41**, 12218
28. R. E. Stenkamp, L. C. Sieker and L. H. Jensen, *J. Am. Chem. Soc.*, 1984, **106**, 618
29. H. Basch, K. Mogi, D. G. Musaev, K. Morokuma, *J. Am. Chem. Soc.*, 1999, **121**, 7249
30. M. Chino, O. Maglio, F. Nastri, V. Pavone, W. F. Degrado and A. Lombardi, *Eur. J. Inorg. Chem.*, 2015, **2015**, 3371
31. E. Safaei, Z. Alaji, F. Panahi, A. Wojtczak and J. Z. Jagličić, *New J. Chem.*, 2018, **42**, 7230
32. J. Chen and W. R. Browne, *Coord. Chem. Rev.*, 2018, **374**, 15
33. B. Chandra, K. K. Singh and S. Sen Gupta, *Chem. Sci.*, 2017, **8**, 7545
34. J. Rosenthal, T. D. Luckett, J. M. Hodgkiss and D. G. Nocera, *J. Am. Chem. Soc.*, 2006, **128**, 6546
35. J. Chen, S. Stepanovic, A. Draksharapu, M. Gruden and W. R. Browne, *Angew. Chem. Int. Ed.*, 2018, **57**, 3207
36. H. Eguchi, M. Umemura, R. Kurotani, H. Fukumura, I. Sato, J. H. Kim, Y. Hoshino, J. Lee, N. Amemiya, M. Sato, K. Hirata, D. J. Singh, T. Masuda, M. Yamamoto, T. Urano, K. Yoshida, K. Tanigaki, M. Yamamoto, M. Sato, S. Inoue, I. Aoki and Y. Ishikawa, *Sci. Rep.*, 2015, **5**, 1
37. P. A. Thornley, J. C. Starkey, R. Zibaseresht, M. I. J. Polson, J. L. Wikaira and R. M. Hartshorn, *J. Coord. Chem.*, 2011, **64**, 145
38. M. Yoshida, M. Kondo, T. Nakamura, K. Sakai and S. Masaoka, *Angew. Chem. Int. Ed.*, 2014, **53**, 11519
39. R. Bagai, K. A. Abboud and G. Christou, *Inorg. Chem.*, 2007, **46**, 5567
40. V. Bhatt, *Essentials of Coordination Chemistry a Simplified Approach with 3D Visuals*, 2016, Elsevier, London
41. N. E. Bresse and M. O. Keeffe, *Acta Cryst*., 1991, **B47**, 192
42. I. D. Brown, *The Chemical Bond in Inorganic Chemistry*, 2016, Oxford University Press, Oxford
43. J. A. Real, A. B. Gaspar, V. Niel and M. C. Muñoz, *Coord. Chem. Rev.*, 2003, **236**, 121
44. M. A. Halcrow, *Crystals*, 2016, **6**, 58
45. A. Jouaiti, V. Jullien, M. W. Hosseini, J. M. Planeix and A. De Cian, *Chem. Commun.*, 2001, **2001**, 1114
46. Y. Zhang, K. L. M. Harriman, G. Brunet, A. Pialat, B. Gabidullin and M. Murugesu, *Eur. J. Inorg. Chem.*, 2018, **2018**, 1212
47. Bruker, *APEX2*, 2012, Bruker AXS Inc., Madison, Wisconsin, USA
48. G. M. Sheldrick, *Acta Crystallogr. Sect. C Struct. Chem.*, 2015, **71**, 3

CHAPTER 3

3.0 Azido-bridging in First Row Transition Metal Complexes

Most terpy-based complexes yield primarily mononuclear species upon coordination; however, there are some examples of dinuclear complexes formed serendipitously upon reacting with certain metal salts (e.g., chlorides, hydroxides, azides, etc.).[1–4] The use of bridging anions in the coordination of paramagnetic metal ions has proven to be advantageous in the field of molecular magnetism, due in large part to the ability of bridging groups to promote exchange interactions that can give rise to magnetic behaviours such as ferromagnetism and antiferromagnetism.[3,5] In that regard, the aforementioned bridging anions tend to yield antiferromagnetically coupled systems through a weak superexchange pathway, a consequence of the angle between the bridging ligand and the two metal centres.[6,7]

On the other hand, azide (N_3^-) counter ions are highly desirable in coordination chemistry, as they can bind through various modes leading to the generation of polymetallic structures. With respect to magnetic exchange between paramagnetic metal ions, the azido bridge plays a key role that is dependent on the bridging mode (e.g., end-to-end (EE): μ-1,3; end on (EO): μ-1,1; Figure 3.1). This may be attributed to parameters such as the bridging angle (M-N-M) and metal-metal bond distances, which can influence spin polarization, delocalization of unpaired electrons, and the magnetic orbitals of spin centres; all of which have been identified as major contributors to the strength and sign of the magnetic coupling.[8–11] For example, EE azido bridges typically lead to antiferromagnetic (AF) interactions, whereas EO coordination modes are associated with ferromagnetic (FM) interactions.[12,13]

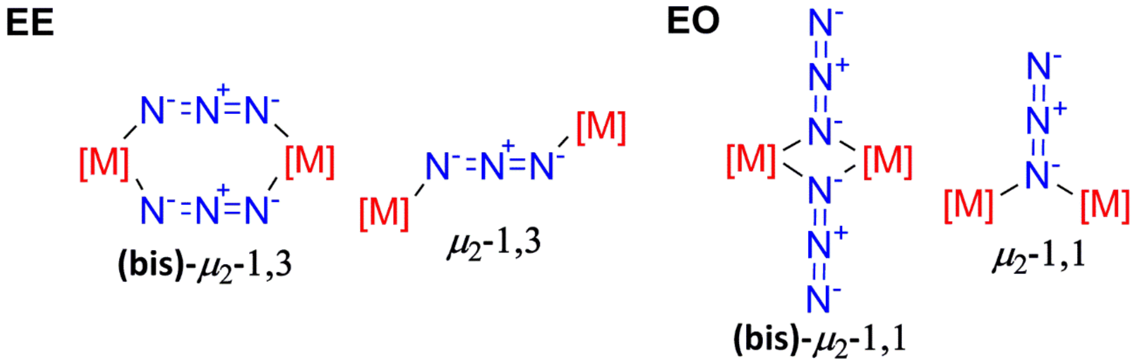

Figure 3.1 – Selected end-to-end (EE; left) and end-on (EO; right) azido bridging modes in dinuclear complexes.

The magnetic properties of EO azido bridged complexes are well documented for many first-row transition metals, and Co^{II} complexes in particular have been shown to display attractive magnetic characteristics.[14–16] In the case of μ-1,1 azido bridged dinuclear Co^{II} complexes, all reported examples exhibit FM interactions resulting from the acute bridging angles afforded by the end-on azide bridge. [17–20] Interestingly, Fe^{II} ions coordinated by two μ-1,1-N_3 moieties are much rarer, with only four examples reported and each of high nuclearity ($n \geq 4$). [21–24] Considering EO azido bridged dinuclear iron complexes, the only examples reported to date possess Fe^{III} ions, [25–28] highlighting the rarity of double end-on azide bridging motifs in iron chemistry. We have therefore focused our attention on the development of EO azido bridged dinuclear Fe^{II} and Co^{II} complexes, taking advantage of the terpy-like framework afforded by Py_2F_2BTA.

3.1.1 Synthesis and Structural Properties of Dinuclear M^{II} Complexes Based on a Boratriazine Ligand Framework

Here our goal is two-fold, by employing Py_2F_2BTA with azide counterions, we anticipate generating high spin Fe^{II} and Co^{II} complexes, which are known for their unquenched first order orbital angular momentum, an important source of anisotropy necessary for Single-Molecule Magnets (SMMs). Furthermore, the formation of dinuclear complexes through the bridging N_3^-

anion can facilitate ferromagnetic interactions, due to the acute M-N-M angle afforded by the end on azido groups, and therefore generate molecules with large spin ground states. To that end, herein are reported the structure and magnetic properties of two novel double EO azido bridged dinuclear complexes; a Co^{II} species and its isostructural Fe^{II} analogue, which shows SMM behaviour and represents the first magnetic report of a dinuclear EO azido bridged Fe^{II} complex.

The two compounds reported here were prepared using similar methodology, with the key difference being the concentration of the reactions. In particular, an EO azido-bridged dinuclear Fe^{II} complex can be isolated upon adding a stirred methanolic solution of $FeCl_2$ and NaN_3 into a solution of Py_2F_2BTA in acetonitrile. Following filtration, the solution was sealed and left to stand at room temperature for 48 hrs, after which time $[Fe_2^{II}(\mu_{1,1}\text{-}N_3)_2(Py_2F_2BTA)_2(N_3)_2]$ (**3.1**) crystallized out as green blocks suitable for SCXRD. Alternatively, when $CoCl_2$ is employed, $[Co_2^{II}(\mu_{1,1}\text{-}N_3)_2(Py_2F_2BTA)_2(N_3)_2]$ (**3.2**) crystallizes within 24 hrs as orange blocks suitable for SCXRD analysis. For both compounds, bulk purity and composition of the as-synthesized products were confirmed through SCXRD and PXRD (presented at the end of this chapter).

Single crystal X-ray analysis reveals that **3.1** and **3.2** crystallize in the monoclinic $P2_1/c$ space group (Figure 3.2 and Table 3.1), with an asymmetric unit containing a metal ion (either Fe^{II} or Co^{II}) coordinated in *mer* fashion to a neutral Py_2F_2BTA ligand. The asymmetric unit is completed with two azide anions coordinated in an EO manner, one of which is bridging to a second metal ion (e.g., Fe1A or Co1A). As such, the metal ions adopt a six-coordinate arrangement with two μ-1,1 azide anions between the two metal centres resulting in geometries that are best described as a distorted octahedron, as determined using the SHAPE[29] software (Figure 3.3 and Table 3.2). The similarities between the two complexes continue upon considering the supramolecular interactions, in which a number of short contacts exist including one $F\cdots\pi$ interaction centered on a neighbouring pyridyl group, as well as interactions between the terminal nitrogen atoms of the axial azido ligands, resulting in two N-H···N and two C-H···N interactions, and one C-H···F contact (Figure 3.4).

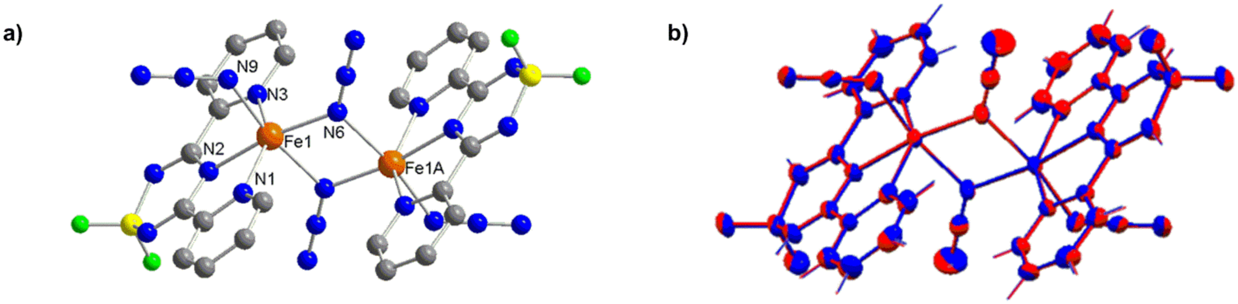

Figure 3.2 – a) Molecular structure of [Fe$_2^{II}$($\mu_{1,1}$-N$_3$)$_2$(Py$_2$F$_2$BTA)$_2$(N$_3$)$_2$], which includes labelling for key atoms within the molecular unit. b) Overlay of complexes [Fe$_2^{II}$($\mu_{1,1}$-N$_3$)$_2$(Py$_2$F$_2$BTA)$_2$(N$_3$)$_2$] (**3,1**, red) and [Co$_2^{II}$($\mu_{1,1}$-N$_3$)$_2$(Py$_2$F$_2$BTA)$_2$(N$_3$)$_2$] (**3.2**, blue) using 50% thermal ellipsoids.

Table 3.1 – Selected bond lengths (Å) for complexes **3.1** and **3.2**.

Distance	3.1	3.2
M1–N1	2.191(3)	2.166(5)
M1–N2	2.120(2)	2.074(4)
M1–N3	2.195(3)	2.170(5)
M1–N6	2.063(3)	2.060(4)
M1–N6(a)	2.240(3)	2.163(4)
M1–N9	2.168(2)	2.155(4)
M1–M1(a)	3.3461(7)	3.280(1)

Table 3.2 – Results from Shape analysis. Ideal geometry is a zero value, distortion from this geometry increases the value of the continuous shape measures.

	HP-6	PPY-6	OC-6	TBR-6	JPPY-6
3.1	34.28	21.45	2.79	11.11	25.46
3.2	34.35	21.34	2.67	11.03	25.40

HP-6: Hexagon (D_{6h}); PPY-6: Pentagonal pyramid (C_{5v}); OC-6: Octahedron (O_h); TPR-6: Trigonal prism (D_{3h}); JPPY-6: Johnson pentagonal pyramid (C_{5v})

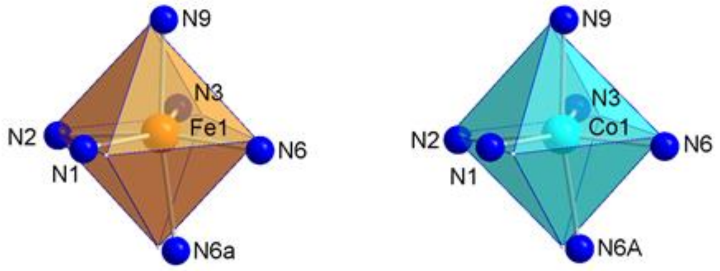

Figure 3.3 – Deviation from ideal octahedral environment about the metal ion in complexes **3.1** (left) and **3.2** (right)

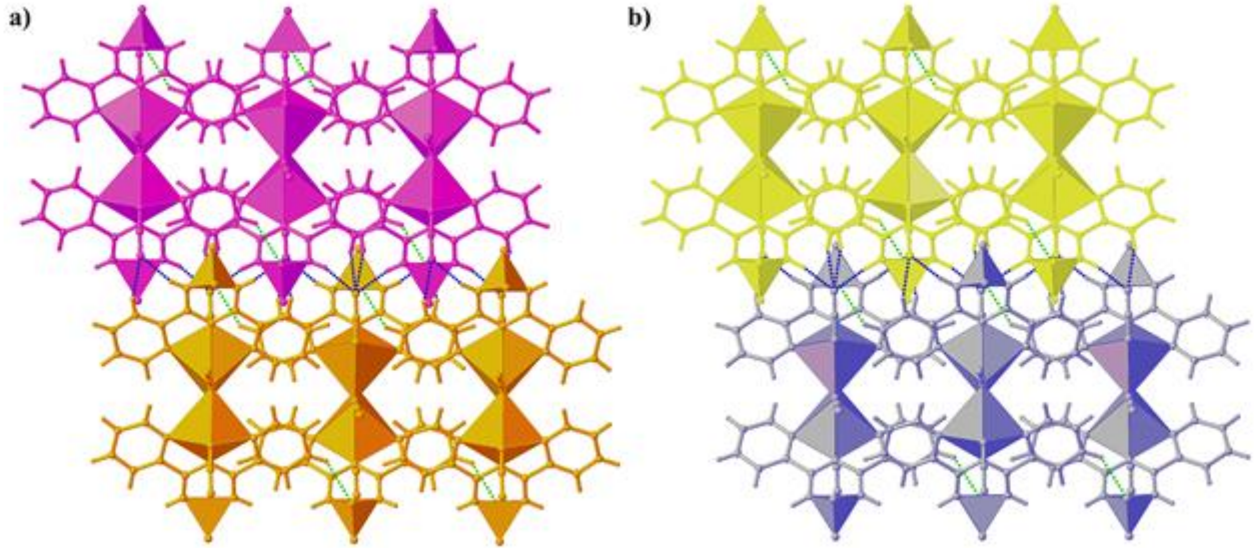

Figure 3.4 – Crystal packing diagram of complex a) **3.1** and b) **3.2**. Hydrogen bonds are denoted as green (F···H–A) and blue (N···H–A) dotted lines. Polyhedra added to show orientation of units.

Perhaps unsurprisingly, there is little deviation between the angles and distances in complexes **3.1** and **3.2**, which is highlighted by the overlay of the two structures shown in Figure 3.2. As a consequence of the azido bridging ligands, the Fe1-N6-Fe1A and Co1-N6-Co1A angles measure 102.0°, resulting in relatively close intramolecular M-M distances of 3.346(1) Å and 3.280(1) Å for Fe^{II}-Fe^{II} and Co^{II}-Co^{II}, respectively. As such, not only is the first report of a binuclear Fe^{II} complex that possesses EO *bis*(μ-1,1 azido) bridging anions, but in the case of **3.2**, the complex presented here represents the second smallest Co^{II}-N-Co^{II} angle reported for EO azido-bridged Co^{II} binuclear structures. Such features are particularly attractive in the design of molecular magnets.

3.1.2 Magnetic Properties of Ferromagnetically Coupled Dinuclear M^{II} Complexes Based on a Boratriazine Ligand Framework

To investigate the magnetic behaviour of both the Fe^{II} (**3.1**) and Co^{II} (**3.2**) analogs, variable-temperature magnetic susceptibility data was collected on solid samples. Under a static (dc) field of 1000 Oe, the χT values were determined to be 7.96 and 6.40 cm^3 K mol^{-1} at 300 K for **3.1** and

3.2, respectively (Figure 3.5). These χT values are within range of the expected 7.03 and 5.93 cm^3 K mol^{-1} values for two non-interacting Fe^{II} and Co^{II} ions, respectively, when considering the calculated Landé *g*-factors resulting from the best-fit of the magnetic data (*vide infra*). The slightly higher values are also suggestive of ferromagnetic interactions present at high temperatures, which is supported by the fact that the χT curve does not fully saturate at 300 K. Indeed, upon decreasing the temperature, we observe an increase of the χT product in both analogs, testifying to the presence of ferromagnetic interactions. Such behaviour is well-known to originate from end-on azide bridges with acute bridging angles, which promotes magnetic-orbital orthogonality.[17–20] To the best of our knowledge, only four examples exists of Fe^{II} ions being bridged exclusively by two EO-N_3 moieties; however, each consist of high nuclearity compounds.[21–24] The other few examples reported feature Fe^{III} ions,[25–28] thus illustrating the lack of instances in iron chemistry for double end-on azide bridging motifs. While the χT product in **3.2** exhibits a rather broad peak at low temperatures, the distinct peak in **3.1** allows us to confirm a spin ground state of $S_T = 4$ using $g = 2.16$. This is evidenced by the maximal χT value of 11.63 cm^3 K mol^{-1} at 20 K, which is in excellent agreement with the theoretical value of 11.66 cm^3 K mol^{-1}. The final decrease at low temperature can be ascribed to the partial depopulation of excited magnetic states and zero-field splitting effects.

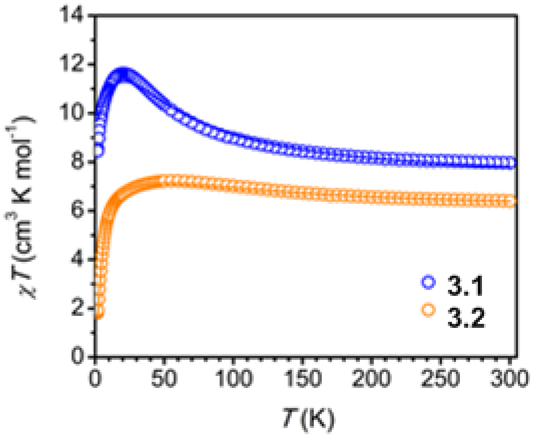

Figure 3.5 – Variable-temperature dc magnetic susceptibility ($\chi = M/H$ per mole of compound) data for **3.1** (blue spheres) and **3.2** (orange spheres), collected under an applied field of 1000 Oe. The solid lines correspond to the best fit using the magnetic model described in the main text.

To provide further insights into the magnetic exchange interaction between the two metal centres, we have successfully fit the experimental data (χT *vs*. T and M *vs*. H; Figure 3.5 and 3.6) using the program *PHI*[30] and the Hamiltonian : $H = -2J(S_1 \cdot S_2) + D\sum S_{i,z}^2$, where J is the coupling constant between the two metal ions, S_i is the spin operator for each metal ion, and D is the axial zero-field splitting parameter. Here, given the centrosymmetric nature of both dinuclear compounds, we employed a two-fold symmetric model where both Co^{II} and Fe^{II} ions are equivalent and used a single axial D parameter for collinear anisotropies. The resulting parameters (Table 3.3) suitably reproduce the magnetic data. It should be noted that attempts were made to fit **3.1** using a positive D; however, simultaneous fitting of the susceptibility and magnetization data was not possible, resulting in rather poor fits. The use of a negative D significantly improved the fitting procedure. Alternatively, the use of a negative D value for **3.2** yielded fitting parameters that were physically unreasonable. Furthermore, the obtained parameters are in line with other octahedral Co^{II} ions that have reported large and positive D values and $g > 2$.[31,32] The difference in the sign of D between **3.1** and **3.2** may contribute to the fact that only **3.1** exhibits an ac signal (*vide infra*). In terms of the coupling strength mediated by a double EO azido bridge, both J values are within the same range as one another, despite a change in the selected metal ion (Fe^{II} *versus* Co^{II}).

Moreover, it is of a comparable magnitude to those observed in similarly bridged Fe^{II} and Fe^{III} complexes.[21,28]

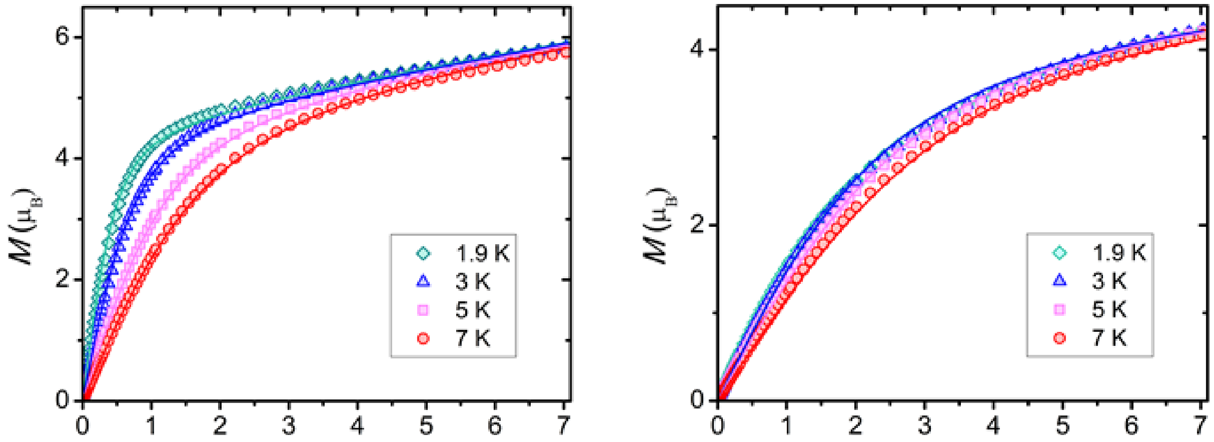

Figure 3.6 – *M vs H* plots for complex **3.1** (left) and **3.2** (right), between 1.9 and 7 K. The solid lines correspond to the best fit obtained using the model described in the main text.

Table 3.3 – Parameters used for the spin Hamiltonian models of **3.1** and **3.2**.

Parameter	**3.1**	**3.2**
g	2.16(5)	2.51(6)
D (cm^{-1})	-6.0(4)	17.3(9)
J (cm^{-1})	5.7(9)	7.1(9)

AC susceptibility measurements were also performed on both samples, however, under an applied static field an out-of-phase signal was only detected for **3.1**. As previously stated, this may be due to the significant transverse anisotropy found in **3.2** and the inability of an external dc field to adequately suppress tunnelling effects. Thus, focusing on **3.1**, we measured the out-of-phase magnetic susceptibility (χ'') under varying applied dc fields and at 1.9 K (Figure 3.7). No ac signal is detected under zero dc field, however, upon application of increasingly higher fields clear peaks begin to appear. This behaviour is commonly observed in cases where the magnetic relaxation is highly influenced by quantum tunnelling of the magnetization.[33,34] Subsequently, we performed ac measurements under an optimal static dc field of 1600 Oe, which revealed the emergence of two well-separated peaks, indicating that at least two magnetic relaxation processes are operative in this range (Figure 3.8). The slow relaxation phase, centred around 1 Hz, exhibits peaks that are essentially overlapped on top of one another. As such, we expect magnetic relaxation times that are minimally influenced by the temperature, as observed in a number of other transition metal complexes featuring similar field-induced behaviour.[35,36] It has been previously demonstrated through doping experiments that the low frequency relaxation phase can be attributed to intermolecular interactions, where at increasing higher applied dc fields, the metal centres begin to interact.[37] This is also evident by the strong field dependence of this relaxation phase, which gains in intensity as the strength of the field increases (Figure 3.7). On the other hand, the fast relaxation phase does show shifting of the peaks below 2.2 K, suggesting a dependence of the relaxation times at low temperatures. Given the fact that this behaviour is only observable at very low temperatures and under high dc external magnetic fields, we have focused our attention on the other novel features of this compound. While two or even three relaxation processes have been observed in a number of Dy^{III}, Co^{II}, Ni^{II} and Cu^{II} complexes,[35,36,38] **3.1** represents a rare example of an Fe-based system displaying two distinct relaxation mechanisms.[39]

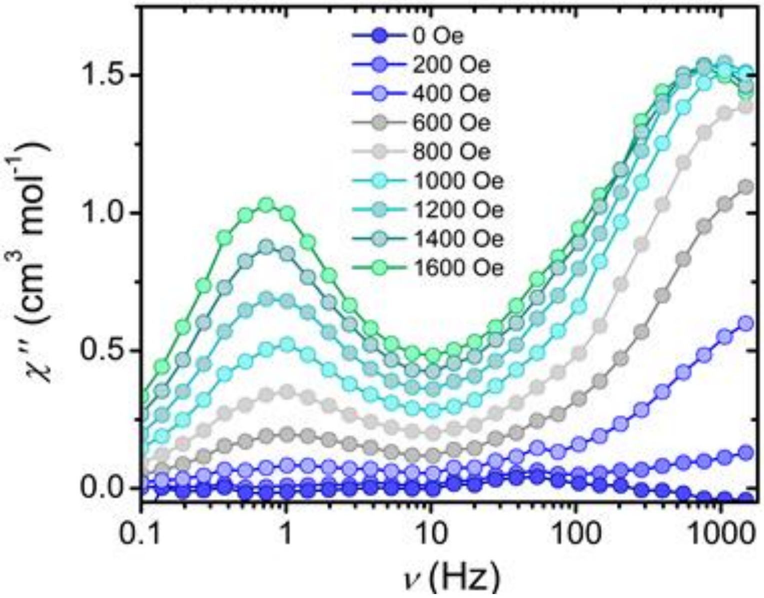

Figure 3.7 – Frequency dependence of the out-of-phase (χ'') magnetic susceptibility for complex **3.1** collected at 1.9 K and varying dc fields. Solid lines are guides for the eyes.

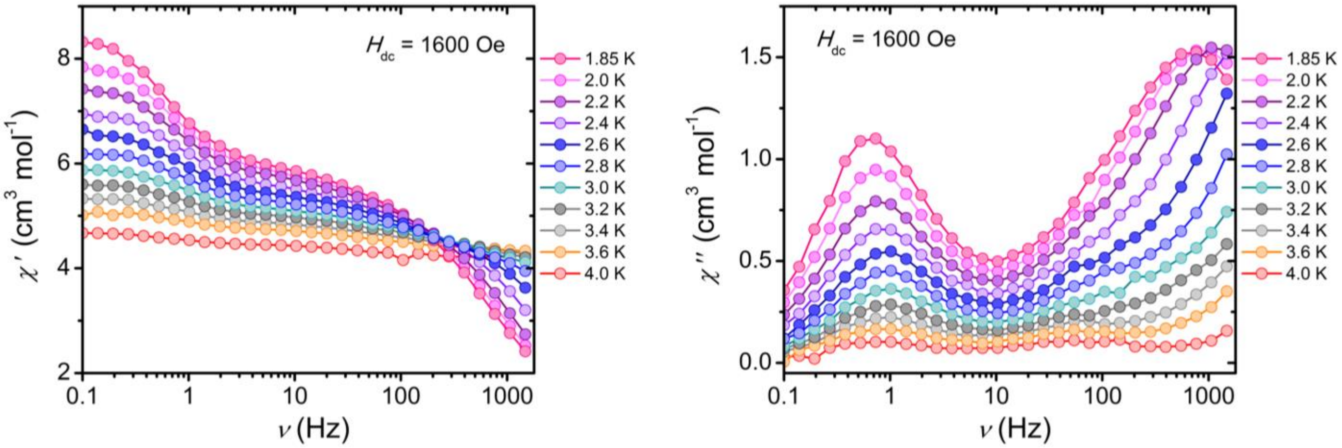

Figure 3.8 – Frequency dependence of the in-phase (χ') and out-of-phase (χ'') magnetic susceptibilities for **3.1**, collected under a 1600 Oe dc field and varying temperatures. Solid lines are guides for the eyes.

3.1.3 Summary of Findings

The Py_2F_2BTA ligand, which integrates attractive features of both terpy and bodipy, proves to be an ideal chelate for coordination chemistry, as explored here for the first time with Fe^{II} and Co^{II}. This, coupled with the carefully chosen azido bridge to promote FM interactions between metal ions, enables investigation of the magnetic exchange within these two isostructural model compounds. As projected, the use of azides as bridging ligands afforded complexes with large spin ground states due to the FM interactions, and as such these complexes represent ideal systems to probe the magnetic exchange between two octahedral M^{II} ions.

3.2 Experimental Procedures

General Procedures

The reagents NaN3, obtained from Acros Organics, anhydrous $FeCl_2$ and $CoCl_2$, obtained from Alfa Aesar, were used as received. Anhydrous solvents (acetonitrile, methanol and diethyl ether) were of reagent grade. The Py_2F_2BTA and Pm_2F_2BTA were synthesize following previously reported procedures.[40] IR spectra of solid samples were recorded on an Agilent Technologies Cary 630 FT-IR spectrometer.

Synthetic Procedure

Synthesis of $[Fe_2^{II}(\mu_{1,1}\text{-}N_3)_2(N_3)_2(Py_2F_2BTA)_2]$ (3.1): $FeCl_2$ (14 mg, 0.11 mmol) and NaN_3 (18 mg, 0.28 mmol) were dissolved and stirred in methanol (10 mL) then combined with Py_2F_2BTA (30 mg, 0.11 mmol) dissolved in acetonitrile (10 mL) to afford an opaque, green solution that was then stored at RT. After 48 hours, crystallization was completed, and black blocks were separated from the solution then washed with acetonitrile and diethyl ether. Yield = 78%. IR (neat cm^{-1}): 3108(*br*), 3060(*br*), 2965(*br*), 2059(*s*), 1633(*s*), 1598(*m*), 1571(*w*), 1492(*s*), 1467(*s*), 1425(*s*), 1331(*m*), 1284(*s*), 1269(*m*), 1212(*w*), 1190(*w*), 1158(*w*), 1131(*m*), 1161(*w*), 1107(*w*), 1081(*m*), 1049(*w*), 1036(*m*), 1015(*m*), 992(*w*), 972(*s*), 898(*w*), 846(*m*), 815(*m*), 788(*w*), 745(*s*), 713(*s*).

Preparation of $[Co_2^{II}(\mu_{1,1}\text{-}N_3)_2(N_3)_2(Py_2F_2BTA)_2]$ (3.2): The synthetic procedure followed is the same as that mentioned above using $CoCl_2$ (14 mg, 0.11 mmol), NaN_3 (18 mg, 0.28 mmol), methanol (15 mL), Py_2F_2BTA (30 mg, 0.11 mmol), and acetonitrile (15 mL). After 24 hours, crystallization was completed, and orange blocks were separated from the solution then washed with acetonitrile and diethyl ether. Yield = 85%. IR (neat cm^{-1}): 3060(*br*), 2943(*br*), 2833(*br*), 2060(*s*), 2050(*s*), 1635(*s*), 1599(*m*), 1572(*w*), 1496(*s*), 1465(*s*), 1427(*s*), 1376(*w*), 1334(*m*), 1287(*s*), 1267(*s*), 1158(*w*), 1129(*m*), 1107(*m*), 1083(*m*), 1027(*s*), 1016(*s*), 993(*m*), 973(*s*), 899(*w*), 850(*m*), 814(*m*), 746(*s*), 714(*s*), 670(*m*).

3.3 Crystallographic Information

Single Crystal X-Ray Diffraction Procedures

Crystallographic data as well as data collection and refinement of complex **3.1** and complex **3.2** are summarized in Table 3.4. The crystals were mounted on thin glass fibers using super glue. Prior to data collection crystals were cooled to 200(2) K. Data were collected on a Bruker AXS KAPPA single crystal diffractometer equipped with a sealed Mo tube source (wavelength 0.71073 Å) APEX II CCD detector. Raw data collection and processing were performed with APEX II software package from Bruker AXS. Systematic absences in the diffraction data and unit-cell parameters were consistent with monoclinic $P2_1/c$ (No.14) for complexes **3.1** and **32**. Solutions in the centrosymmetric space groups for complexes **3.1** and **3.2** yielded chemically reasonable and computationally stable results of refinement. The structures were solved by direct methods, completed with differential Fourier transformation, and refined with full-matrix least-squares procedures based on F^2. Refinement results for complexes **3.1** and **3.2** both suggested several non-merohedrally twinned domains. Careful examination of the original data frames and precession images for each complex confirmed the initial twinning assumption. In order to find the independent orientation matrices 307 reflections were collected for **3.1** and 604 reflections were collected for **3.2** in different sections of the Ewald sphere. The collected reflection data were then processed with CELL_NOW software[41–43] and two independent orientation matrices were obtained. Data sets were re-integrated with two independent matrices and treated for twinning absorption corrections and consecutive model refinement was preformed using HKL5 formatted reflection data file. Twining domain ratio coefficients (BASF) for complex **3.1** and **3.2** were allowed to refine freely and converged at a ratio of 0.504(1):0.496(1) and 0.511(2):0.489(2) for **3.1** and **3.2** respectively. For both complexes all non-hydrogen atoms were refined with anisotropic thermal motion approximation. All hydrogen atom positions were calculated based on the geometry of related non-hydrogen atoms, except for the N-H groups that were located using the Fourier difference maps and refined freely.

Table of Crystallographic Data

Table 3.4 – Crystallographic data for compounds **3.1**-**3.2**.

Crystal data	**3.1**	**3.2**
M_r	825.94	8.38.29
Space group	$P2_1/c$	$P2_1/c$
a, (Å)	11.9622(3)	11.8492(16)
b (Å)	10.2305(2)	10.2697(14)
c (Å)	14.0273(3)	13.9894(19)
α , (°)	90	90
β , (°)	107.128(1)	108.402(2)
γ , (°)	90	90
V, (Å^3)	1640.52(6)	1624.4(4)
Z	2	2
D_x, (Mg m^{-3})	1.672	1.714
μ, (mm^{-1})	0.97	1.11
Reflections measured	7704	4517
Independent Reflections	7704	4571
Reflections with $I>2\sigma(I)$	4536	3392
θ_{max}, θ_{min}, (°)	31.0, 1.8	25.2, 1.8
h	$-17\rightarrow16$	$-14\rightarrow13$
k	$0\rightarrow14$	$0\rightarrow12$
l	$0\rightarrow20$	$0\rightarrow16$
$R[F^2 > 2\sigma(F^2)]$	0.056	0.045
$wR(F^2)$	0.150	0.130
$\Delta\rho_{max}$, $\Delta\rho_{min}$ (e Å^{-3})	2.32, -0.63	0.61, -0.62

Powder Crystal X-Ray Diffraction Procedures

Bulk purity of the complexes described here was obtained on a Rigaku Ultima IV diffractometer and assessed by comparison of the obtained PXRD patterns with predicted patterns from single crystal data. The experimental PXRD patterns reported herein are found to convincingly match the predicted patterns

Overlay of Experimental PXRD and Predicted (through Mercury) SCXRD Patterns

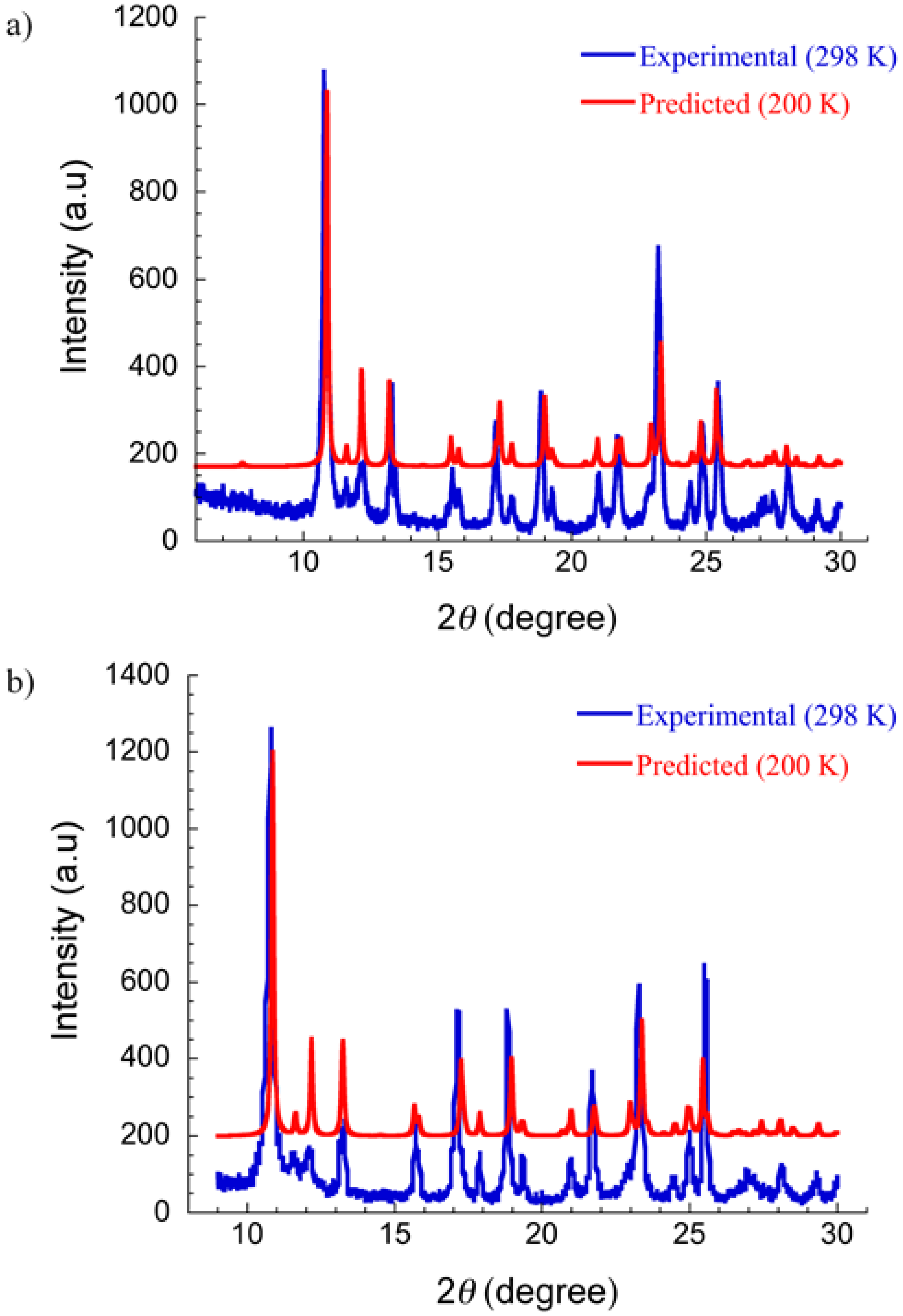

Figure 3.9 – PXRD pattern overlay of experimental microcrystalline samples of a) **3.1** and b) **3.2** with their predicted patterns.

3.4 Supramolecular Interactions

Table 3.5 – Potential short contacts in complexes 3.1 and 3.2.

3.1				**3.2**			
D–H···A	d(D–H), Å	d(H···A), Å	<(DHA), °	D–H···A	d(D–H), Å	d(H···A), Å	<(DHA), °
N4–H···N11	0.84(3)	2.09(4)	160	N4–H···N11	0.92(6)	2.01(6)	161
N5–H···N11	0.84(2)	2.05(3)	165	N5–H···N11	0.95(8)	1.91(8)	175
C3–H···F2	0.95	2.54	140	C3–H···F2	0.95	2.53	139
C4–H···N11	0.95	2.54	163	C4–H···N11	0.95	2.53	164
C9–H···N11	0.95	2.49	163	C9–H···N11	0.95	2.53	162
d(F1···N3C8C9C10C11C12 centroid), Å 3.169(3)				d(F1···N1C1C2C3C4C5 centroid), Å 3.003(4)			

3.5 References

1 P. A. Thornley, J. C. Starkey, R. Zibaseresht, M. I. J. Polson, J. L. Wikaira and R. M. Hartshorn, *J. Coord. Chem.*, 2011, **64**, 145

2 M. Yoshida, M. Kondo, T. Nakamura, K. Sakai and S. Masaoka, *Angew. Chemie - Int. Ed.*, 2014, **53**, 11519

3 X. Y. Wang, Z. M. Wang and S. Gao, *Chem. Commun.*, 2008, **2008**, 281

4 R. Bagai, K. A. Abboud and G. Christou, *Inorg. Chem.*, 2007, **46**, 5567

5 A. Escuer and G. Aromí, *Eur. J. Inorg. Chem.*, 2006, **2006**, 4721

6 J. Long, F. Habib, P. H. Lin, I. Korobkov, G. Enright, L. Ungur, W. Wernsdorfer, L. F. Chibotaru and M. Murugesu, *J. Am. Chem. Soc.*, 2011, **133**, 5319

7 U. Chakraborty, M. Modl, B. Mühldorf, M. Bodensteiner, S. Demeshko, N. J. C. Van Velzen, M. Scheer, S. Harder and R. Wolf, *Inorg. Chem.*, 2016, **55**, 3065

8 A. Escuer, J. Esteban, S. P. Perlepes, T. C. Stamatatos, *Coord. Chem. Rev.*, 2014, **275**, 87

9 Y. F. Zeng, X. Hu, F. C. Liu, X. H. Bu, *Chem. Soc. Rev.*, 2009, **38**, 469.

10 J A. Jana, S. Konar, K. Das, S. Ray, J. A. Golen, A. L. Rheingold, L. M. Carrella, E. Rentschler, T. K. Mondal, S. K. Kar, *Polyhedron*, 2012, **38**, 258

11 J. Yuan, W. B. Shi and H. Z. Kou, *Transit. Met. Chem.*, 2015, **40**, 807

12 S. Demeshko, G. Leibeling, W. Maringgele, F. Meyer, C. Mennerich, H. H. Klauss and H. Pritzkow, *Inorg. Chem.*, 2005, **44**, 519

13 F. Meyer, P. Kircher, H. Pritzkow, *Chem. Commun.*, 2003, **0**, 774

14 X. H. Zhao,L. D. Deng, Y. Zhou, D. Shao, D. Q. Wu, X. Q. Wei, X. Y. Wang, *Inorg. Chem.*, 2017, **56**, 8058

15 T. F, Liu, D. Fu, S. Gao, Y. Z. Zhang, H. L. Sun, G. Su, Y. J. liu, *J. Am. Chem. Soc.*, 2003, **2**, 13976

16 J. Liu, M. Qu, M.Rouzière, X. M. Zhang, R. A. Clérac, *Inorg. Chem.*, 2014, **53**, 7870

17 C. Adhikary, S. Koner, *Coord. Chem. Rev.*, 2010, **254,** 2933

18 E. Ruiz, J. Cano, S. Alvarez, P. Alemany, *J. Am. Chem. Soc.*, 1998, **120,** 11122

19 G. Brunet, F. Habib, C. Cook, T. Pathmalingam, F. Loiseau, I Korobkov, T. J. Buchell, A. M. Beauchemin, M. Murugesu, *Chem. Commun.*, 2012, **48,** 1287

20 J J. Ribas, A. Escuer, M. Monfort, R. Vicente, R. Cortés, L. Lezama, T. Rojo, *Coord. Chem. Rev.*, 1999, **193–195,** 1027

21 A. K. Boudalis, J. M. Clemente-Juan, F. Dahan, J. P., Tuchagues, *Inorg. Chem.*, 2004, **43,**

1574
22 A. K. Boudalis, J. M. Clemente-Juan, F. Dahan, J. P., Tuchagues, *Inorg. Chem.*, 2004, **43,** 1574
23 J. M. Clemente-Juan, C. Mackiewicz, M. Verelst, F. Dahan, A Bousseksou, Y. Sanakis, J. P. Tuchagues, *Inorg. Chem.*, 2002 **41,** 1478
24 Y. F. Deng, T. Han, N. Hayashi, H. Kageyama, Y. Z. Zheng, *Dalton Trans.*, 2017, **46,** 1449
25 J. W. Shin, S. R. Rowthu, M. Y. Hyun, Y. J. Song, C. Kim, B. G. Kim, K. S. Min, *Dalt. Trans.*, 2011, **40,** 5762
26 S. Naiya, M. G. B. Drew, C. Diaz, J. Ribas, A. Ghosh, *Eur. J. Inorg. Chem.*, 2011, **2011,** 4993
27 S. Schmidt, D. Prodius, G. Novitchi, V. Mereacre, G. E. Kostakis, A. K. Powell, *Chem. Commun.*, 2012, **48,** 9825
28 G. De Munno, T. Poerio, G. Viau, M. Julve, F. Lloret, *Angew. Chem. Int. Ed. EngI.*, 1997, **36**, 1459
29 D. Casanova, M. Llunell, P. Alemany, S. Alvarez, *Chem. Eur. J.*, 2005, **11,** 1479
30 N. F. Chilton, R. P. Anderson, L. D. Turner, A. Soncini, K. S. Murray, *J. Comput. Chem.*, 2013 **34,** 1164
31 Y. L. Wang, L. Chen, C. M. Liu, Y. Q. Zhang, S. G. Yun, Q. Y. Liu, *Inorg. Chem.*, 2015, **54,** 11362
32 J. Vallejo, I. Castro, R. Ruiz-García, J. Cano, M. Julve, F. Lloret, G. De Munno, W. Wernsdorfer, E. Pardo, *J. Am. Chem. Soc.*, 2012, **134,** 15704
33 G. Brunet, D. A. Safin, J. Jover, E. Ruiz, M. Murugesu, *J. Mater. Chem.*, 2017, **5**, 835
34 R. Boča, J. Miklovič, J. Titiš, *Inorg. Chem.*, 2014, **53,** 2367
35 B. H. Wu, M. J. Huang, C. C. Lai, C. H. Cheng, I. C. Chen, *Inorg. Chem.*, 2018, **57**, 4448
36 D. Lomjanský, J. Moncol, C. Rajnák, J. Titiš, R. Boča, *Chem. Commun.*, 2017, **53**, 6930
37 F. Habib, I. Korobkov, M. Murugesu, *Dalton Trans.*, 2015, **44,** 6368
38 C. M. Liu, D. Q. Zhang, D. B. Zhu, *Chem. Commun.*, 2016, **52,** 4804
39 S S. Mossin, B. L. Tran, D. Adhikari, M. K. Szilagyi, K. Meyer, D. J. Mindiola, *J. Am. Chem. Soc.*, 2012, **134,** 13651
40 M. Yousaf, N. J. Yutronkie, R. Castañeda, J. A. Klein and J. Brusso, *New J. Chem.*, 2017, **41**, 12218
41 G. M. Sheldrick, *Acta Crystallogr. Sect. A Found. Crystallogr.*, 2008, **64**, 112
42 G. M. Sheldrick, *Acta Crystallogr. Sect. C Struct. Chem.*, 2015, **71**, 3
43 Bruker, *APEX2*, 2012, Bruker AXS Inc., Madison, Wisconsin, USA

CHAPTER 4

4.0 Thiocyanate Functionalization in Terpy-type Complexes of First Row Transition Metals

Owing to the rich coordination chemistry made available through the use of azide ligands (Chapter 3), we next sought to employ of the ambivalent thiocyanate (NCS) ligand, which has a similarly rich set of binding modes, for the preparation of magnetically interesting materials. The NCS ligand commonly binds in an end-on (EO) or end-to-end (EE) fashion, forming mononuclear and polynuclear constructs.[1] Dinuclear structures bridged through NCS ions are, however, less efficient at transmitting magnetic interactions than their azido derivatives, leading to much weaker antiferromagnetic and ferromagnetic interactions.[2–4]

On the other hand, mononuclear five-coordinate 3d metal complexes involving EO bound NCS ions and a terpy-type framework have been shown to display attractive magnetic phenomena, including intermolecular antiferromagnetic interactions, slow magnetic relaxation pathways as well as spin crossover.[5–9] With respect to the choice of 3d metal, Fe^{II} and Co^{II} are often employed for their highly anisotropic ground state and their unquenched first order orbital angular momentum.[6] When employing tridentate ligands and NCS anions with these metal salts, octahedral structures are most commonly obtained. Octahedral Fe^{II} structures with double EO bound NCS ligands being especially prone to hosting spin crossover behaviours.[10,11] Interestingly, five-coordinate metal complexes which feature double EO bound NCS anions are relatively uncommon for Co^{II}. In the case of Fe^{II}, only two examples of this type of structure have been reported, both being multinuclear in nature, highlighting the rarity of this motif in coordination chemistry.[12,13]

We have therefore focused our attention on the development of mononuclear Fe^{II} and Co^{II} complexes by taking advantage of the rigid tridentate framework of the BTA ligand. By employing Py_2F_2BTA with thiocyanate counterions, we anticipate generating high spin Fe^{II} and Co^{II}

complexes, which have been recognized to have unquenched first order orbital angular momentum, which is an important source of anisotropy necessary for SMMs. To that end, we report herein the synthesis and structural properties of two novel mononuclear constructs featuring double EO bound thiocyanate counterions; $[Fe^{II}(NCS)_2(Py_2F_2BTA)]\cdot MeCN$ **4.1**, and its isostructural analogue $[Co^{II}(NCS)_2(Py_2F_2BTA)]\cdot MeCN$ **4.2**. Due to time constraints, however, the magnetic measurements of these complexes have not yet been obtained.

4.1 Synthesis and Structural Properties of Mononuclear [M^{II}(NCS)$_2$BTA] Complexes

The two compounds reported here were prepared using similar methodology, with the key difference being in the preparation of the metal salts used. For example, by stirring a solution of $FeCl_2$ and excess KSCN in an MeCN solution, the corresponding $Fe(NCS)_2$ metal salt can be formed *in situ*. Layering this atop a stirred solution of the Py_2F_2BTA ligand in dichloromethane (DCM), then placing the layered solutions in a diethyl ether bath leads to the formation of a green solution over time. After a few days the solution turns red, indicating the completion of crystallization of $[Fe^{II}(NCS)_2(Py_2F_2BTA)]\cdot MeCN$ (**4.1**), which forms as green needles suitable for SCXRD analysis. Alternatively, a solution of commercially obtained $Co(NCS)_2$ in MeCN can be layered upon a DCM solution containing Py_2F_2BTA and then placed in a diethyl ether bath to obtain a green solution. After a few days, the color of the reaction remains green and dark red needles of $[Co^{II}(NCS)_2(Py_2F_2BTA)]\cdot MeCN$ (**4.2**) suitable for SCXRD can be isolated. For both compounds, bulk purity and composition of the as synthesized products have been confirmed though SXCRD and PXRD (see below). Single crystal analysis reveals that **4.1** and **4.2** crystallize in the monoclinic $P2_1/n$ space group (Figure 4.1 and Table 4.1), with an asymmetric unit featuring either Fe^{II} or Co^{II} coordinated in *mer* fashion to a neutral molecule of the Py_2F_2BTA ligand. Completing the coordination environment about the metal centres are two NCS counterions bound through their nitrogen atoms. An uncoordinated MeCN molecule can be found in the crystal lattice of each structure. As such, the metal centres adopt a five-coordinate arrangement, resulting in coordination geometries best described as an admixture between trigonal bipyramidal and square planar, as determined using the SHAPE[14] software (Table 4.2 and Figure 4.2).

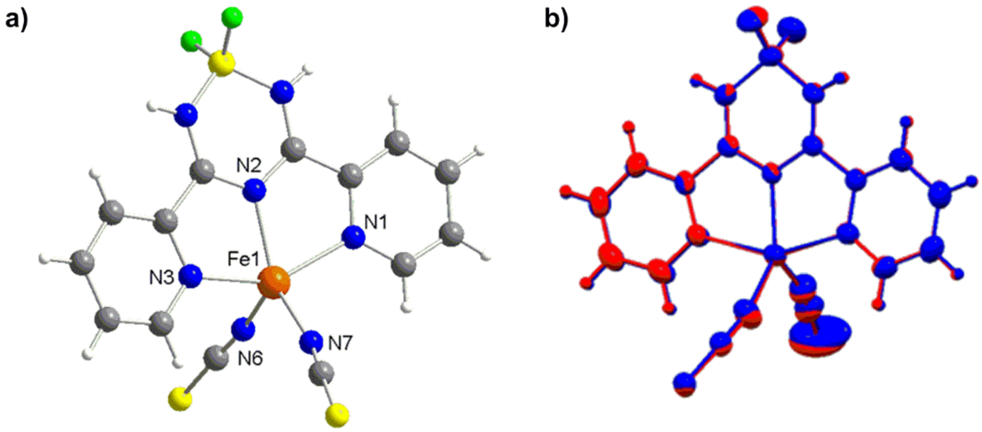

Figure 4.1 – a) Molecular structure of [Fe^{II}(NCS)$_2$(Py$_2$F$_2$BTA)]·MeCN, which includes labelling for key atoms within the molecular unit. Acetonitrile is omitted for clarity. b) Overlay of complexes [Fe^{II}(NCS)$_2$(Py$_2$F$_2$BTA)]·MeCN (**4.1**, red) and [Co^{II}(NCS)$_2$(Py$_2$F$_2$BTA)]·MeCN (**4.2**, blue) using 50% thermal ellipsoids.

Table 4.1 – Selected bond lengths (Å) for complexes **4.1** and **4.2**.

Distance	**4.1**	**4.2**
M1–N1	2.166(3)	2.152(3)
M1–N2	2.088(3)	2.002(3)
M1–N3	2.153(3)	2.145(3)
M1–N6	1.990(4)	1.971(3)
M1–N7	2.016(3)	1.977(3)

Table 4.2 – Results from Shape analysis. Ideal geometry is a zero value, distortion from this geometry increases the value of the continuous shape measures.

	PP-5	vOC-5	TBPY-5	SPY-5	JTBPY-5
4.1	29.05	4.64	3.50	2.57	5.87
4.2	30.32	4.53	2.61	2.74	4.52

PP-5: D_{5h}, Pentagon; vOC-5: C_{4v}, Vacant octahedron (Johnson square pyramid J1); TBPY-5: D_{3h}, Trigonal bipyramid; SPY-5: C_{4v}, Square pyramid; JTBPY-5: D_{3h}, Johnson trigonal bipyramid (J12).

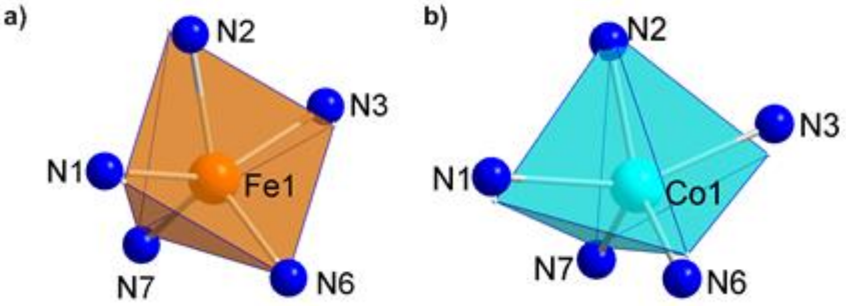

Figure 4.2 Deviation from ideal geometrical environments about the metal ions in complexes a) **4.1** and b) **4.2**.

The two complexes have further similarities upon considering the supramolecular interactions, in which a number of short contacts exist between the terminal sulfur atom of the NCS ligands, resulting in one N–H···S, three C–H···S and two S···π interactions in addition to a π···π interaction between pyridyl rings, one N–H···N, one C–H···S, and one C–H···N short contacts in each structure. These are visualized in Figure 4.3, which shows compounds **4.1** and **4.2** packing in brick-like arrangements.

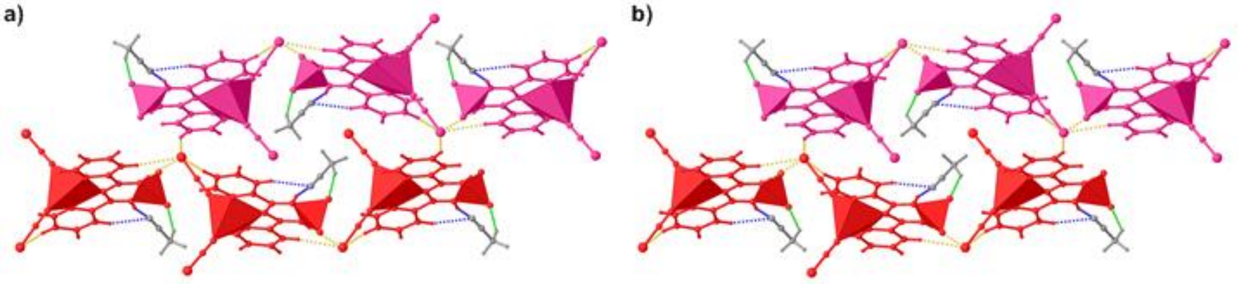

Figure 4.3 – Crystal packing diagram of complex a) **4.1** and b) **4.2**. Hydrogen bonds are denoted as green (F···H–A), yellow (S···H–A), and blue (N···H–A) dotted lines. Polyhedra added to show orientation of units.

The terpy analogue of compound **4.2** is a single ion magnet known to display magnetic relaxation through multiple pathways.[6] Comparison of the [Co^{II}(NCS)$_2$terpy] with **4.2** reveals that, while the tridentate ligands reside in the same planes, the EO bound NCS ligands are oriented differently (Figure 4.4). This results in the terpy analogue favouring the trigonal bipyramidal geometry more strongly than compound **4.2**. Additionally, although both compounds have π···π interactions between pyridyl rings in the solid state, the distance between centroids is shorter in the terpy analogue by 0.27 Å.

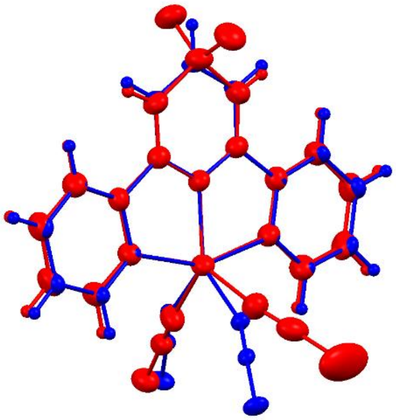

Figure 4.4 – Overlay of complexes **4.2** (red) and [$Co^{II}(NCS)_2$(terpy)] (blue) using 50% thermal ellipsoids. The acetonitrile molecule in **4.2** is omitted for clarity.

4.2 Summary of Findings

Through the reaction of the Py_2F_2BTA ligand with the triatomic thiocyanate ligand, different coordination structures are obtained than when using azides, yielding mononuclear compounds as opposed to dimeric constructs. Although magnetic measurements have not yet been obtained for the presented complexes, it is expected, through the analysis of similar coordination compounds, that interesting magnetic properties arise from these systems.

4.3 Experimental Procedures

General Procedures

The reagents KSCN, obtained from VWR, anhydrous $FeCl_2$ and $Co(NCS)_2$, obtained from Alfa Aesar, were used as received. Anhydrous solvents (MeCN, DCM and diethyl ether) were of reagent grade. The Py_2F_2BTA and Pm_2F_2BTA were synthesize following previously reported procedures.[15] IR spectra of solid samples were recorded on an Agilent Technologies Cary 630 FT-IR spectrometer.

Synthetic procedures

Synthesis of [Fe^{II}(NCS)$_2$(Py$_2$F$_2$BTA)]·MeCN (4.1): Py$_2$F$_2$BTA (68 mg, 0.25 mmol) was dissolved in acetonitrile (10 mL) then layered upon a solution of FeCl$_2$ (32 mg, 0.25 mmol) and KSCN (59 mg, 0.60 mmol) that was stirred and dissolved in dichloromethane (10 mL). The mixture was then placed in a diethyl ether bath. The result is a green solution which turned red after a few days once crystallization was completed. Green needles were then separated from the solution then washed with acetonitrile and diethyl ether. Yield = 84%. IR (neat cm^{-1}): 3194(*br*), 3063(*br*), 2951(*br*), 2259(*w*), 2088(*s*), 2051(*s*), 1643(*w*), 1598(*s*), 1560(*s*), 1492(*s*), 1467(*m*), 1431(*s*), 1389(*m*), 1367(*w*), 1331(*w*), 1289(*w*), 1231(*m*), 1152(*w*), 1113(*w*), 1090(*m*), 1048(*w*), 1019(*m*), 971(*m*), 778(*w*), 755(*s*), 711(*s*).

Preparation of [Co^{II}(NCS)$_2$(Py$_2$F$_2$BTA)]·MeCN (4.2): Co(NCS)$_2$ (33 mg, 0.25 mmol) was dissolved in acetonitrile (10 mL) then layered upon a solution of Py$_2$F$_2$BTA (68 mg, 0.25 mmol) that was dissolved in dichloromethane (10 mL). The mixture was then placed in a diethyl ether bath. The result is a green solution which yields red needles after a few days. Once crystallization was completed these red needles were then separated from the solution then washed with acetonitrile and diethyl ether. Yield = 80%. IR (neat cm^{-1}): 3193(*br*), 2090(*s*), 2059(*s*), 1643(*s*), 1598(*m*), 1493(*w*), 1466(*s*), 1432(*s*), 1330(*s*), 1288(*w*), 1153(*m*), 1112(*s*), 1091(*m*), 1048(*m*), 1015(*s*), 979(*s*), 816(*m*), 788(*m*), 755(*s*), 712(*s*).

4.4 Crystallographic Information

Single Crystal X-Ray Diffraction Procedures

Prior to data collection, crystals were cooled to 200(2) K. Data was collected on a Bruker APEX II CCD detector with a sealed Mo tube source (wavelength 0.71073 Å). Raw data collection and processing were performed with the APEX II and SAINT software packages from BRUKER AXS.[16] The SHELXT and SHELXL programs were used to solve and refine the structures.[17] For both complexes all non-hydrogen atoms were refined with anisotropic thermal motion approximation. All hydrogen atom positions were calculated based on the geometry of related non-hydrogen atoms, except for the N-H groups that were located using the Fourier difference maps and refined freely.

Table of Crystallographic Data

Table 4.3 – Crystallographic data for compounds **4.1-4.2**.

Crystal data	4.1	4.2
FW	486.12	489.20
Space group	$P2_1/n$	$P2_1/n$
a, (Å)	7.8758(13)	7.991(4)
b (Å)	19.288(3)	19.258(9)
c (Å)	14.285(2)	14.151(6)
α , (°)	90	90
β , (°)	104.366(5)	104.159(7)
γ , (°)	90	90
V, (Å^3)	2102.1(5)	2111.3(16)
Z	4	4
D_x, (Mg m^{-3})	1.536	1.539
μ, (mm^{-1})	0.95	1.05
Reflections measured	27378	18349
Independent Reflections	4467	5046
Reflections with $I>2\sigma(I)$	2531	2745
R_{int}	0.116	0.076
θ_{max}, θ_{min}, (°)	26.7, 1.8	28.7, 1.8
h	$-9\rightarrow9$	$-9\rightarrow10$
k	$-24\rightarrow24$	$-25\rightarrow25$
l	$-16\rightarrow18$	$-18\rightarrow19$
$R[F^2 > 2\sigma(F^2)]$	0.049	0.051
$wR(F^2)$	0.129	0.124
$\Delta\rho_{max}$, $\Delta\rho_{min}$ (e Å^{-3})	0.45, -0.52	0.43, -0.38

Powder Crystal X-Ray Diffraction Procedures

Bulk purity of the complexes described here was obtained on a Rigaku Ultima IV diffractometer and assessed by comparison of the obtained PXRD patterns with predicted patterns from single crystal data. The experimental PXRD patterns reported herein are found to convincingly match the predicted patterns.

Overlay of Experimental PXRD and Predicted (through Mercury) SCXRD Patterns

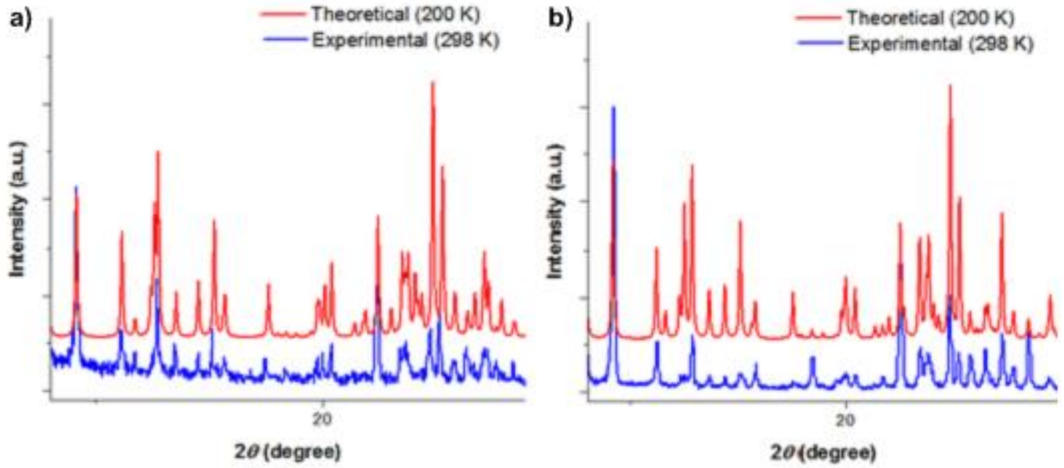

Figure 4.5 – PXRD pattern overlay of experimental microcrystalline samples of a) **4.1** and b) **4.2** with their predicted patterns (using the Mercury software).

4.5 Supramolecular Interactions

Table 4.3 – Potential short contacts in complexes **4.1** and **4.2**.

4.1				**4.2**			
D–H···A	d(D–H), Å	d(H···A), Å	<(DHA), °	D–H···A	d(D–H), Å	d(H···A), Å	<(DHA), °
N4–H···S2	0.85(3)	2.57(3)	163(3)	N4–H···S2	0.85(3)	2.60(4)	157(3)
N5–H···N1S	0.87(3)	2.19(3)	165(3)	N5–H···N1S	0.86(3)	2.20(3)	163(3)
C2S–H···F2	0.98	2.28	158	C2S–H···F2	0.98	2.41	139
C2–H···S2	0.95	2.82	148	C3–H···S2	0.95	2.81	148
C3–H···S2	0.95	2.82	166	C4–H···S2	0.95	2.86	166
C9–H···N1S	0.95	2.48	164	C9–H···N1S	0.95	2.52	164
C11–H···S2	0.95	2.84	151	C11–H···S2	0.95	2.86	150
d(S1···B1N4C6N2C7N5 centroid), Å 3.323(3)				d(S1···B1N4C6N2C7N5 centroid), Å 3.305(3)			
d(S2··· B1N4C6N2C7N5 centroid), Å 3.272(2)				d(S2··· B1N4C6N2C7N5 centroid), Å 3.299(2)			
d(C1C2C3C4C5N1··· C8C9C10C11C12N3 centroid), Å 3.925(2)				d(C1C2C3C4C5N1··· C8C9C10C11C12N3 centroid), Å 3.932(2)			

4.6 References

1 S. Suckert, L. S. Germann, R. E. Dinnebier, J. Werner and C. Näther, *Crystals*, 2016, **6**, 38

2 J. Palion-Gazda, B. Machura, F. Lloret and M. Julve, *Cryst. Growth Des.*, 2015, **15**, 2380

3 R. Boča and R. Herchel, *Coord. Chem. Rev.*, 2010, **254**, 2973

4 B. Machura, A. Świtlicka, J. Palion and R. Kruszynski, *Struct. Chem.*, 2013, **24**, 89

5 T. Jurca, A. Farghal, P. H. Lin, I. Korobkov, M. Murugesu and D. S. Richeson, *J. Am. Chem. Soc.*, 2011, **133**, 15814

6 F. Habib, O. R. Luca, V. Vieru, M. Shiddiq, I. Korobkov, S. I. Gorelsky, M. K. Takase, L. F. Chibotaru, S. Hill, R. H. Crabtree and M. Murugesu, *Angew. Chem. Int. Ed.*, 2013, **52**, 11290

7 B. MacHura, J. Palion, J. Mroziński, B. Kalińska, M. Amini, M. M. Najafpour and R. Kruszynski, *Polyhedron*, 2013, **53**, 132

8 R. Kapoor, A. Kataria, P. Venugopalan, P. Kapoor, G. Hundal and M. Corbella, *Eur. J. Inorg. Chem.*, 2005, **2005**, 3884

9 D. Gatteschi, C. A. Ghilardi, A. Orlandini and L. Sacconi, *Inorg. Chem.*, 1978, **17**, 3023

10 R. J. Wei, J. Tao, R. Bin Huang and L. S. Zheng, *Inorg. Chem.*, 2011, **50**, 8553

11 Q. L. Liu, L. J. Yang, Y. H. Luo, W. Wang, Y. Ling and B. W. Sun, *Inorg. Nano-Met.* 2016, **46**, 1

12 G. Psomas, N. Bréfuel, F. Dahan and J. P. Tuchagues, *Inorg. Chem.*, 2004, **43**, 4590

13 J. Klingele and D. Kaase, *CSD Communication*, 2016, DOI: 10.5517/ccdc.csd.cc14fkhm

14 D. Casanova, M. Llunell, P. Alemany and S. Alvarez, *Chem. Eur. J.*, 2005, **11**, 1479

15 M. Yousaf, N. J. Yutronkie, R. Castañeda, J. A. Klein and J. Brusso, *New J. Chem.*, 2017, **41**, 12218

16 G. M. Sheldrick, *Acta Crystallogr. Sect. A Found. Crystallogr.*, 2008, **64**, 112

17 G. M. Sheldrick, *Acta Crystallogr. Sect. C Struct. Chem.*, 2015, **71**, 3

CHAPTER 5

5.0 Mechanisms of Luminescence

The emission of light is a physical phenomenon that occurs as a response to an external stress, which can take the form of thermal, electrical, or chemical energy. The general term for this phenomenon is dubbed luminescence; however, depending on the nature of the external stimulus, it can be subdivided into different designations. These include bioluminescence, chemiluminescence, electroluminescence, photoluminescence, radioluminescence, sonoluminescence, thermoluminescence, and triboluminescence; each are due, respectively, to enzymatic reactions, chemical reactions, electrical input, photons, ionization, sound waves, temperature, and mechanical efforts.[1] Among these, photoluminescence is the most well understood process. Substances which are capable of photoluminescence are termed fluorophores.

Electrons fill up molecular orbitals according to the Boltzmann distribution, with the population of higher electronic levels being negligibly populated compared with that of the ground state at room temperature. When subjected to excitation, promotion of electrons from the ground state S_0, to an excited state S_n may occur. The excited state is typically an unstable and transient species, and thus return of the electrons to their ground state energy ensues through either radiative or non-radiative decay mechanisms.[2]

Non-radiative decay mechanisms take place without emission of photons, and these consist mainly of three processes: vibrational relaxation (a process in which the excited molecule transfers vibrational energy through collisions to surrounding molecules), internal conversion (a process in which transitions between two electronic states of the same multiplicity occurs), and intersystem crossing (a spin forbidden process where a transition between two electronic states of different multiplicities occurs). For non-gaseous compounds, radiative decay is associated with the emission of photons through either fluorescence or phosphorescence. Fluorescence involves the transition of an electron from the lowest excited singlet state to the ground state. Phosphorescence occurs as a spin forbidden transition from the triple lowest excited state to the singlet ground state, and therefore occurs on a much slower timescale when compared to fluorescence. In both cases, a molecule excited to an S_n state would first decay to the lowest excited state, S_1, through internal conversion before radiating to the ground state.[2] A Jablonski diagram best aids in visualizing the described phenomena and is provided below (Figure 5.1).

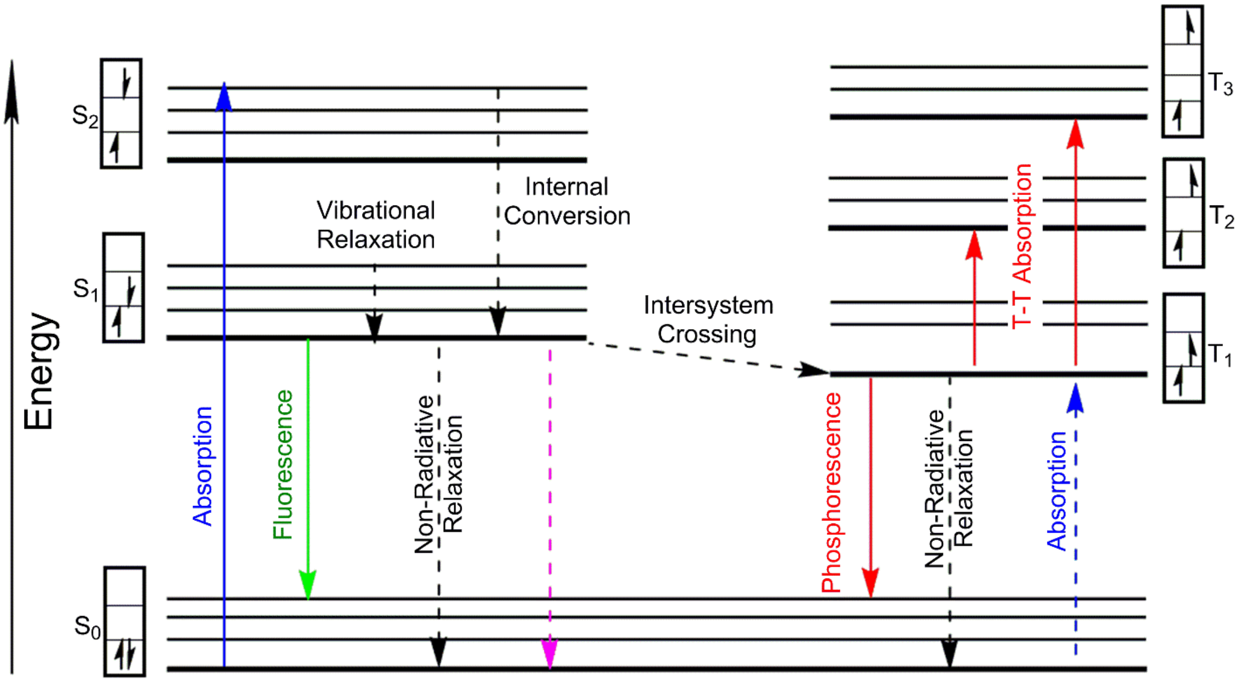

Figure 5.1 – Jablonski energy level diagram depicting the principal luminescence processes (left: singlet (*S*) manifold, right: triplet (*T*) manifold). Radiative processes are shown as full arrows and non-radiative processes are shown as dotted arrows. This figure was recreated from literature.[1]

Deactivation of an excited state is possible *via* quenching processes. Collisional quenching is a bimolecular process that occurs when a substance, able to receive the excess energy possessed by the excited state, collides with the fluorophore; static quenching occurs when a non-fluorescent entity attaches to the fluorophore, and self-quenching can occur when a fluorophore interacts with another molecule of itself, absorbing the emission of its neighboring partner.[1,2]

5.1 Luminescent Zinc (II) and Cadmium (II) Metal Complexes

Luminescent metal complexes are key materials for several applications such as lighting, molecular probes and switches, lasers and imaging.[3,4] Although the properties of these compounds show great potential for grabbing significant shares in their respective markets, the development strategies of these technologies are still evolving. For example, the major complication which currently limits the growth of the light emitting displays employing metal complexes in their fabrication is the availability of rare earth metals, especially iridium.[5] To address such concerns, the development of luminescent metal complexes which come from more sustainable sources has thus become an emerging area of research.

Many examples of luminescent metal compounds based on precious and rare earth metals exist; elements from the platinum group have received particular attention in this field. The expensive and environmentally problematic nature of these compounds have, however, driven research towards less traditional, but more sustainable metal sources.[6] The use of metal ions housing a d^{10} configuration, such as the group 12 metal dications Zn(II) and Cd(II), has recently risen as a strategic means for the development of luminescent compounds. Zinc compounds are fairly non-toxic to humans due to their relative non-reactivity and abundance in the human body, in which their main role is to provide structural properties to different proteins.[4] In contrast, compounds of cadmium have a known harmful toxicity profile. This, in combination with the low cost of zinc salts, has seen Zn(II) compounds as the more prolifically investigated metal cation among group 12 elements.

The unique properties of Zn(II) and Cd(II) compounds can be harnessed for the development of highly emissive materials. Due to their closed shell electronic configurations, the metal centres are quite insensitive to redox processes, therefore d-d transitions are not expected to occur. The possibilities for quenching the luminescent excited state by thermal equilibration or energy transfer are thus reduced due to this lack of low-lying metal-centred energy levels. Therefore, the emission in these d^{10} complexes originates from the associated organic ligand, with the lowest energy excited states being typically ligand-centred (LC) and/or ligand to ligand charge transfer (LLCT) in nature. There have also been several reports of ligand-to-metal charge transfer (LMCT) states involving the low-lying empty *s* or *p* orbitals of the metal centre; however, it has been advocated that in most of these compounds, the transition is more accurately assigned as an admixture of LLCT and LMCT.[3,7] Modulation of the associated ligands in Zn(II) and Cd(II) complexes can therefore be used for the finetuning of the resulting photophysical properties.

Upon complexation of an organic chromophore to group 12 metals, luminescence often increases due to the rigidification of the ligand. Vibrationally and rotationally coupled internal conversions are the major non-radiative decay pathways, more so with compounds possessing increasing degrees of freedom. Once ligated, the number of rotational degrees of freedom which can contribute to the non-radiative decays of the excited state of a molecule are reduced, which in turn decreases the rate of internal conversion, increasing fluorescence.[3,7] In the solid state, the non-radiative decay offered by bond vibration/rotation can be further impeded through tighter molecular packing *via* a process known as aggregation induced emission. This holds true so long as aggregation does not introduce competing intermolecular quenching pathways.[8,9]

Another attractive feature of Zn(II) and Cd(II) metal complexes is that they can assume coordination geometries which range from tetrahedral to octahedral, increasing the diversity of possible constructs. The structures that are formed with these ions are highly dependent upon the identity of the ligand, resulting in the synthesis of monomeric, multinuclear, and polymeric (2D and 3D) species.[3,10]

The investigation into luminescent zinc and cadmium complexes has led to several applications in science and technology. Zn(II) complexes have been used in the fabrication of photovoltaic devices such as organic light emitting displays, in light emitting electrochemical cells, in luminescent solar concentrators,[4,5,7] in the ratiometric fluorescent recognition of histidine,[11] as well as in the biological imaging of Zn(II) ions[7]. Due to cadmium being an environmental pollutant, there is a growing interest in the development of selective Cd(II) fluorescent indicators.[7]

In light of the attractive features of Zn(II) and Cd(II) complexes, we sought to explore the luminescent properties of BTA based complexes. Through modulation of the coordination environment, the emission energy and intensity, stability of the complex, as well as changes in structure and bonding are expected.[3,7] This has been the motivation behind the work presented within this chapter. In particular, we sought to employ the chromophoric BTA ligands Py_2F_2BTA and Pm_2F_2BTA for the construction of group 12 based emissive materials. In general, it has been observed that upon complexation of a chromophoric ligand to Zn(II) or Cd(II) salts, an increase in emission intensity is observed.[3] This is typically attributed to the decrease in vibrational and rotational degrees of freedom of the ligand upon complexation to the metal centre. Upon coordination to Zn(II) or Cd(II) metal salts, the emission profile of a fluorophoric ligand typically experiences some measure of redshift due to a stabilization of the excited state; the degree of redshift is usually smaller if cadmium is used for acquiring the spectrum.[3,7,12,13] Further redshift is normally observed going from solution to solid state for these complexes, a phenomenon which is caused by the introduction of intermolecular interactions such as hydrogen bonding or π-stacking, which effectively decreases the energy gap.[14–16] Also, it has been well documented that the choice of ligands used to complete the coordination environment in zinc or cadmium constructs has the ability to shift the emission spectra to a significant degree.[13–16]

5.2.1 Synthesis and Structural Properties of Boratriazine-Based Zinc (II) and Cadmium (II) Complexes

In an effort to explore the luminescent properties of our boratriazine systems upon coordination to group 12 metals, we herein report the preparation of a series of Zn(II) and Cd(II) complexes, namely, $[Zn^{II}Cl_2(Py_2F_2BTA)]$ (**5.1**), $[Zn^{II}Cl_2(Pm_2F_2BTA)]\cdot MeOH$ (**5.2**), $[Cd^{II}Cl_2(Py_2F_2BTA)(MeOH)]$ (**5.3**), $[Cd^{II}Cl_2(Pm_2F_2BTA)]\cdot MeOH$ (**5.4**), $[Zn^{II}(NCS)_2(Py_2F_2BTA)]\bullet MeCN$ (**5.5**), and $[Cd^{II}(Py_2F_2BTA)_2]2(ClO_4)$ (**5.6**). In addition, the emissive properties of a crystalline material (termed here **A1**) for which X-ray data was not obtained is discussed. Through comparison of the syntheses and IR signatures of compounds **5.5** and **A1**, it is likely that **A1** is the pyrimidyl analogue of **5.5** (Figure 5.2). Interestingly, all of these compounds crystallize from the same 1:1 MeCN:MeOH solvent system, although the crystallization methods vary between complexes.

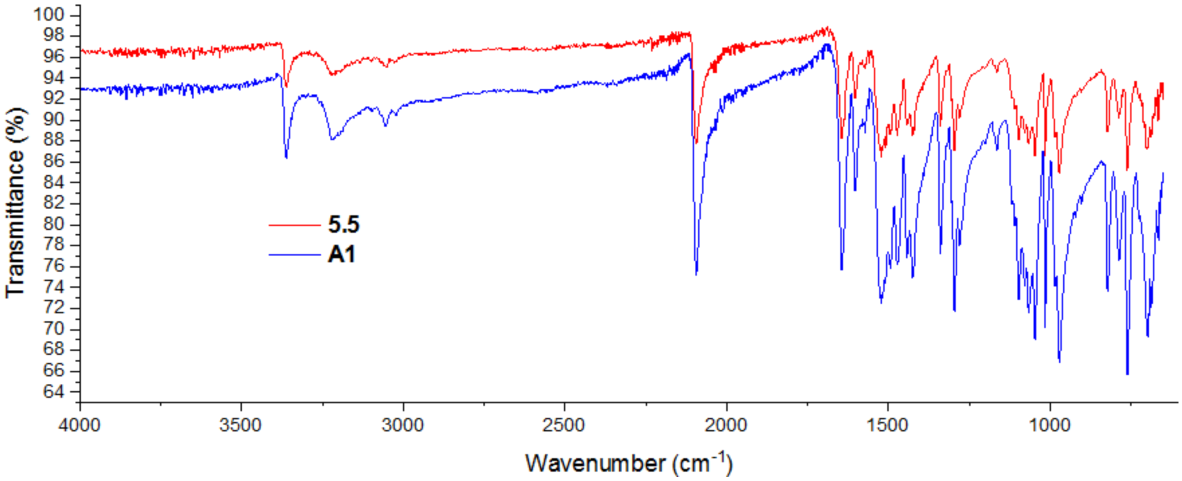

Figure 5.2 – Overlay of the infrared spectra of both compounds **5.5** (red) and **A1** (blue).

Compounds **5.1** and **5.2** (Figure 5.3) can be achieved by reacting $ZnCl_2$ and the corresponding BTA ligand in a MeCN:MeOH solution. After stirring a few minutes, the solution is filtered and capped, affording clear plate-shaped crystalline material suitable for SCXRD analysis after 12 hours. Crystals of **5.1** and **5.2** belong to the monoclinic space $P2_1/c$ and $P2_1/n$ space group, respectively. The asymmetric unit of these complexes involve the coordination of a neutral BTA ligand in *mer* fashion to the Zn^{II} central ion. The coordination environment in then completed by the coordination of two chloride anions; as such, the metal ions adopt a five-coordinate arrangement. Compound **5.1** most closely resembles a distorted square pyramidal geometry, as determined by the SHAPE software.[17] Compound **5.2**, however, can be more accurately described as a mixture between square pyramidal and trigonal bipyramidal, which leans in the favor of the former geometry (Table 5.1 and Figure 5.4). This may be due to the presence of MeOH in the lattice which interacts with the complex.

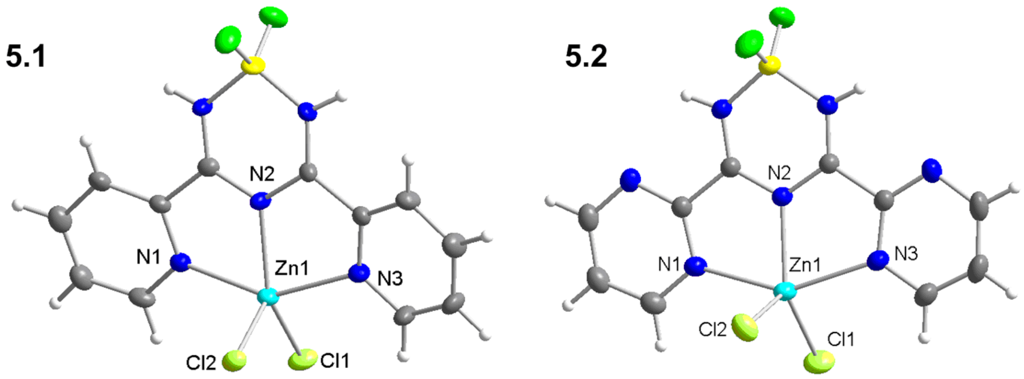

Figure 5.3 – Structural diagram of **5.1** and **5.2** illustrating their asymmetric units with 50% thermal ellipsoids. MeOH in **5.2** is omitted for clarity.

Table 5.1 – Shape analysis of compounds **5.1**-**5.6**. Ideal geometry is a zero value, distortion from this geometry increases the value of the continuous shape measures.

	5.1	**5.2**	**5.3**	**5.4**	**5.5**	**5.6**
PP-5	28.93	31.58		31.96	30.68	
vOC-5	4.35	4.97		5.74	4.69	
TBPY-5	4.27	3.33		5.04	2.73	
SPY-5	2.19	2.63		3.00	2.50	
JTBPY-5	7.60	6.34		8.49	4.86	
HP-6			34.39			28.61
PPY-6			22.03			18.83
OC-6			4.22			8.00
TPR-6			11.84			10.39
JPPY-6			25.37			22.88

HP-6: D_{6h}, Hexagon; PPY-6: C_{5v}, Pentagonal pyramid; OC-6: O_h, Octahedron; TPR-6: D_{3h}, Trigonal prism; JPPY-6: C_{5v}, Johnson pentagonal pyramid J_2, PP-5: D_{5h}, Pentagon; vOC-5: C_{4v}, Vacant octahedron (Johnson square pyramid J1); TBPY-5: D_{3h}, Trigonal bipyramid; SPY-5: C_{4v}, Square pyramid; JTBPY-5: D_{3h}, Johnson trigonal bipyramid (J12).

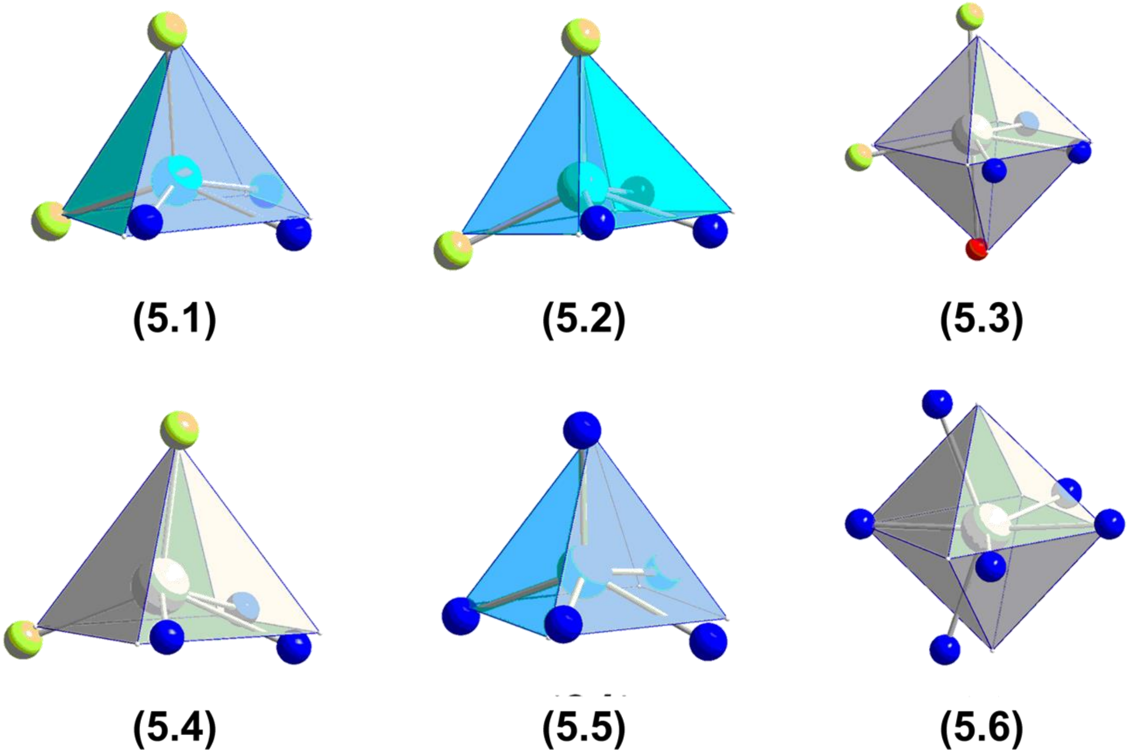
(5.1) (5.2) (5.3)

(5.4) (5.5) (5.6)

Figure 5.4 – Deviation from ideal square pyramidal (**5.1**, **5.2**, **5.4**, and **5.4**) and octahedral (**5.3** and **5.6**) geometrical environments about the metal ion.

By employing the same reaction conditions as above but substituting the metal salt for $CdCl_2$, compounds **5.3** and **5.4** (Figure 5.5) can be isolated from the mother liquor overnight as clear block-shaped crystals. Similar to what is observed with the zinc derivatives, the analogous compounds **5.3** and **5.4** each crystallize in the monoclinic $P2_1/c$ and $P2_1/n$ space group, respectively. Unlike compound **5.1**, the cadmium analogue **5.3** features coordination of a molecule of methanol to the metal centre, forming a distorted octahedral geometry. Compound **5.4** shares a similar coordination environment to **5.2** and features a distorted square pyramidal geometry.

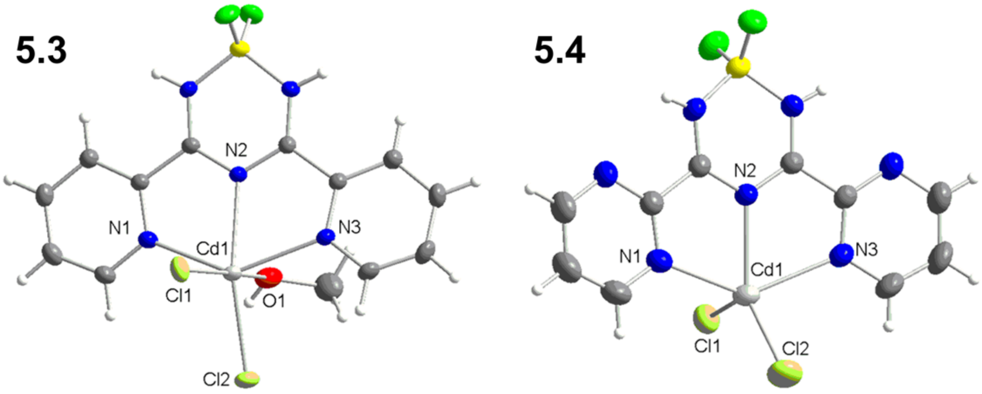

Figure 5.5 – Structural diagram of **5.3** and **5.4** illustrating their asymmetric units with 50% thermal ellipsoids. MeOH is omitted from **5.4** for clarity.

Compound **5.5** (Figure 5.6) can be realized by reacting $ZnCl_2$ and excess KSCN together with Py_2F_2BTA in a 1:1 MeCN:MeOH solution. Similarly, compound **A1** can be realized through the same methodology, with the sole differentiating factor being that Pm_2F_2BTA is employed in the reaction instead of Py_2F_2BTA. Compound **5.6** is accessible through the reaction of $Cd(ClO_4)_2$ and an excess of Py_2F_2BTA in a 1:1 MeCN:MeOH mixture. After stirring the resulting solutions for a few minutes, they were then filtered and placed in a diethyl ether bath. After several days, both compounds **5.5** and **5.6** crystallize as clear plates suitable for SCXRD analysis. Complex **5.5** crystallizes in the monoclinic $P2_1/n$ space group, with a *mer* coordinated molecule of Py_2F_2BTA and two thiocyanate anions bound to the central metal ion through the nitrogen atoms. As with compound **5.2**, the geometry about the central metal ion in complex **5.5** is an intermediate between square pyramidal and trigonal bipyramidal. Conversely, complex **5.6** crystallizes in the triclinic $P\bar{1}$ space group, with two neutral Py_2F_2BTA molecules coordinated in *mer* fashion to the central metal ion. Two molecules of perchlorate are found in the lattice to balance the charge, which are found to possess a 50% positional disorder. Due to the enforced bite angle of the ligands, the geometry of **5.6** can best be described as a heavily distorted octahedron.

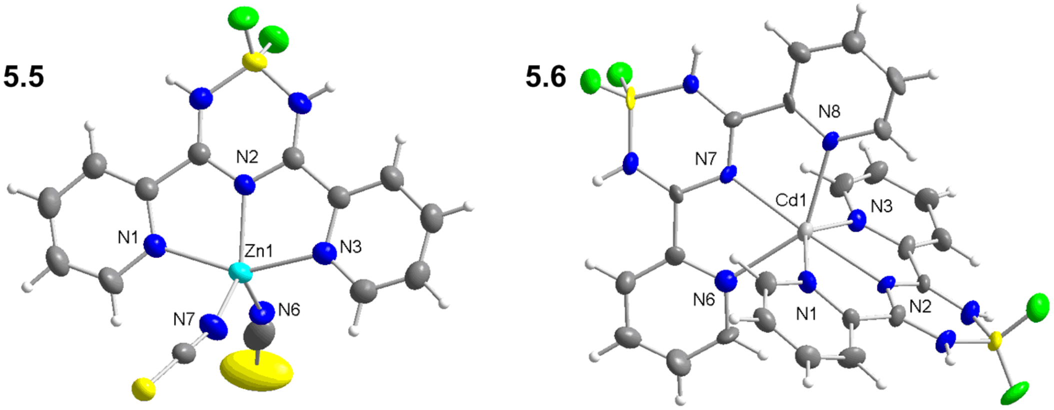

Figure 5.6 – Structural diagram of **5.5** and **5.6** illustrating their asymmetric units with 50% thermal ellipsoids. Uncoordinated molecules in the lattice are omitted for clarity.

In complexes **5.1**-**5.6**, the bond lengths corresponding to the nitrogen atoms of the flanking pyridyl and pyrimidyl groups on Py_2F_2BTA and Pm_2F_2BTA are essentially equivalent, while the metal-nitrogen bonds to the central BTA moieties are shorter; this effect is, however, much less pronounced in compound **5.3**. (Table 5.2). This could be a result of the coordination of a neutral MeOH molecule in an axial position on the complex, causing a pull on the central metal ion away from the plane created by the BTA ligand towards the chloride anion opposite the bound MeOH. Evidence of this can be found in the crystal structure of **5.3**, in which a distance of 0.3600(8) Å can be observed between the Cd^{II} ion and the plane created by N1-N2-N3-Cl2.

Table 5.2 – Select bond lengths (Å) for complexes **5.1-5.6**.

Distance	**5.1**	**5.2**	**5.3**	**5.4**	**5.5**	**5.6**
M1–N1	2.208(4)	2.2388(14)	2.370(2)	2.4320(18)	2.170(3)	2.355(10)
M1–N2	2.077(3)	2.0711(14)	2.338(2)	2.2930(17)	2.052(3)	2.291(8)
M1–N3	2.182(4)	2.2484(15)	2.376(2)	2.4315(19)	2.179(3)	2.337(10)
M1–Cl1	2.2533(16)	2.2233(6)	2.5444(13)	2.4304(7)		
M1–Cl2	2.2857(16)	2.2839(5)	2.5042(12)	2.4174(8)		
M1–O1			2.545(2)			
M1–N6					2.032(3)	2.317(9)
M1–N7					1.969(3)	2.270(8)
M1–N8						2.371(8)

M represents the central metal ion (Zn for **5.1**, **5.3**, **5.5** and **5.6** and Cd for **5.2** and **5.4**)

While complexes **5.1-5.6** all pack in layered arrays in the solid state (Figure 5.7), the nature of the central metal ion, presence of solvent in the lattice, differences in coordination number, and nature of the associated ligands lead to significant differences in their supramolecular arrangements. For example, although the molecular units between layers of complex **5.1** and its pyrimidyl derivative **5.2** are both aligned in a similar face-to-end orientation, the introduction of an uncoordinated molecule of MeOH in the lattice of **5.2** causes additional intermolecular interactions that change the discrete layers causing them to pack two units thick. The intermolecular interactions in compound **5.1** are dominated by short contacts to halide atoms; these involve four N–H···Cl, one C–H···Cl, and one C–H···F hydrogen bond. In compound **5.2**, these interactions are more varied in nature, and include one O–H···Cl, one N–H···Cl, one C–H···F intermolecular interactions, as well as two N–H···N intramolecular short contacts. All hydrogen bonds in this chapter are calculated through the PLATON interface, which uses appropriate D–H···A distances and angles as defined in the literature,[18–20] where D and A are the donor and acceptor atoms, respectively. A list of all short contacts discussed herein are presented at the end of this chapter.

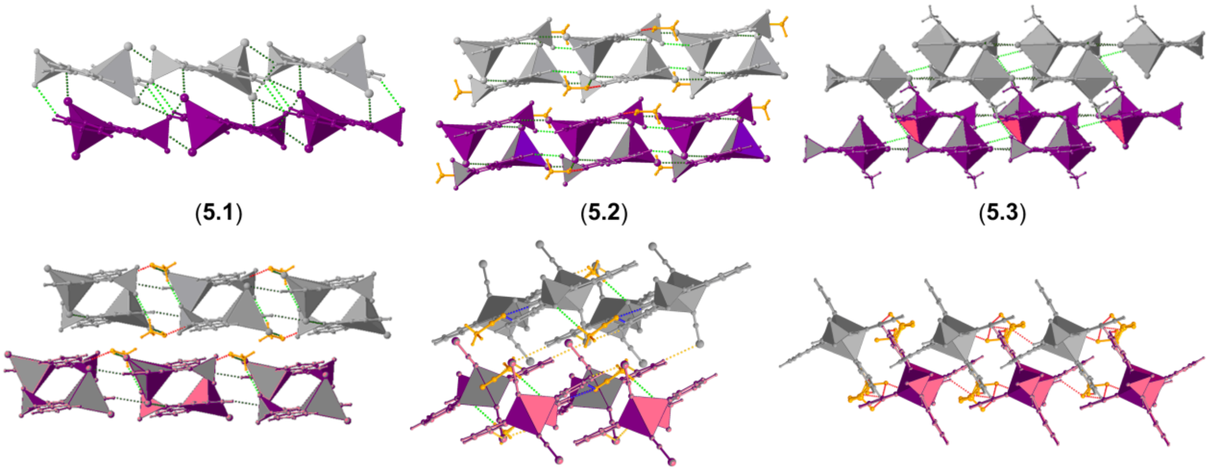

(**5.1**) (**5.2**) (**5.3**)

(**5.4**) (**5.5**) (**5.6**)

Figure 5.7 – Packing diagrams for compounds **5.1-5.6.** Polyhedra are added about the metal centres and boron atoms to depict molecular orientation. Different layers are colored in alternating schemes; molecules in the lattice are colored separately. Possible hydrogen interactions D–H···N (blue), D–H···O (red), D–H···F (light green), D–H···S (yellow), and D–H···Cl (dark green), where D represents the donor atoms, are denoted by dotted lines.

Upon coordination of a molecule of MeOH to the metal ion in compound **5.3**, the space between individual layers is slightly reduced, and the molecular units pack in a similar fashion to that of complex **5.2**. The unique intermolecular interactions in this complex are completely comprised of short contacts to halogen atoms and include one O–H···Cl, two N–H···Cl, two C–H···Cl and two C–H···F hydrogen bonds. Complex **5.4**, which is the cadmium analogue of **5.2**, is found to arrange in a very similar manner in the solid state. Indeed, the intermolecular interactions in complex **5.4** are near identical to that of **5.2**, with the main difference being a lack of C–H···Cl interactions.

By substituting the chloride anions in **5.1** for thiocyanate in complex **5.5**, drastic changes are observed in the supramolecular assembly. The discrete layers are related through a two-fold screw axis (2_1) and connected to one another through intermolecular interactions involving the sulfur atom of the bound NCS ligands. These interactions include one N–H···S and two C–H···S hydrogen bonds, as well as two S···π interactions (both measuring 3.62 Å) that are centered on the central boratriazine rings of the Py_2F_2BTA ligands. Uncoordinated solvent molecules are also present in the lattice, providing additional short contacts through one unique C−H···F interaction; other unique short contacts in this structure involve one N−H···N, and one C−H···N bond.

In compound **5.6**, perchlorate counterions are found in between molecular units of the coordination complex. This leads to a brick-like arrangement in the solid state which is held together mostly through interactions to the counterions. However, the perchlorate molecules have a 50% positional disorder, which increases the amount of unique short contacts. For example, one position features two N−H···O and six C−H···O intermolecular hydrogen bonds, while the other position displays three N−H···O and five C−H···O short contacts. Other unique close contacts belonging to every molecular unit involve two N−H···O, three C−H···O and three C−H···F hydrogen bonds.

5.2.2 Luminescent Properties of Boratriazine-Based Zinc (II) and Cadmium (II) Complexes

There are several examples of terpy-type frameworks which coordinate in *mer* fashion as 2:1 or 1:1 ratios with Zn(II). Quenching of fluorescence in the solution state has, however, been observed and reported for coordination complexes between terpy-like fluorophores and Zn(II) ions.[21–23] This effect has been postulated to be due to internal charge transfer pathways between the excited state of the complex and polar solvents.[7] In our studies of BTA coordination to group 12 metals, we observed near complete quenching of the luminescence in MeOH and tetrahydrofuran (THF) for all compounds studied. Compounds **5.1**-**5.6** are only sparingly soluble in these solvents, and insoluble in solvents of lower polarity, as such these could not be investigated. Despite this, it was possible to investigate the efficiency at which these complexes absorb photon energy through the obtention of their molar extinction coefficients (ε, Table 5.3 and Table 5.4). In THF, the pyridyl-based compounds **5.1**, **5.3**, and **5.5** were found to be less efficient in capturing photon energy than the free ligand, while compound **5.6** was found to be much more efficient. This is likely due to the coordination of two units of the chromophoric ligand per metal centre. Coordination of the pyrimidyl-based BTA ligand to group 12 metals, however, showed a small increase in their extinction coefficients when compared to the free ligand. Although no significant shift is observed upon coordination of Py_2F_2BTA to Zn(II) or Cd(II) cations (Figure 5.8), a small blueshift was observed in the U.V. spectra for complexes of Pm_2F_2BTA (Figure 5.9).

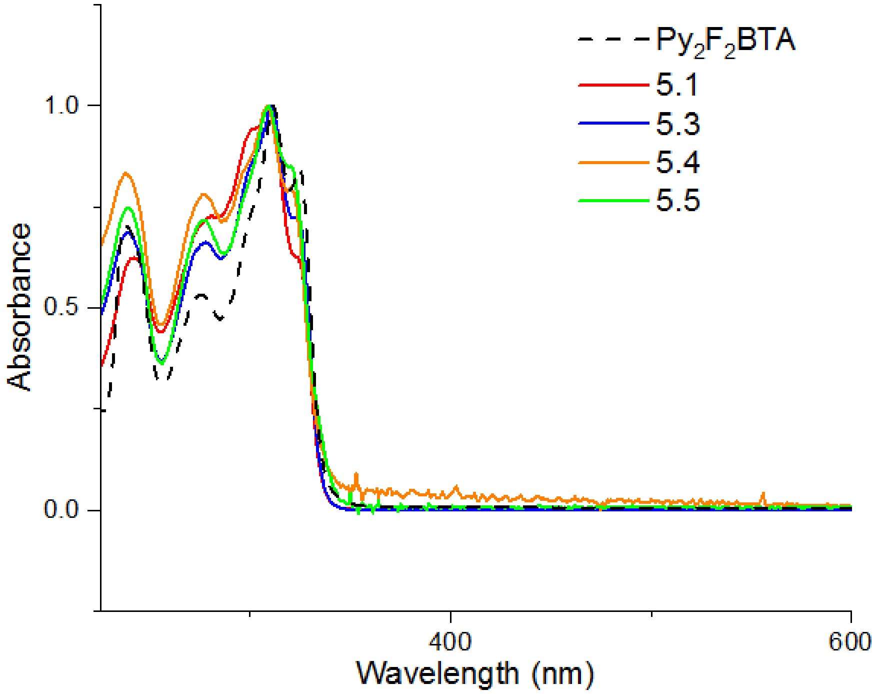

Figure 5.8 – Normalized absorption spectra of Py_2F_2BTA, **5.1, 5.3**, **5.5**, and **5.6** recorded in THF.

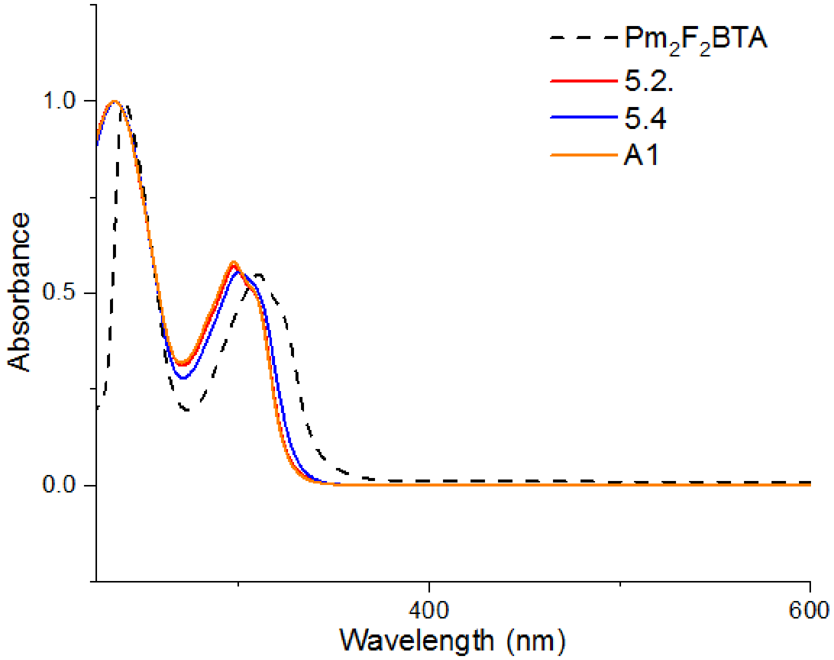

Figure 5.9 – Normalized absorption spectra of Pm_2F_2BTA, **5.2**, **5.4**, and **A1** recorded in THF.

Table 5.3 – Photophysical properties of pyridyl-based BTA compounds in THF.

	λ^{abs} (nm)	**ε ($LM^{-1}cm^{-1}$)**
Py_2F_2BTA	310	22045
5.1	309	14676
5.3	311	19941
5.5	309	18804
5.6	309	33702

Table 5.4 – Photophysical properties of pyrimidyl-based BTA compounds in THF.

	λ^{abs} (nm)	**ε ($LM^{-1}cm^{-1}$)**
Pm_2F_2BTA	239	14549
5.2	235	15423
5.4	235	15037

Due to the observed quenching of the luminescence in solution, we have focused our attention on describing the emissive properties of our group 12 coordination compounds in the solid state. As such, we sought to investigate the solid-state luminescence of our BTA ligands (Figure 5.10) and compare them with that of their complexes (Figure 5.11).

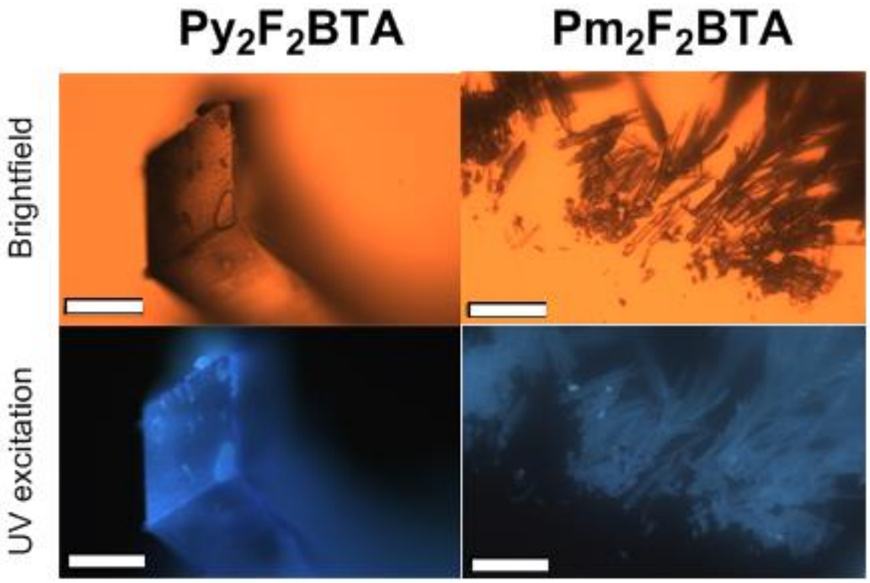

Figure 5.10 – Solid state emission of Py_2F_2BTA and Pm_2F_2BTA. White bars are added for scale, representing 100 μm in length. Crystals were grown as previously described.[24]

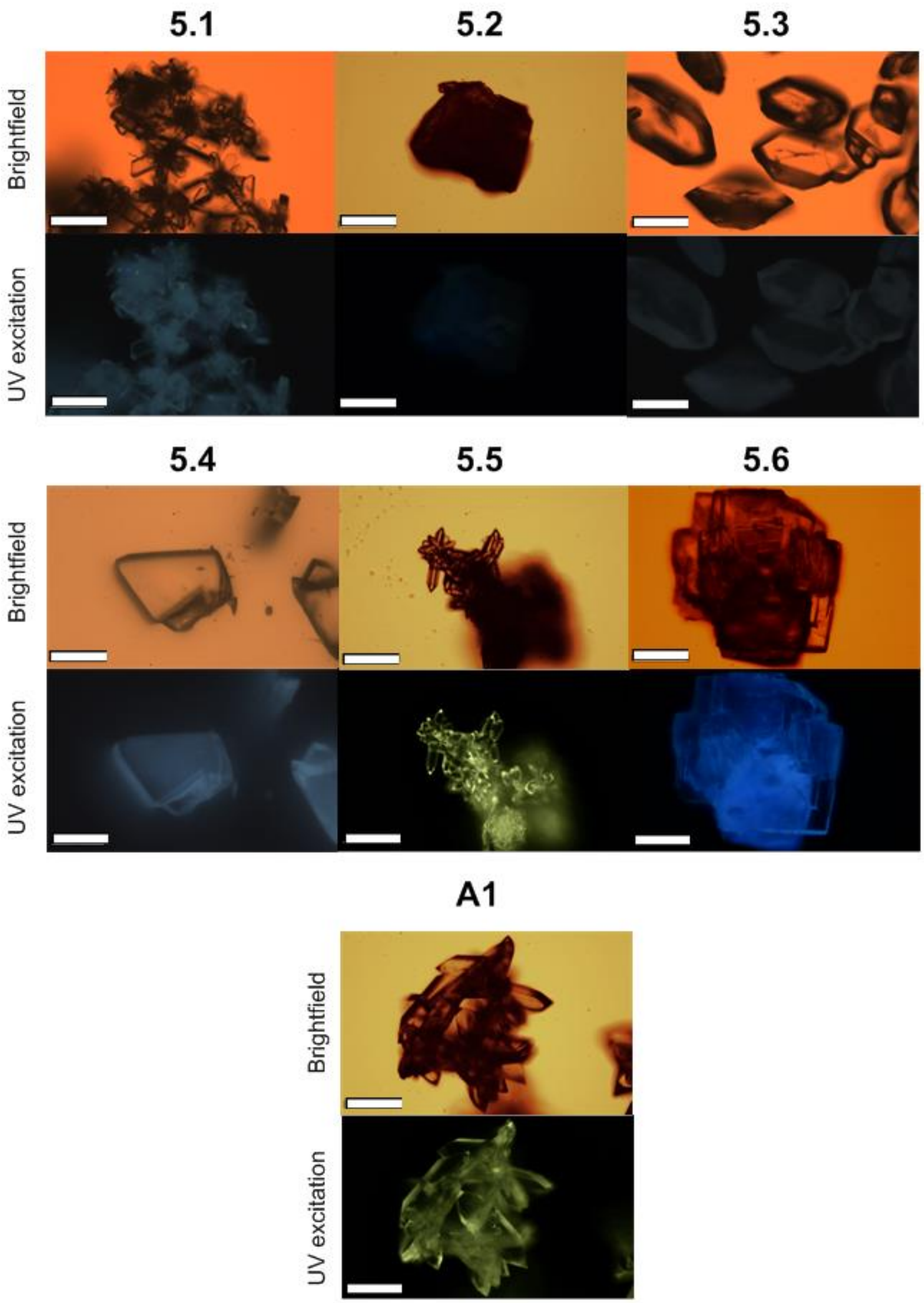

Figure 5.11 – Solid state emission of compounds **5.1-5.6** as well as compound **A1**. White bars are added for scale, representing 100 μm in length.

Heavy atom effects promote intersystem crossing, thus leading to a quenching of the luminescence.[25,26] This phenomena has been used to explain the less emissive nature of chlorinated compounds compared to their non-chlorinated analogues as well as Cd(II) complexes comparatively to their Zn(II) analogues.[21,22,27,28] Indeed, this phenomena is observed for both the pyridyl (**5.1** and **5.3**) and pyrimidyl (**5.2** and **5.4**) derivatives (Figure 5.12). Moreover, halogen ligands have been demonstrated to promote intersystem crossing through the same pathways,[13] which helps explain why complexes **5.1-5.4** are the least emissive. Upon substitution of the chloride ligands for thiocyanate, a large increase in solid state fluorescence is observed for both pyridyl (**5.5**) and pyrimidyl (**A1**) derivatives. Although a crystal structure was not obtained for **A1** comparison of the IR spectra with the analogous complex **5.5** reveals many similarities, most important of which are the characteristic thiocyanate peaks near 2100 cm^{-1}. In the case of compound **5.5**, the emission is comparable to that of the unbound ligand, however, in the case of **A1**, the fluorescence is observed to be larger by a factor of two. The absence of heavy atoms such as chlorine and the chelating mode of the ligand are believed to be responsible for the high luminescence of compounds **5.5** and **A1**. The 2:1 ligand to metal *mer* coordinated complex **5.6** has a stronger emission than the chloride analogue **5.1** by a factor of two, however, the emission of this species is likely experiencing quenching as a result of the hydrogen bonded perchlorate counterions present in the crystal lattice.

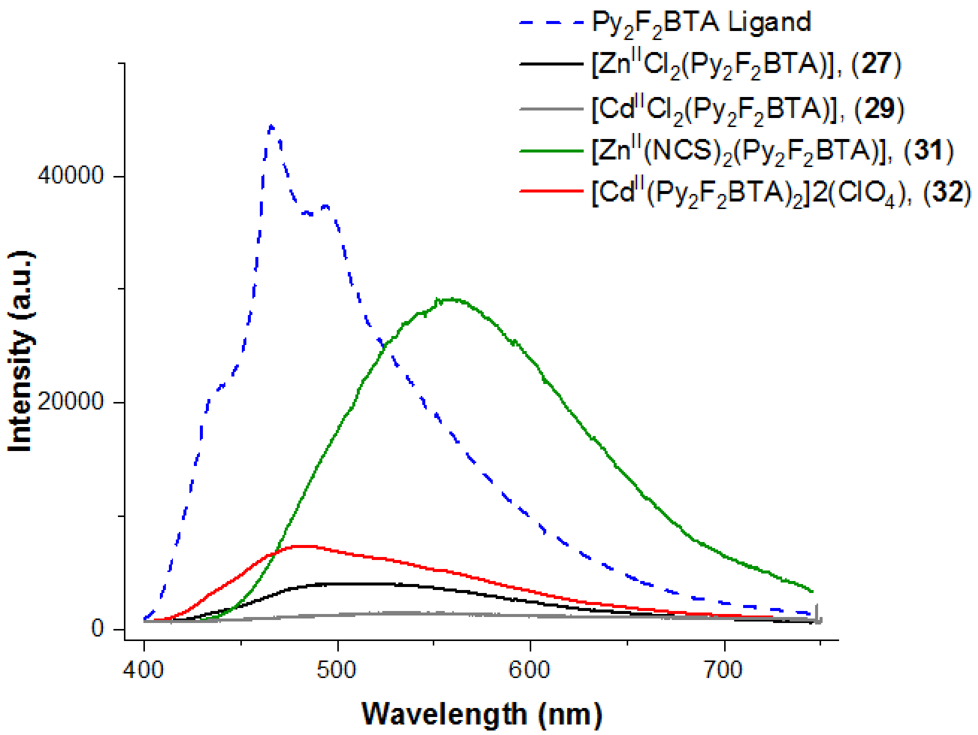

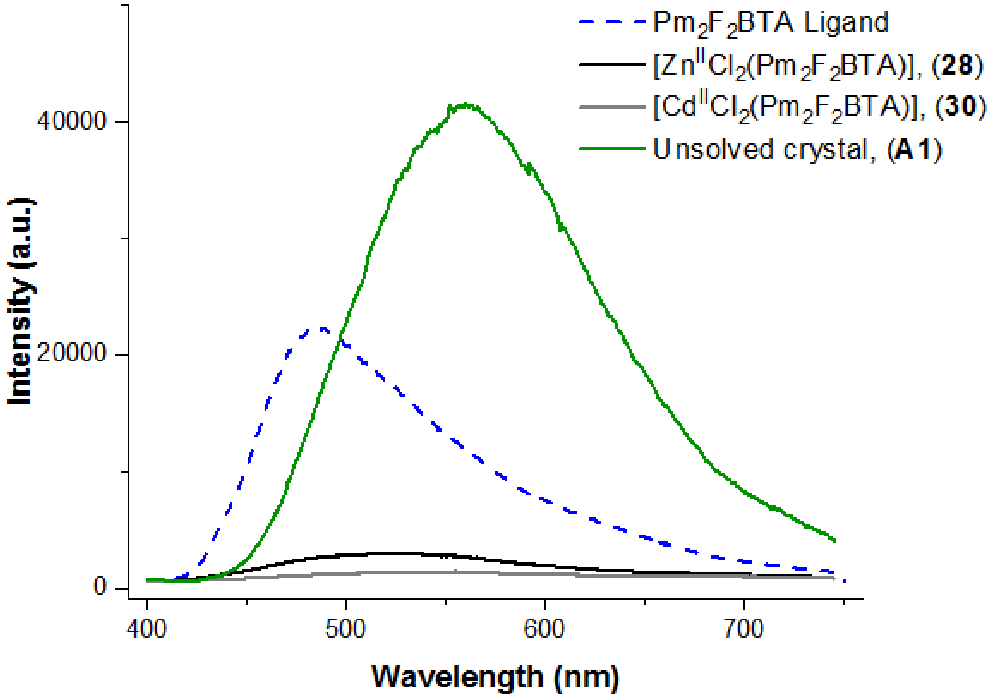

Figure 5.12 – Solid state emission of Py$_2$F$_2$BTA (top) and Pm$_2$F$_2$BTA (bottom) and their complexes. 0.1s UV (broadband excitation) exposure at 50x gain was used to collect the spectra (average of three) over a 2s period.

Through modulation of the coordinated ligands, it has become possible to access luminescent materials which are emit of various colors, as depicted below in a CIE 1931 diagram (Figure 5.13). In general, coordination to Zn(II) and Cd(II) leads to a redshift of the color profile, with blue-green, off-white, and yellow emissions being accessible. Additionally, analogous pyridyl and pyrimidyl complexes are seen to emit similar color profiles.

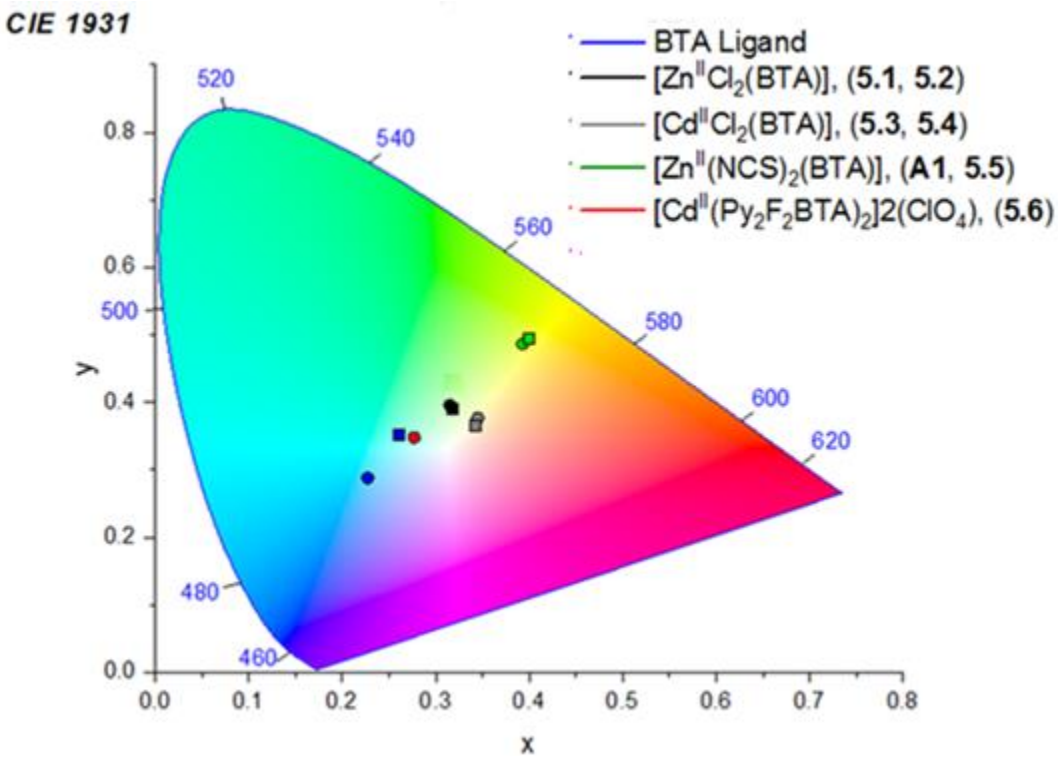

Figure 5.13 – CIE chromaticity diagram showing the color of emission for pyridyl (circles) and pyrimidyl (squares) BTA compounds.

5.3 Summary of Findings

Through our study of Zn(II)/Cd(II) coordination complexes to BTA ligands, we have demonstrated a system with tunability of its emission intensity and color based on the substitution of different ligands. Through the analysis of chloride complexes **5.1-5.4**, we were able to observe an increase in fluorescence intensity upon changing the Cd(II) central metal ion for Zn(II). It was also demonstrated that more efficient emissive complexes can be synthesized upon substitution of the axial chloride ligands. For example, compounds

5.5, and **A1** were shown to be possessive of more intense emission profiles than **5.1** and **5.2** upon the incorporation of thiocyanate anions. Heavy atom effects were speculated to play a key role in this observation, which could help explain the low emissions observed for compound **5.6**. It was also shown that the degree to which complexes **5.1**-**5.6** could absorb photonic energy was comparable to their unbound BTA ligands. Future works within the field of luminescent materials involving the BTA system will be discussed in the following chapter.

5.4 Experimental Procedures

General Procedures

The ligands Py_2F_2BTA and Pm_2F_2BTA were synthesize following previously reported procedures.[24] $ZnCl_2$, $CdCl_2$, and KSCN were obtained from VWR, and $Cd(ClO_4)_2$ was obtained from Sigma-Aldrich. All solvents used were of reagent grade. All reactions were performed at room temperature under regular atmosphere. FT-IR spectra in the range 4000-650 cm^{-1} were recorded on an Agilent Cary 630 FT-IR spectrometer. The visible emissive spectra were obtained on single crystals at room temperature with an inverted optical microscope (Nikon Eclipse Ti-U) using a Nikon Halogen Lamp (IntensiLight 100W) with a broadband camera for color imaging, a set of galvanometer mirrors, a Princeton Instruments SP-2360 monochromator/spectrograph, and a Princeton Instruments ProEM EMCCD camera for detection of the visible emission.

Synthetic Procedure

Preparation of $[Zn^{II}Cl_2(Py_2F_2BTA)]$ (5.1): To a solution of Py_2F_2BTA (30 mg, 0.12 mmol) in MeCN (10 mL) was added a solution of $ZnCl_2$ (20 mg, 0.12 mmol) in MeOH (10 mL). The resulting solution was stirred 5 minutes, then filtered and capped. Clear plate-shaped crystals developed overnight. Yield = 92%. IR (neat, cm^{-1}): 3248(*br*), 3076(*br*), 1646(*m*), 1598(*w*), 1570(*w*), 1507(*s*), 1469(*m*), 1422(*m*), 1330(*m*), 1294(*s*), 1279(*m*), 1168(*w*), 1149(*w*), 1110(*s*), 1094(*s*), 1050(*m*), 1012(*m*), 976(*s*), 816(*m*), 756(*s*), 695(*s*), 683(*m*).

Preparation of $[\mathrm{Zn^{II}Cl_2(Pm_2F_2BTA)}]\cdot\mathrm{MeOH}$ (5.2): To a solution of $\mathrm{Pm_2F_2BTA}$ (30 mg, 0.12 mmol) in MeCN (10 mL) was added a solution of $\mathrm{ZnCl_2}$ (20 mg, 0.12 mmol) in MeOH (10 mL). The resulting solution was stirred 5 minutes, then filtered and capped. Clear plate-shaped crystals developed overnight. Yield = 84%. IR (neat, $\mathrm{cm^{-1}}$): 3449(*br*), 3156(b*r*), 3057(*br*), 1661(*m*), 1623(*w*), 1579(*m*), 1521(*s*), 1442(*w*), 1408(*s*), 1329(*m*), 1285(*m*), 1224(*w*), 1198(*w*), 1171(*w*), 1151(*m*), 1112(*m*), 1095(*w*), 1048(*m*), 1009(*m*), 983(*w*), 961(*s*), 862(*m*), 838(*s*), 811(*w*), 726(*s*), 708(*m*), 666(*m*).

Preparation of $[\mathrm{Cd^{II}Cl_2(Py_2F_2BTA)(MeOH)}]$ (5.3): To a solution of $\mathrm{Py_2F_2BTA}$ (20 mg, 0.08 mmol) in MeCN (10 mL) was added a solution of $\mathrm{CdCl_2}$ (15 mg, 0.08 mmol) in MeOH (10 mL). The resulting solution was stirred 5 minutes, then filtered and capped. Clear block-shaped crystals developed overnight. Yield = 93%. IR (neat, $\mathrm{cm^{-1}}$): 3251(*br*), 3157(*br*), 1630(*m*), 1594(*m*), 1560(*w*), 1467(*s*), 1431(*m*), 1326(*m*), 1288(*s*), 1270(*m*), 1165(*w*), 1129(*w*), 1089(*s*), 1047(*m*), 1009(*s*), 965(*s*), 905(*w*), 820(*m*), 779(*m*), 753(*s*), 712(*m*), 672(*m*), 658(*m*).

Preparation of $[\mathrm{Cd^{II}Cl_2(Pm_2F_2BTA)}]\cdot\mathrm{MeOH}$ (5.4): To a solution of $\mathrm{Pm_2F_2BTA}$ (20 mg, 0.08 mmol) in MeCN (10 mL) was added a solution of $\mathrm{CdCl_2}$ (15 mg, 0.08 mmol) in MeOH (10 mL). The resulting solution was stirred 5 minutes, then filtered and capped. Clear block-shaped crystals developed overnight. Yield = 82%. IR (neat, $\mathrm{cm^{-1}}$): 3434(*br*), 3203(*br*), 2977(*br*), 1651(*m*), 1577(*m*), 1560(*m*), 1516(*s*), 1441(*w*), 1408(*s*), 1326(*w*), 1283(*w*), 1220(*w*), 1197(*w*), 1164(*m*), 1144(*m*), 1095(*m*), 1067(*w*), 1050(*w*), 1025(*m*), 1012(*m*), 982(*m*), 970(*s*), 853(*w*), 834(*m*), 807(*w*), 726(*s*), 710(*m*), 664(*m*).

Preparation of [Zn^{II}(NCS)$_2$(Py$_2$F$_2$BTA)]·MeCN (5.5): A solution of ZnCl$_2$ (20 mg, 0.12 mmol) and KSCN (30 mg, 0.31 mmol) in MeOH (5 mL) was stirred for five minutes, after which a solution of Py$_2$F$_2$BTA (30 mg, 0.12 mmol) in MeCN (5 mL) was added. The resulting solution was stirred 5 minutes, then filtered and placed in a diethyl ether bath. Clear plate-shaped crystals developed after several days. Yield = 72%. IR (neat, cm^{-1}): 3362(*br*), 3215(*br*), 3055(*br*), 2093(*s*), 1645(*s*), 1603(*m*), 1576(*w*), 1497(*s*), 1473(*s*), 1443(*s*), 1425(*m*), 1340(*m*), 1296(*s*), 1280(*m*), 1165(*w*), 1097(*s*), 1067(*s*), 1047(*s*), 1015(*s*), 984(*s*), 971(*s*), 822(*m*), 787(*m*), 761(*s*), 699(*m*), 689(*m*).

Preparation of [Cd^{II}(Py$_2$F$_2$BTA)$_2$]2(ClO$_4$) (5.6): To a solution of Py$_2$F$_2$BTA (30 mg, 0.12 mmol) in MeCN (5 mL) was added a solution of Cd(ClO$_4$)$_2$ (15 mg, 0.05 mmol) in MeOH (5 mL). The resulting solution was stirred 5 minutes, then filtered and placed in a diethyl ether bath. Clear plate-shaped crystals developed after several days. Yield = 89%. IR (neat, cm^{-1}): 3267(*br*), 1637(*m*), 1596(*w*), 1500(*m*), 1467(*m*), 1431(*m*), 1329(*m*), 1294(*m*), 1272(*m*), 1098(*s*), 1074(*s*), 1045(*s*), 1014(*s*), 973(*s*), 816(*m*), 748(*s*), 700(*m*).

Preparation of unsolved crystal (A1): A solution of ZnCl$_2$ (20 mg, 0.12 mmol) and KSCN (30 mg, 0.31 mmol) in MeOH (5 mL) was stirred for five minutes, after which a solution of Pm$_2$F$_2$BTA (30 mg, 0.12 mmol) in MeCN (5 mL) was added. The resulting solution was stirred 5 minutes, then filtered and placed in a diethyl ether bath. Clear plate-shaped crystals developed after several days. IR (neat, cm^{-1}): 3362(*br*), 3220(*br*), 3055(*br*), 2094(*s*), 1644(*s*), 1602(*m*), 1572(*w*), 1523(*s*), 1493(*s*), 1473(*s*), 1443(*s*), 1425(*s*), 1339(*s*), 1296(*s*), 1280(*m*), 1164(*w*), 1096(*s*), 1066(*s*), 1047(*s*), 1015(s), 985(*s*), 971(*s*), 822(*m*), 786(*m*), 761(*s*), 698(*m*), 687(*m*), 669(*m*).

5.5 Crystallographic Information

Single Crystal X-Ray Diffraction Procedures

Prior to data collection, crystals were cooled to 200(2) K. Data was collected on a Bruker APEX II CCD detector with a sealed Mo tube source (wavelength 0.71073 Å). Raw data collection and processing were performed with the APEX II and SAINT software packages from BRUKER AXS.[29] The SHELXT and SHELXL programs were used to solve and refine the structures.[30] All non-hydrogen atoms were refined in anisotropic thermal motion approximation. All non-H atoms were refined anisotropically. The hydrogen atoms of N-H groups were located in a difference Fourier map and refined using bond distance restraints (DFIX in Shelxl), while the remaining hydrogen atoms were placed in idealized positions.

Tables of Crystallographic Data

Table 5.5 – Crystal data and structural refinement for compounds **5.1-5.3**.

Crystal data	**5.1**	**5.2**	**5.3**
FW	409.33	443.36	488.40
Space group	$P2_1/c$	$P2_1/n$	$P2_1/c$
a, (Å)	7.594(3)	6.8333(1)	9.756(4)
b (Å)	12.475(5)	14.2539(3)	12.968(5)
c (Å)	15.658(6)	17.2375(4)	13.984(5)
α, (°)	90	90	90
β, (°)	98.741(8)	98.557(1)	107.241(5)
γ, (°)	90	90	90
V, (Å^3)	1466.0(9)	1660.26(6)	1689.8(10)
Z	4	4	4
D_x, (Mg m^{-3})	1.855	1.774	1.920
μ, (mm^{-1})	2.07	1.84	1.64
Reflections measured	5522	40331	50670
Independent Reflections	5522	5661	4676
Reflections with $I>2\sigma(I)$	3607	4355	3803
R_{int}		0.030	0.063
θ_{max}, θ_{min}, (°)	29.9, 2.1	32.4, 1.9	29.8, 2.2
h	$-10 \rightarrow 10$	$-10 \rightarrow 10$	$-13 \rightarrow 13$
k	$0 \rightarrow 15$	$-21 \rightarrow 21$	$-18 \rightarrow 18$
l	$0 \rightarrow 21$	$-25 \rightarrow 25$	$-19 \rightarrow 19$
$R[F^2 > 2\sigma(F^2)]$	0.047	0.032	0.029
$wR(F^2)$	0.117	0.082	0.068
$\Delta\rho_{max}$, $\Delta\rho_{min}$ (e Å^{-3})	0.65, -0.86	0.67, -0.52	0.61, -0.52

Table 5.6 – Crystal data and structural refinement for compounds **5.4-5.6**.

Crystal data	**5.4**	**5.5**	**5.6**
FW	490.39	495.64	857.43
Space group	$P2_1/n$	$P2_1/n$	$P\bar{1}$
a, (Å)	9.8024(2)	7.9568(6)	8.7255(5)
b (Å)	12.4336(3)	19.2198(14)	9.3296(5)
c (Å)	14.7016(4)	14.3076(11)	19.2715(11)
α, (°)	90	90	85.858(1)
β, (°)	103.9804(6)	104.795(2)	78.401(1)
γ, (°)	90	90	85.249(1)
V, (Å^3)	1738.7(4)	2115.5(3)	1529.0(1)o
Z	4	4	2
D_x, (Mg m^{-3})	1.873	1.556	1.862
μ, (mm^{-1})	1.60	1.40	0.98
Reflections measured	25269	33573	16065
Independent Reflections	3421	5257	8232
Reflections with $I>2\sigma(I)$	2957	3392	4655
R_{int}	0.024	0.058	0.169
θ_{max}, θ_{min}, (°)	26.0, 2.2	28.3, 1.8	30.0, 1.1
h	-12→12	-8→10	-12→12
k	-15→15	-25→25	-13→13
l	-18→18	-19→18	-26→26
$R[F^2 > 2\sigma(F^2)]$	0.020	0.043	0.121
$wR(F^2)$	0.050	0.131	0.290
$\Delta\rho_{max}$, $\Delta\rho_{min}$ (e Å^{-3})	0.44, -0.27	0.74, -0.75	0.462, -0.35

Powder Crystal X-Ray Diffraction Procedures

Bulk purity of the complexes described here was obtained on a Rigaku Ultima IV diffractometer and assessed by comparison of the obtained PXRD patterns with predicted patterns from single crystal data. The experimental PXRD patterns reported herein are found to convincingly match the predicted patterns

Overlay of Experimental PXRD and Predicted (through Mercury) SCXRD Patterns

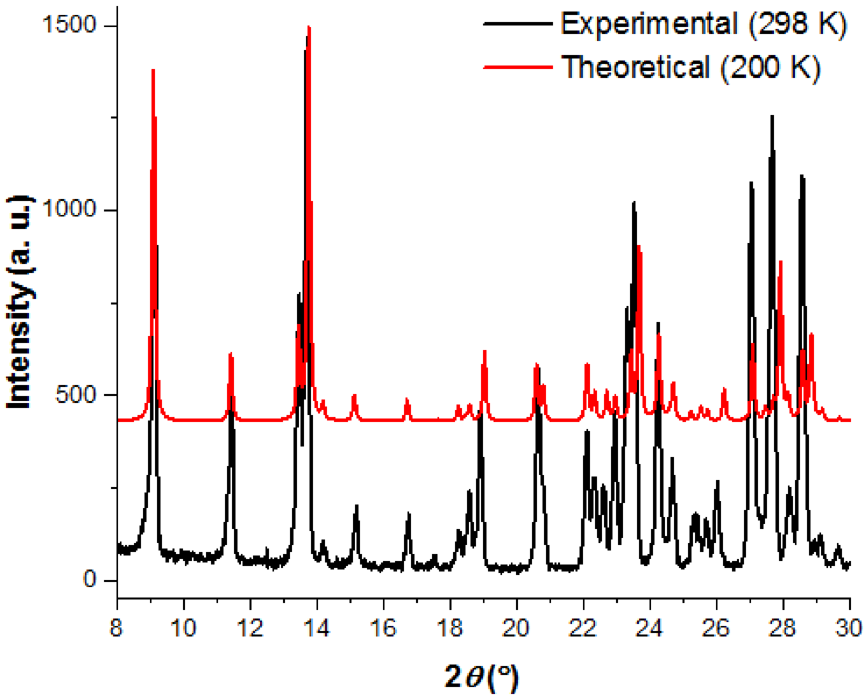

Figure 5.14 – PXRD pattern overlay of experimental microcrystalline sample of **5.1** with the predicted pattern.

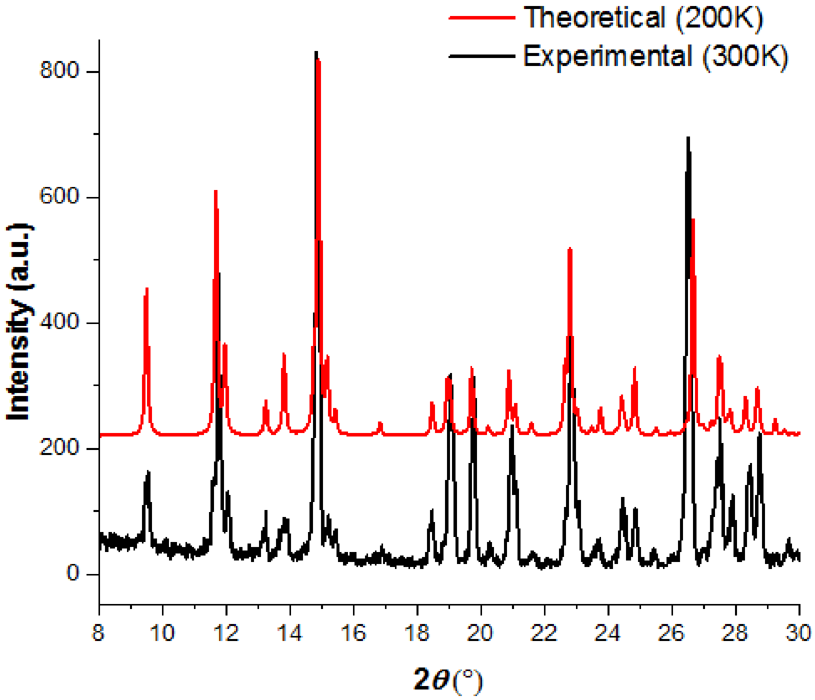

Figure 5.15 – PXRD pattern overlay of experimental microcrystalline sample of **5.3** with the predicted pattern.

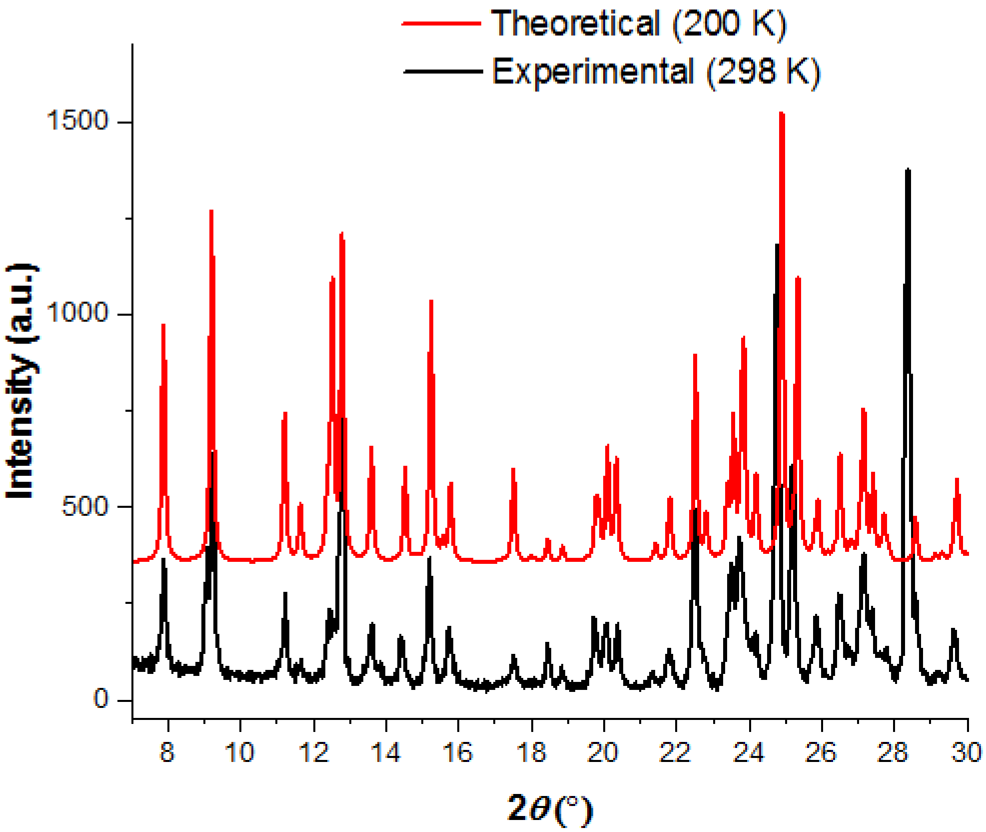

Figure 5.16 – PXRD pattern overlay of experimental microcrystalline sample of **5.5** with the predicted pattern.

5.6 Supramolecular Interactions

Table 5.7 – Hydrogen-bonding in **5.1** (Å, °)

D—H···*A*	*D*—H	H···*A*	*D*···*A*	*D*—H···*A*
N2—H2A···Cl1^{i}	0.85(2)	2.74(4)	3.386(5)	134(4)
N2—H2A···Cl2^{ii}	0.85(2)	2.62(4)	3.227(4)	130(4)
N3—H3A···Cl1^{iii}	0.865(2)	2.82(4)	3.454(4)	132(4)
N3—H3A···Cl2^{iii}	0.86(2)	2.66(4)	3.338(4)	138(4)
C5—H5···Cl1^{iv}	0.95	2.72	3.658(5)	168
C10—H10···F2^{v}	0.95	2.47	3.068(6)	121

Symmetry codes: (i) 1-x,1-y,1-z; (ii) 2-x,1-y,1-z; (iii) x,1/2-y,-1/2+z; (iv) 1-x,1/2+y,3/2-z; (v) 2-x,-1/2+y,1/2-z.

Table 5.8 – Hydrogen-bonding in **5.2** (Å, °).

D—H···*A*	*D*—H	H···*A*	*D*···*A*	*D*—H···*A*
O1S—H1D···Cl2^{i}	0.80(2)	2.41(2)	3.2114(15)	177(2)
N4—H4A···N6	0.853(19)	2.38(2)	2.766(2)	107.7(17)
N4—H4A···Cl1^{ii}	0.853(19)	2.61(2)	3.3317(15)	143.7(18)
N5—H5A···O1S	0.864(16)	1.978(18)	2.804(2)	159.7(19)
N5—H5A···N7	0.864(16)	2.413(19)	2.776(2)	105.9(16)
C1—H1···F1^{ii}	0.95	2.36	3.273(2)	161
C3—H3···Cl2^{iv}	0.95	2.76	3.6793(19)	163

Symmetry codes: (i) 3/2-x,-1/2+y,1/2-z; (ii) -1/2+x,3/2-y,-1/2+z; (iii) 1/2+x,3/2-y,1/2+z; (iv) 3/2-x,-1/2+y,1/2-z.

Table 5.9 – Hydrogen-bonding in **5.3** (Å, °).

D—H···*A*	*D*—H	H···*A*	*D*···*A*	*D*—H···*A*
O1—H1A···Cl2^{i}	0.81(2)	2.46(2)	3.251(2)	166(3)
N2—H2A···Cl2^{ii}	0.84(3)	2.55(3)	3.361(2)	161(2)
N3—H3A···C11^{iii}	0.863(17)	2.45(2)	3.264(2)	158(3)
C3—H3···Cl1^{iii}	0.95	2.79	3.488(3)	131
C4—H4···Cl2^{ii}	0.95	2.79	3.732(3)	174
C12—H12···F2^{iv}	0.95	2.31	3.154(4)	148
C14—H13B···F2^{v}	0.98	2.35	3.266(3)	156

Symmetry codes: (i) 2-x,1-y,1-z; (ii) -1+x,y,z; (iii) 1-x,-1/2+y,1/2-z ; (iv) 1+x,y,z; (v) 1+x,1/2-y,1/2+z.

Table 5.10 – Hydrogen-bonding in **5.4** (Å, °).

D—H···*A*	*D*—H	H···*A*	*D*···*A*	*D*—H···*A*
N2—H2···N7	0.80(2)	2.41(2)	2.748(3)	107.0(18)
N2—H2···Cl1^{i}	0.80(2)	2.61(2)	3.289(2)	144.2(19)
N3—H3···O12	0.77(3)	2.09(2)	2.815(3)	157(3)
N3—H3···N4	0.77(3)	2.35(3)	2.724(3)	111(2)
O12—H12···Cl2^{ii}	0.82	2.40	3.2017(19)	165
C11—H11C···F1^{iii}	0.96	2.43	3.352(3)	161

Symmetry codes: (i) 3/2-x,1/2+y,3/2-z; (ii) 1/2+x,1/2-y,-1/2+z; (iii) 2-x,1-y,1-z.

Table 5.11 – Hydrogen-bonding in **5.5** (Å, °).

D—H···*A*	*D*—H	H···*A*	*D*···*A*	*D*—H···*A*
N2—H2A···N8^{i}	0.88(4)	2.16(4)	3.031(6)	172(4)
N3—H3A···S2^{ii}	0.85(4)	2.59(4)	3.412(3)	163(4)
C3—H3···N8^{i}	0.95	2.49	3.418(5)	164
C9—H9···S2^{ii}	0.95	2.84	3.776(4)	167
C10—H10···S2^{iii}	0.95	2.84	3.672(4)	147
C16—H16B···F2^{iv}	0.98	2.27	3.208(6)	160

Symmetry codes: (i) -1+x,y,z; (ii) 3/2-x,1/2+y,3/2-z; (iii) 1/2+x,1/2-y,-1/2+z; (iv) x,y,z.

Table 5.12 – Hydrogen-bonding in **5.6** (Å, °).

D—H···*A*	*D*—H	H···*A*	*D*···*A*	*D*—H···*A*
N4—H4A···O5B^{i}	0.88	2.08	2.918(19)	158
N4—H4A···O5A^{i}	0.88	2.08	2.95(4)	167
N5—H5A···O6^{ii}	0.88	2.15	3.004(14)	163
N9—H9A···O4^{iii}	0.88	2.22	3.055(14)	159
N10—H10A···O1A^{iv}	0.88	2.37	3.02(2)	131
N10—H10A···O1B^{iv}	0.88	2.00	2.78(2)	147
N10—H10A···O2A^{iv}	0.88	2.59	3.41(3)	156
C1—H1···O2B^{v}	0.95	2.49	3.38(3)	155
C2—H2···O3^{v}	0.95	2.45	3.129(16)	128
C3—H3···O7B^{v}	0.95	2.46	3.38(3)	163
C3—H3···O7A^{v}	0.95	2.28	3.11(4)	146
C4—H4···O5A^{i}	0.95	2.29	3.20(4)	159
C9—H9···O6^{ii}	0.95	2.54	3.422(15)	155
C10—H10···F2^{vi}	0.95	2.53	3.232(14)	131
C12—H12···F3^{iv}	0.95	2.42	3.297(14)	153
C13—H13···O8B^{vii}	0.95	2.51	3.14(2)	123
C13—H13···O7A^{vii}	0.95	2.49	3.37(5)	153
C14—H14···O8B^{vii}	0.95	2.54	3.15(2)	123
C15—H15···F3^{iii}	0.95	2.43	3.334(14)	159
C16—H16···O1A^{iii}	0.95	2.30	3.01(2)	131
C16—H16···O1B^{iii}	0.95	5.51	3.19(3)	128
C16—H16···O4^{iii}	0.95	2.58	3.465(16)	155
C21—H21···O1B^{iv}	0.95	2.55	3.28(3)	133
C24—H24···O8A^{viii}	0.95	2.43	2.98(6)	117

Symmetry codes: (i) 1-x,-y,2-z; (ii) 2-x,-y,2-z; (iii) 2-x,-y,1-z; (iv) 2-x,1-y,1-z; (v) -1+x,y,z; (vi) 2-x,1-y,2-z; (vii) x, y, z; (viii) x,1+y,z.

5.7 References

1 J. R. Lakowicz, *Principles of Fluorescence Spectroscopy*, 2006, Springer, New York, USA
2 B. Valeur and M. N. Berberan-Santos, *Molecular Fluorescence*, 2012, Wiley-VCH, Weinham, Germany
3 S. L. Zheng, X. M. Chen, *Aust. J. Chem.*, 2004, **57**, 703
4 C. Bizzarri, E. Spuling, D. M. Knoll, D. Volz and S. Bräse, *Coord. Chem. Rev.*, 2018, **373**, 49
5 F. Dumur, L. Beouch, M. A. Tehfe, E. Contal, M. Lepeltier, G. Wantz, B. Graff, F. Goubard, C. R. Mayer, J. Lalevée and D. Gigmes, *Thin Solid Films*, 2014, **564**, 351
6 A. Barbieri, G. Accorsi and N. Armaroli, *Chem. Commun.*, 2008, **2008**, 2185
7 L. Zhu, Z. Yuan, J. T. Simmons and K. Sreenath, *RSC Adv.*, 2014, **4**, 20398
8 Y. Hong, J. W. Y. Lam and B. Z. Tang, *Chem. Soc. Rev.*, 2011, **40**, 5361
9 Y. Hong, J. W. Y. Lam and B. Z. Tang, *Chem. Commun.*, 2009, **2009**, 4332
10 A. Erxleben, *Coord. Chem. Rev.*, 2003, **246**, 203
11 J. Du, S. Yu, Z. Huang, L. Chen, Y. Xu, G. Zhang, Q. Chen, X. Yu and L. Pu, *RSC Adv.*, 2016, **6**, 25319
12 B. Zhao, H.-M. Shu, H.-M. Hu, T. Qin and X.-L. Chen, *J. Coord. Chem.*, 2009, **62**, 1025
13 R. Q. Fan, H. Chen, P. Wang, Y. L. Yang, Y. B. Yin and W. Hasi, *J. Coord. Chem.*, 2010, **63**, 1514
14 Q. Wu, J. A. Lavigne, Y. Tao, M. D'Iorio, and S. Wang, *Inorg. Chem.* 2000, **39**, 5248

15 W. Yang, H. Schmider, Q. Wu, Y. S. Zhang, S. Wang, *Inorg. Chem.* 2000, **39**, 2397

16 H. Zhu, M. Ströbele, Z. Yu, Z. Wang, H. J. Meyer and X. You, *Inorg. Chem. Commun.*, 2001, **4**, 577

17 D. Casanova, M. Llunell, P. Alemany, S. Alvarez, *Chem. Eur. J.*, 2005, **11,** 1479

18 G. A. Jeffrey, H. Maluszynska and J. Mitra, *Int. J. Biol. Macromol.*, 1985, **7**, 336

19 G. A. Jeffrey and W. Saenger, *Hydrogen Bonding in Biological Structures*, 1991, Springer Nature, Switzerland

20 T. Steiner, *Crystallogr. Rev.*, 1996, **6**, 1

21 G. Bergamini, L. Boselli, P. Ceroni, P. Manca, G. Sanna and M. Pilo, *Eur. J. Inorg. Chem.*, 2011, **2011**, 4590

22 C. Goze, G. Ulrich, L. Charbonnière, M. Cesario, T. Prangé and R. Ziessel, *Chem. Eur. J.*, 2003, **9**, 3748

23 W. Goodall and J. A G. Williams, *Chem. Commun.*, 2001, **2001**, 2514

24 M. Yousaf, N. J. Yutronkie, R. Castañeda, J. A. Klein and J. Brusso, *New J. Chem.*, 2017, **41**, 12218

25 Y. Shimizu and T. Azumi, *J. Phys. Chem.*, 1982, **86**, 22

26 S. P. McGlynn, J. Daigre and F. J. Smith, *J. Chem. Phys.*, 1963, **39**, 675

27 L. Cuijin, G. Qingbing, Y. Guoqiang, J. Xuhong, and G. Sheng, *Chin. J. Chem.*, 2011, **29**, 1395

28 E. F. Healy, S. Manzer, J. Gorman, A. Jones and N. Cristea, *Chem. Phys. Lett.*, 2010, **485**, 258

29 G. M. Sheldrick, *Acta Crystallogr. Sect. A Found. Crystallogr.*, 2008, **64**, 112

30 G. M. Sheldrick, *Acta Crystallogr. Sect. C Struct. Chem.*, 2015, **71**, 3

CHAPTER 6

6.1 Conclusions

The overarching theme of this thesis has been an exploration into the coordination chemistry of a novel pair of boratriazine-based ligands with first row transition metals. These ligands were engineered through the incorporation of attractive aspects from both the extensively studied chromophore bodipy, as well as the prototypic tridentate chelate terpy. Through this process, photoactive features were effectively introduced into a system capable of versatile coordination, a feature not as easily realized with traditional bodipy based compounds. Through reactions with a variety of metal salts, a plethora of boratriazine-based metal complexes can be achieved. Although the development of luminescent metal complexes are obvious synthetic targets with these ligands, the potential applications of BTA-based metal complexes extends into a diversity of scientific fields due to the unique interplay of metal-ligand interactions that occurs.

Chapter two explored the coordination behaviours of Py_2F_2BTA and Pm_2F_2BTA with iron and cobalt metal sources. This led to the preparation of compounds with different coordination numbers, geometries, ligands, and oxidation states, each of which have a significant impact on the crystal field of the obtained complexes. In particular, through molecular orbital calculations of structurally related complexes, it was possible to quantify the changes in the crystal field energies upon coordination of different ligands in an octahedral environment. In effect, in this chapter structural, synthetic and coordination trends have been identified which may aid in the targeted preparation of future complexes.

Chapter three makes use of the concepts explored in the previous chapter in order to prepare dinuclear Fe^{II} and Co^{II} constructs bridged through azide ligands. Since azido bridges are known to promote magnetic exchange between metal centres, the magnetic analysis of these compounds was investigated and discussed, revealing ferromagnetic interactions in both cases. Chapter four continued our investigation into magnetic materials through the synthesis and structural characterization of pentacoordinate Fe^{II} and Co^{II} metal centres with thiocyanate ligands. Due to time constraints, the magnetic data of these compounds was not obtained, nonetheless a discussion on compounds featuring similar coordination environments is included.

Chapter five demonstrated the use of group 12 metals Zn^{II} and Cd^{II} for the preparation of luminescent materials. The tunability of the emission intensity and color of these systems was investigated based on the substitution of different ligands/counterions about these metal centres. It was shown that, by carefully avoiding processes leading to the non-luminous decay of the molecules excited state, it was possible to create compounds of comparable or greater luminescence than that of the unbound ligand in the solid state.

6.2 Future Works

The work presented in this thesis represents the first investigations into the coordination chemistry of BTA-based ligands, however, there remains numerous unexplored avenues left opened to analysis. Within this section potential future projects will be highlighted.

It has been demonstrated in the literature that, through substitution of the fluorine ions of bodipy type compounds for alkyl or alkoxy groups, further modulation of the photophysical properties can be achieved without compromising the emission intensity.[1,2] We have discussed the preparation of $Py_2(MeO)_2BTA$ in chapter two, proving the feasibility for this avenue of research. It would thus be of interest to investigate the changes in the photophysical properties of our BTA system upon the synthesis of various $N{-}BX_2{-}N$ analogues.

In chapter two, the coordination of multiple BTA ligands to Co^{II} and Fe^{II} through their tridentate coordination pockets were targeted for their potentially interesting magnetic properties. Indeed, octahedral complexes with these metals featuring two terpy-like ligands bounds through their tridentate binding sites often lead to the observation of SMM behaviour. It was found that microcrystalline material can be obtained from reactions involving excess Py_2F_2BTA or Pm_2F_2BTA with $M^{II}(BF_4)_2$ or $M^{II}(ClO_4)_2$, where M is either cobalt or iron. Through the use of large counterions, such as tetrafluoroborate or perchlorate, it is expected that a single metallic species be observed in the crystal lattice. In fact, this technique was shown effective in chapter five for the development of compound **5.6**.

With respect to compounds **4.1** and **4.2** described in chapter four the magnetic measurements are, to date, pending analysis. Coordination complexes featuring similar coordination environments have been discussed; these analogous compounds have been shown to be SMMs. As such, depending on the results of the measurements for **4.1** and **4.2**, other complexes with similar coordination environment, counterions, etc. may be explored.

BTA consists of a triazine ring with a boron atom incorporated. Exploring other triazine ring systems in which the heteroatom is replaced enables one to study the heteroatom effect. To that end, heavier atoms such as sulfur and selenium, in place of the BF_2 moiety in Py_2F_2BTA and Pm_2F_2BTA should allow for better opportunities for enhanced magnetic and electronic interactions in associated complexes by virtue of larger orbital overlaps.[3] Thus, it would be interesting to explore and contrast these systems as molecular analogues to compounds **3.1**, **3.2**, **4.1**, and **4.2**.

Luminescence metal complexes with heavy metal ions have been widely studied for sensing applications, particularly complexes based on ruthenium (II), platinum (II), iridium (III), osmium (II), gold (I), and rhenium (I). The unique photophysical properties observed with these metal centres are a result of a complicated set of relaxation pathways made available to the molecular excited state. These include metal to ligand, ligand to ligand, intraligand, ligand to metal, and metal to metal charge transfers.[4] The use of *f-f* emissions from lanthanide ions are also of special interest due to their sharp line-like spectra and long lifetimes. These line-like emissions are due to the shielded 4*f* transitions by 5*s* and 5*p* orbitals, while the lifetime is due to the partially forbidden *f-f* transitions.[5] The exploration of luminous materials involving our BTA system and these metal ions are therefore expected to provide exciting new compounds in future investigations.

6.3 References

1 J. Bañuelos, *Chem. Rec.*, 2016, **16**, 335

2 B. Bertrand, K. Passador, C. Goze, F. Denat, E. Bodio and M. Salmain, *Coord. Chem. Rev.*, 2018, **358**, 108

3 N. J. Yutronkie, A. A. Leitch, I. Korobkov and J. L. Brusso, *Cryst. Growth Des.*, 2015, **15**, 2524

4 D. L. Ma, V. P. Y. Ma, D. S. H. Chan, K. H. Leung, H. Z. He and C. H. Leung, *Coord. Chem. Rev.*, 2012, **256**, 3087

5 J. C. G. Bünzli, S. Comby, A. S. Chauvin and C. D. B. Vandevyver, *J. Rare Earths*, 2007, **25**, 257